DOCTOR OF PHILOSOPHY

Watermass Transformations near the Tip of the Antarctic Peninsula

Mead Silvester, Jess

Award date:
2017

Awarding institution:
Bangor University

PRIFYSGOL
BANGOR
UNIVERSITY

School of Ocean Sciences, Bangor University
National Oceanography Centre Liverpool

Watermass Transformations near the Tip of the Antarctic Peninsula

Jess Mead Silvester

Main supervisor:
Yueng Djern-Lenn

Co-supervisors:
Jeff A. Polton
Miguel Angel Morales Maqueda
Tom P. Rippeth
Helen E. Phillips

Submitted in partial fulfilment of the requirements for the degree of
Doctor of Philosophy in Physical Oceanography
Bangor University October 2017

Abstract

The global overturning circulation is a density-driven circulation that controls Earth's climate through its latitudinal transport of heat, freshwater and carbon. In the Southern Ocean, which links all the major oceans of the world, watermasses that are critical to the Meridional Overturning Circulation (MOC) outcrop and transform as they exchange properties that affect their density (e.g heat, salt), acting to close the mass budget of the MOC. Two cells make up the Southern Ocean component of the MOC: a lower cell in which the major portion of global dense waters are formed and the upper cell in which waters subducted elsewhere are returned to the surface via upwelling.

The watermasses that transform to drive Southern Ocean overturning have been warming and freshening over recent decades, which has implications for overturning and upwelling strength as well as the drawdown of carbon during dense water formation. The turbulent mixing processes that drive these watermass transformations and the origins of seasonally conditioned dense waters that form the densest watermass are poorly quantified and spatially characterised. This limits our ability to forecast climate change in this region, its global transmission and the performance of climate models. The aim of this thesis is to investigate processes that influence watermass transformations that are critical to the Southern Ocean MOC.

Over the continental slope at Elephant Island, we observe the first direct evidence of elevated yet intermittent diapycnal mixing at mid-depths and propose that observed mixing is forced by the locally-generated internal tide. These events occur between overturning cells and are associated with shear instability and turbulent mixing, driving watermass transformation at depth instead of at the surface following upwelling. This has implications for Southern Ocean overturning and upwelling strength. At the same location but two years later, we capture direct heat exchange between a lens (likely an eddy) of Upper Circumpolar Deep Waters (UCDW) and Lower Circumpolar Deep Waters (LCDW). Heat, mass and buoyancy are lost from UCDW to the cooler LCDW beneath as they transform at mid-depth, with instabilities across their shared boundary consistent with symmetric forcing in phase with the baroclinic tide. We propose a mechanism whereby eddy-tide interaction might drive mid-depth heat dispersion from warm UCDW-core eddies, which are the main form of heat transport onto the shelf along the Western Antarctic Peninsula where the recent acceleration of ice-shelf melt is linked to ocean warming. Finally, we link the magnitude of seasonal dense-water pulses at this same location

with that of previous-season sea-ice concentration over a wider area dominated by Powell Basin in the west Weddell Sea (the prime site of seasonally-conditioned dense water production), which is separated from waters at Elephant Island by the South Scotia Ridge. We find that the time-lag and the location of three further observations of dense water crossing the South Scotia Ridge via western Hesperides Trough and on the continental slope east of Elephant Island are consistent with tidally-induced currents along connecting isobaths. This pathway is more direct than previously proposed, allowing exported waters to maintain more cohesive dense, cold properties upon arrival at the continental slope where they may interact with warm, saline CDW and convect downslope to replenish and ventilate Antarctic Bottom Waters.

This work highlights the contribution of tides to processes that influence the Southern Ocean MOC. The findings of the thesis implicate the tide in forcing mid-water diapycnal mixing as the baroclinic tide interacts with topography and in driving overturns as the baroclinic tide modifies a submesoscale feature. These processes drive watermass transformations at depth where they can influence upwelling rates and facilitate mid-depth ocean warming where glacier melt is sensitive to heat content along the Western Antarctic Peninsula. Additionally, it is proposed that the tidally-induced flow around bathymetry might play a role in exporting Weddell Sea waters onto the slope at Elephant Island. This work demonstrates that temporally-intermittent and submesoscale features and flows (i.e sub-grid processes) contribute to watermass transformations in the Southern Ocean; depending on location, these can have a significant influence on regional climate. This work makes a contribution towards understanding the spatial and temporal variability of these sub-grid processes and highlights regions where these processes may be studied further.

Acknowledgements

I am grateful to the National Oceanography Centre in Liverpool for offering and funding this PhD studentship through the National Environmental Research Council's grant (NE/K500938/1).

I have been lucky to have had brilliant, approachable supervisors who have made undertaking this PhD an absolute pleasure. I am grateful for the excellent teaching and mentoring of Yueng-Djern Lenn, my main supervisor, as well as for the opportunities thrown my way. I would like to thank Miguel Angel Morales Maqueda for the data, for taking me on a research cruise along the Antarctic Peninsula and for the good company while there - and Jeff Pugh and many others on this cruise too; Jeff Polton for teaching, patience and an inspiring level of clarity; Tom Rippeth for showing me the importance of a good story; Helen Phillips for the warm welcome at UTAS and for arranging lessons in planning an EM-APEX float mission.

I am indebted to Yvonne Firing, Geoff Hargreaves and Steve Mack for deploying EM-APEX float 4980b and John Dunlap for relaying its instructions at my frequent requests; to others whose comments improved this work and to my fellow-PhDs for conversation and tea breaks.

Thank you Liz and Ted, who made life exciting, for demonstrating that anything is attainable in the right spirit. My partner would call it obstinacy. I am grateful for the support and encouragement of my grandparents. I thank Idris, who never consented but came to accept my absences to finish this thesis. And whose loveliness distilled this work into what was practicable, pinning down many tangental explorations into a hopefully coherent piece of work. Thanks to Ted, Caz, Alan, Loz and Charlotte, who picked up various responsibilities so that this could be finished without (too much) domestic or professional disgrace. An enormous thank you to Sally and Jasper, without whose wonderful friendship (and Dylan Evans by association) I would not have been able to pursue oceanography. Most of all, Tom, my partner in life and a magician of sorts. The first years of my PhD were a great laugh and we accomplished much in life beyond our PhDs; this last one has been a boring and unfulfilling year for you, keeping everything going until I can return to a shared life. Thank you for your tolerance and for ensuring that I have (just) enough sleep and am well fed. You have been (mostly) supportive and especially good at moderating my expectations of myself. Last but not least, thank you to Carreg, Cidyll and Pandim, for walking me when I needed it. They are waiting by the door now.

Author Contributions

I undertook all research and the writing of Chapter 3. Chronologically, this was my first piece of work. I was supervised by Yueng-Djern Lenn, Miguel Angel Morales Maqueda, Jeff A. Polton and Tom P. Rippeth whose tutorial contributions were mainly in the form of guiding the exploration of the data and driving mechanisms of observed phenomena. I was given the data by Miguel Angel Morales Maqueda and Yueng-Djern Lenn. This is published in *Geophysical Research Letters*.

I undertook all research work and the writing of Chapter 4, with feedback from Yueng-Djern Lenn, Jeff A. Polton, Helen E. Phillips and Miguel Angel Morales Maqueda. I explored the data, we agreed on initial direction and heat flux computations (with Yueng-Djern Lenn); it was my idea to explore instabilities from the potential vorticity. I was given the EM-APEX float data from a previous mission by Miguel Angel Morales Maqueda. This has been submitted to the *Journal of Physical Oceanography*.

I undertook the research and writing of Chapter 5. The idea for comparing seasonal magnitudes in sea-ice concentration and BPR lander temperature was mine, scripts for extracting the tidally-induced current from TMD were adapted from Jeff Polton's at his suggestion and I was primarily advised by Jeff Polton and Yueng-Djern Lenn, with feedback on the written piece from Tom P. Rippeth and Helen E.Phillips. EM-APEX float data was organised and funded by Miguel Angel Morales Maqueda, but I was responsible for planning and guiding the 2015 float's mission (but not its deployment, see Section 2.4), with some earlier training from Helen E. Phillips. This chapter is currently in preparation for *Geophysical Research Letters*.

For the spirit of the journey:

‘ They sailed away in a Sieve, they did,
In a Sieve they sailed so fast,
With only a beautiful pea-green veil
Tied with a riband by way of a sail,
To a small tobacco-pipe mast;
And every one said, who saw them go,
‘O won’t they be soon upset, you know!
For the sky is dark, and the voyage is long,
And happen what may, it’s extremely wrong
In a Sieve to sail so fast!’
Far and few, far and few,
Are the lands where the Jumblies live;
Their heads are green, and their hands are blue,
And they went to sea in a Sieve.

The water it soon came in, it did,
The water it soon came in;
So to keep them dry, they wrapped their feet
In a pinky paper all folded neat,
And they fastened it down with a pin.
And they passed the night in a crockery-jar,
And each of them said, ‘How wise we are!
Though the sky be dark, and the voyage be long,
Yet we never can think we were rash or wrong,
While round in our Sieve we spin!’
Far and few, far and few,
Are the lands where the Jumblies live;
Their heads are green, and their hands are blue,
And they went to sea in a Sieve.’ *(15-42)*

Edward Lear, ‘The Jumblies’

Contents

List of Figures

List of Tables

List of Acronyms

AABW	Antarctic Bottom Water
AAIW	Antarctic Intermediate Water
ACC	Antarctic Circumpolar Current
ADCP	Accoustic Doppler Current Profiler
ASF	Antarctic Slope Front
BPR	Bottom Pressure Recorder
CC	Coastal Current
CDW	Circumpolar Deep Water
CTD	Conductivity Temperature Depth
DSW	Dense Shelf Water
EPV	Ertel Potential Vorticity
LCDW	Lower Circumpolar Deep Water
MOC	Meridional Overturning Circulation
PF	Polar Front
RRS	*Royal Research Ship*
SAF	SubAntarctic Front
SAM	Southern Annular Mode
SSR	South Scotia Ridge
TKE	Total Kinetic Energy
UCDW	Upper Circumpolar Deep Water
VMP	Turbulent Microstructure Profiler
WSDW	Weddell Sea Deep Water
WSF	Weddell Sea Front

Chapter 1

Introduction

1.1 Motivation

In the Southern Ocean, water masses which are critical components of the global overturning circulation outcrop into the ocean's surface layer. These watermasses are transformed as they exchange properties, acting to complete the global overturning circulation, which controls Earth's climate through redistributing heat latitudinally. The properties of watermasses critical to the Southern Ocean overturning cells have been changing (warming and freshening) over the past few decades, some of which is attributed to anthropogenically-forced regional warming. Our poor understanding of where Southern Ocean watermass transformations occur, their drivers (e.g turbulent mixing, upwelling) and the origins of seasonally conditioned waters contributing to these watermasses pose a significant limitation on our ability to forecast climate change in this region and its global transmission.

1.2 Background

While a concise background and literature review is given at the beginning of each of the three data chapters, a broader overview of the Southern Ocean, its unique processes and role

in the Meridional Overturning Circulation (MOC) is given here. This section constitutes an introduction to all the processes relevant to the main chapters of this thesis and is intended not to duplicate, but to provide a coherent context to the reader for all three chapters.

1.2.1 The Southern Ocean and Drake Passage

The MOC is a primarily density-driven circulation that is responsible for the meridional transport of the Earth's incoming solar radiation (heat). High-latitude processes dominate dense water formation globally: in the Southern hemisphere, Antarctic Bottom Water (AABW) formation is primarily controlled by sea-ice production (Ohshima *et al.* , 2016) as the majority of brine is rejected into surface-cooled waters as sea-ice forms each season. This watermass accounts for the greatest portion of ocean mass (30-40%, (Johnson, 2008)). Dense water formation is balanced by diffusion across the thermocline into surface waters at low latitudes and upwelling in the Southern Ocean, closing the mass budget of the global overturning circulation and explaining observed ocean stratification. The Southern Ocean MOC is increasingly viewed as central to driving the MOC (Marshall & Speer, 2012) (Fig.1.1).

The Southern Ocean overturning circulation comprises two cells: a lower in which waters transform while subject to air-sea fluxes near the cold continent, lose buoyancy and sink to form AABW; and an upper cell in which surface waters are deflected northwards by Ekman transports to form Antarctic Intermediate Water (AAIW). Diverging surface waters are replenished by warm Circumpolar Deep Water (CDW) as it upwells along tilted and thinning isopycnals. Rising waters are much warmer than surrounding waters and so control the northern limit of the cryosphere, and demarcate the circumpolar boundary between the two cells (approximately of isopycnal 27.6 kg m^{-3}, which outcrops at the sea-ice edge (Marshall & Speer, 2012). Fronts in the Southern Ocean are associated with sharp lateral gradients in hydrographic properties, with the Polar Front demarcating the northern limit of a minimum temperature of 2^oC at 100 - 200 m depth, roughly coinciding with the limit of sea-ice influence, and the Subantarctic Front defining the northernmost extent of circumpolar currents (Fig.1.2a).

The vigorous, eastward-flowing Antarctic Circumpolar Current (ACC) dominates the Southern

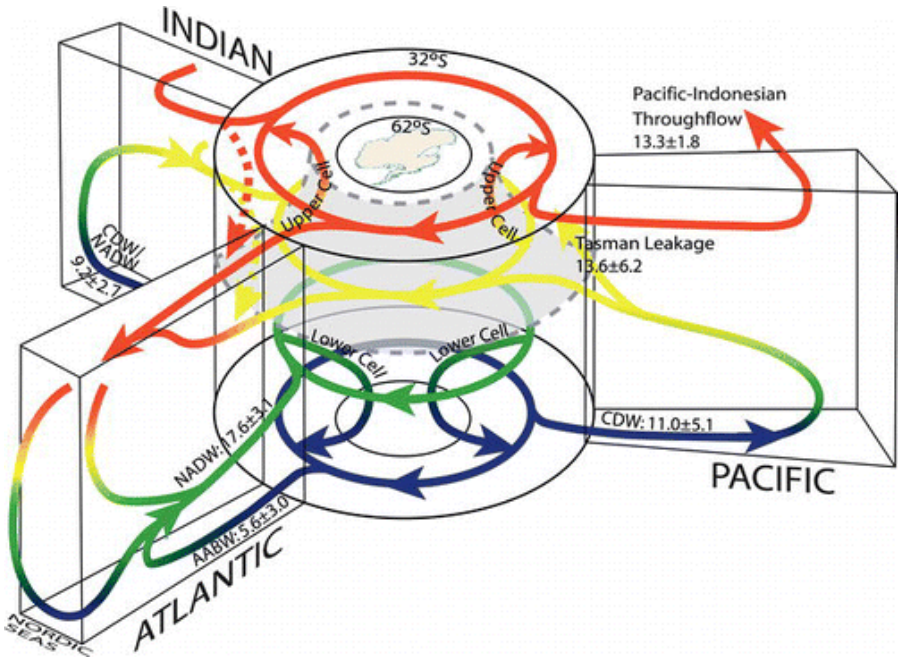

Figure 1.1: A schematic perspective on the Meridional Overturning Circulation with the Southern Ocean overturning cells at its centre reproduced with permission from Rick Lumpkin (Lumpkin & Speer, 2007). The colour gives approximate density ranges in depth-space so that the red is $\gamma n \leq 27.0$, yellow is $\gamma \simeq 27.0$ - 27.6, green is $\gamma n \simeq 27.6$ - 28.15 and blue is $\gamma n \geq 28.15$, where γn is a neutral density surface. The grey-dashed surface is $\gamma n = 27.6$ at 32°S which separates the upper and lower cell transformation in the Southern Ocean.

Ocean: able to circumnavigate the globe unimpeded by landmasses and connecting all the Earth's major oceans, it is vital for exchanging physical (heat, salt, carbon) and biogeochemical properties between ocean basins. This current is characterised by energetic eddies and jets, is driven by strong westerly winds and is guided by bottom topography as it flows through gaps between ridges, plateaus and shelves at depth, but is uninterrupted in its zonal flow above 1800 m (Hallberg & Gnanadesikan, 2006). Drake Passage presents the narrowest intercontinental opening through which the ACC flows, with ridges around the South Scotia Sea additionally obstructing deeper waters. Since there are no zonal pressure gradients (created by meridional boundaries) in the Southern Ocean, the wind-driven northward Ekman transport of surface waters is balanced by a poleward geostrophic flow at depth only, where topographical barriers exist (Meredith *et al.* , 2011).

As westerly winds induce Ekman surface transport northwards and a return geostrophic flow at depth where bathymetry allows, there is an associated upwelling (downwelling) to the south (north) over the ACC axis, known as a Deacon cell. This acts to overturn density interfaces, inclining isopycnals upwards towards Antarctica and generating a store of potential energy (Hallberg & Gnanadesikan, 2006). Eddies restore equilibrium to the baroclinically unstable isopycnals by extracting the available potential energy as eddy kinetic energy (Marshall & Radko, 2003), flattening isopycnals and transporting mass polewards. The wind-driven Deacon cell and the eddy restoration force are equal yet opposite in overturning sense and the strength of upwelling is approximately the sum of these two circulations (Marshall & Radko, 2003) (Fig.1.2b). Drake Passage has been identified as an upwelling hotspot in circumpolar terms (Tamsitt *et al.* , 2017). This upwelling is adiabatic and requires no vertical mixing, so that waters are transformed in the ocean's surface layer where they are subject to air-sea fluxes, after upwelling.

However, this paradigm has been challenged by the hypothesis that watermasses can transform at depth, prior to outcropping into the surface mixed-layer, effectively 'short-circuiting' the adiabatic pathway as mixing across and movement along isopycnals both contribute to upwelling (Naveira Garabato *et al.* , 2007; Watson *et al.* , 2013). These transformations are driven by diapycnal (cross-isopycnal) mixing as water masses exchange properties and Watson *et al.* (2013) suggest that it may account for 20-30% of Southern Ocean upward volume transports. Diapycnal mixing can occur when instabilities arise from the internal wave field. Internal waves oscillate on density interfaces in the stratified ocean interior and can be generated by barotropic (internal) tides interacting with topography (at near-tidal frequencies) or by changes in wind stress (at near-inertial frequencies). Where instabilities arise, internal waves can break, initiating a cascade of energy to turbulence length-scales. Since internal waves lie along the interface between density strata, turbulence increases the surface area of contact between the layers, enhancing the exchange of properties where gradients are greatest. The diapycnal turbulent diffusivity of mass, k_p is described in Munk (1966)'s advection-diffusion equation, which expresses a balance between the upward advection of water and the downward diffusion of a property (e.g heat):

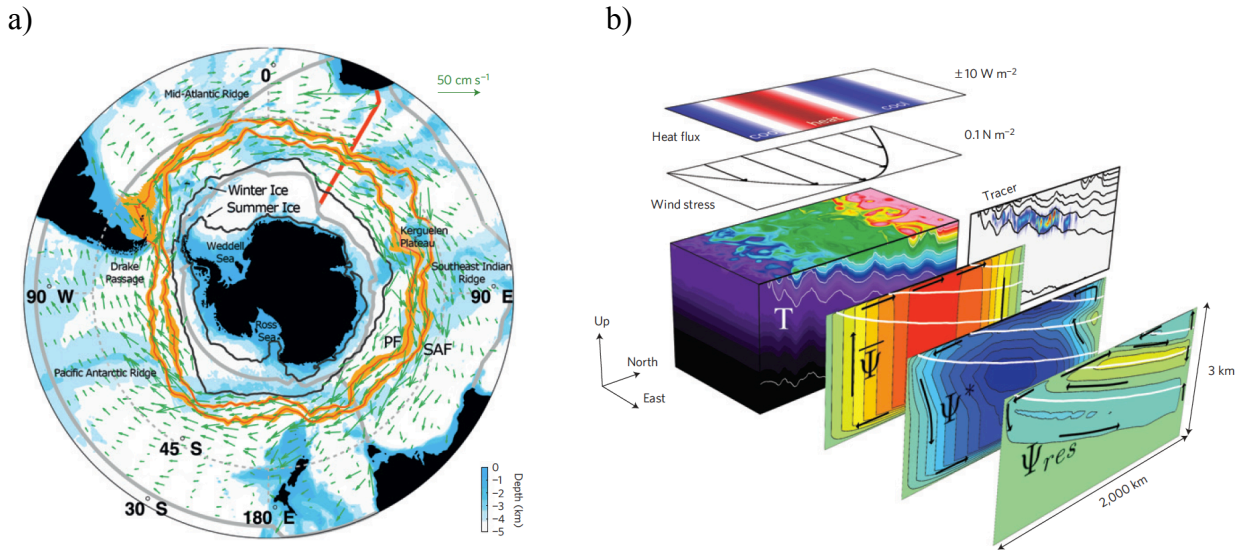

Figure 1.2: These schematics are reproduced with permission from John Marshall from (Marshall & Speer, 2012). a) Shows the average locations of the Subantarctic Front (SAF) (orange outer ring), the Polar Front (PF) (orange inner ring) and their respective variances in thicker orange; speed and direction of 15-m drifter currents (green arrows); seasonal sea-ice margins (black, labelled) and the average extent of sea-ice (grey). Depth is shaded in blue. b) is a snapshot from idealised ACC simulations, in which we are interested in the wind stress; the temperature field which undulates with the mesoscale eddy field and the time-mean overturning cells that make up the Deacon cell. Here, $\overline{\psi}$ is the mean wind-driven overturning which sets up vertical isopycnals; $\psi*$ is the eddy overturning circulation which acts to flatten vertical isopycnals and ψ_{res} is the residual overturning. White lines indicate density surfaces.

$$W\frac{d\theta}{dz} = (\frac{d}{dz})(k_p\frac{d\theta}{dz}) \tag{1.1}$$

where W is the vertical velocity, θ is the potential temperature, ρ is the potential density and z is the depth coordinate. Highly non-linear internal waves can break locally in diapycnal mixing events while others may be radiated away from their generation site through the ocean's interior to contribute to background mixing. Munk (1966) estimates the magnitude of diapycnal mixing required to maintain stratification against 25 - 30 Sv of deep water formation to be of order 10^{-4} m^2 s^{-1}, ten times higher than that observed (Watson *et al.* , 2013). This 'missing mixing paradox' implies that mixing must be spatially and temporally concentrated (Munk & Wunsch, 1998; Naveira Garabato *et al.* , 2004).

The mechanical energy input required to drive sufficient turbulent mixing to maintain existing stratification is $\sim$ 2 TW, partitioned roughly equally between wind and tidal energy (Munk, 1966). The Southern Ocean is windy, with its zonal storm belt accounting for 80% of the world's wind energy (Zhai *et al.* , 2012), is tidally energetic (Heywood *et al.* , 2007), sufficiently topographically complex to break internal waves (Nikurashin *et al.* , 2013) and the prerequisite stratification and internal wave field are both present (Marshall & Speer, 2012). As such, the Southern Ocean represents a global mixing hotspot, but is in itself spatially variable (Whalen *et al.* , 2012). The question of whether there is sufficient concentrated diapyncal mixing that observations are not resolving either temporally or spatially to meet the required global average of 10^{-4} m^2 s^{-1} remains, but it is perhaps now more relevant to ask: what are the relative contributions of diapycnal mixing, adiabatic upwelling and subsurface watermass transformation to MOC closure?

Our understanding of these Southern Ocean processes greatly limits the predictive capabilities of climate models since sub-grid processes such as diapycnal mixing and meso- to submesoscale eddy fluxes must be parameterised (Alford, 2003; Marshall & Speer, 2012). While global circulation models are limited by grid-size (increasing sensitivity to the accuracy of parameterisation) and representing the uniquely complex 3-dimensional dynamics of the Southern Ocean, observations are limited by harsh environmental conditions, it is sensible to focus efforts on improving parameterisation. Critical steps include: (1) quantifying temporally-intermittent and spatially-variable diapycnal mixing, (2) identifying the depth of peak diapycnal mixing, (3) constraining the range of effective diffusivities, (4) accurately relating observed mixing to energy sources and (5) quantifying meridional eddy transport.

1.2.2 Climate and Climate Variability

The MOC mediates Earth's climate by controlling meridional transports of heat, carbon and other climatic variables, and is strongly linked to variability in past and present climate change (Peixoto & Oort, 1992). The upwelling branch of the two-cell overturning circulation in the Southern Ocean is increasingly considered fundamental to climate control (Farneti *et al.* , 2015;

Huybers & Wunsch, n.d.), with Marshall & Speer (2012) claiming that the Southern Ocean plays at least an equally important role as north Atlantic overturning in controlling climate variability. The Southern Ocean is a globally important carbon sink, accounting for ∼40% of all ocean carbon uptake (Sabine *et al.* , 2004), a consequence of the high primary productivity in the surface mixed-layer as upwelling waters deliver the productivity-limiting micronutrient iron (Cullen & Boyd, 2008). Carbon dioxide drawn into surface waters sinks via the biological pump mechanism (see Ducklow *et al.* (2001)) and is sequestered in the deep ocean (AABW) via subducting AAIW and South Antarctic Mode Water (SAMW) (Meredith *et al.* , 2011). On glacial-interglacial timescales, the upwelling of carbon-rich Southern Ocean waters is associated with deglacial increases in atmospheric CO_2 concentration (Sigman & Boyle, 2000). Thus, variability in the strength of upwelling controls the net flux of CO_2, heat and nutrients between the atmosphere, surface mixed-layer and the ocean interior.

Since the ACC permits a global circulation through inter-basin exchange, anomalies in one ocean basin may be transmitted around the globe, influencing climate in remote locations (White & Peterson, 1996). Over the past few decades, sustained observations across Drake Passage have captured a number of changes in the atmosphere, cryosphere and ocean that are thought to be linked to anthropogenic climate change (see e.g (Meredith *et al.* , 2011; Marshall & Speer, 2012) for summary) and influence the CO_2 flux into the Southern Ocean. These include the rapid melting of marine glaciers along the West Antarctic Peninsula (WAP) (Cook *et al.* , 2016) linked to mid-depth ocean heat content over the continental slope (Martinson & McKee, 2012) and warming throughout the Southern Ocean (Gille, 2008) including AABW, which, through its significant volume also impacts on global sea-level (Purkey & Johnson, 2010). Atmospheric warming is thought likely to influence stratification and strengthen the Southern Ocean westerly wind belt and drive it polewards (Fyfe *et al.* , 2007; Le Quéré *et al.* , 2000; Meehl & Zhao, 2007). The strength of the global MOC is thought to be sensitive to changes in the westerly wind-belt (Abernathey *et al.* , 2011). The wind belt is observed to shift southward during positive Southern Annular Mode (SAM) years (the dominant mode of interannual variability in the southern hemisphere), which are increasingly often positive (Meredith *et al.* , 2011). The consensus under this scenario is that northward Ekman transports are increased

(and the ACC eddy field responds proportionately) leading to enhanced upwelling: this brings more warm water into contact with ice shelves and sea-ice (Meehl & Zhao, 2007; Anderson *et al.* , 2009; Ito *et al.* , 2010; Saenko *et al.* , 2005) as well enhancing CO_2 outgassing; the latter has been observed over the past 20 years (Le Quéré *et al.* , 2008). This process, along with increased ice melt along the WAP, is linked to observed AAIW freshening (see also (Meredith & King, 2005)). Both AAIW and AABW have freshened and warmed over the last few decades (Schmidtko *et al.* , 2014; Purkey & Johnson, 2010; van Wijk & Rintoul, 2014; Jacobs & Giulivi, 2010), and a key concern is whether changes in their buoyancy will affect subduction rates and hence the strength of the Southern ocean overturning cell (Meredith *et al.* , 2011); the total volume of AABW has reduced over the same time period (Johnson, 2008), with Purkey & Johnson (2012) inferring a slowdown in AABW production. Exported Weddell Sea Deep Water (WSDW), the main source of dense shelf waters from which AABW is formed, is also freshening (Jullion *et al.* , 2013), but knowledge of export pathways and the role of shelf-sourced AABW and their formation sites limits our ability to monitor variability in AABW formation (Snow *et al.* , 2016).

The delicate balance of air-sea-ice interactions and feedbacks highlights the Southern Ocean and in particular the region around the Weddell Sea and the WAP as being of local and global significance for climate change. While we lack a coherent understanding of how anthropogenic warming might force parameters and feedbacks here, it is clear that understanding watermass transformations critical to the upper and lower overturning cells of the Southern Ocean MOC would vastly improve the forecasting capabilities of climate models. Major weaknesses presently include the accurate parameterisation of diapycnal mixing and upwelling (and sensitivity to those parameters), the contribution of watermass transformations at depth to upwelling, and our understanding of the export pathways and variability of dense waters leading to AABW formation.

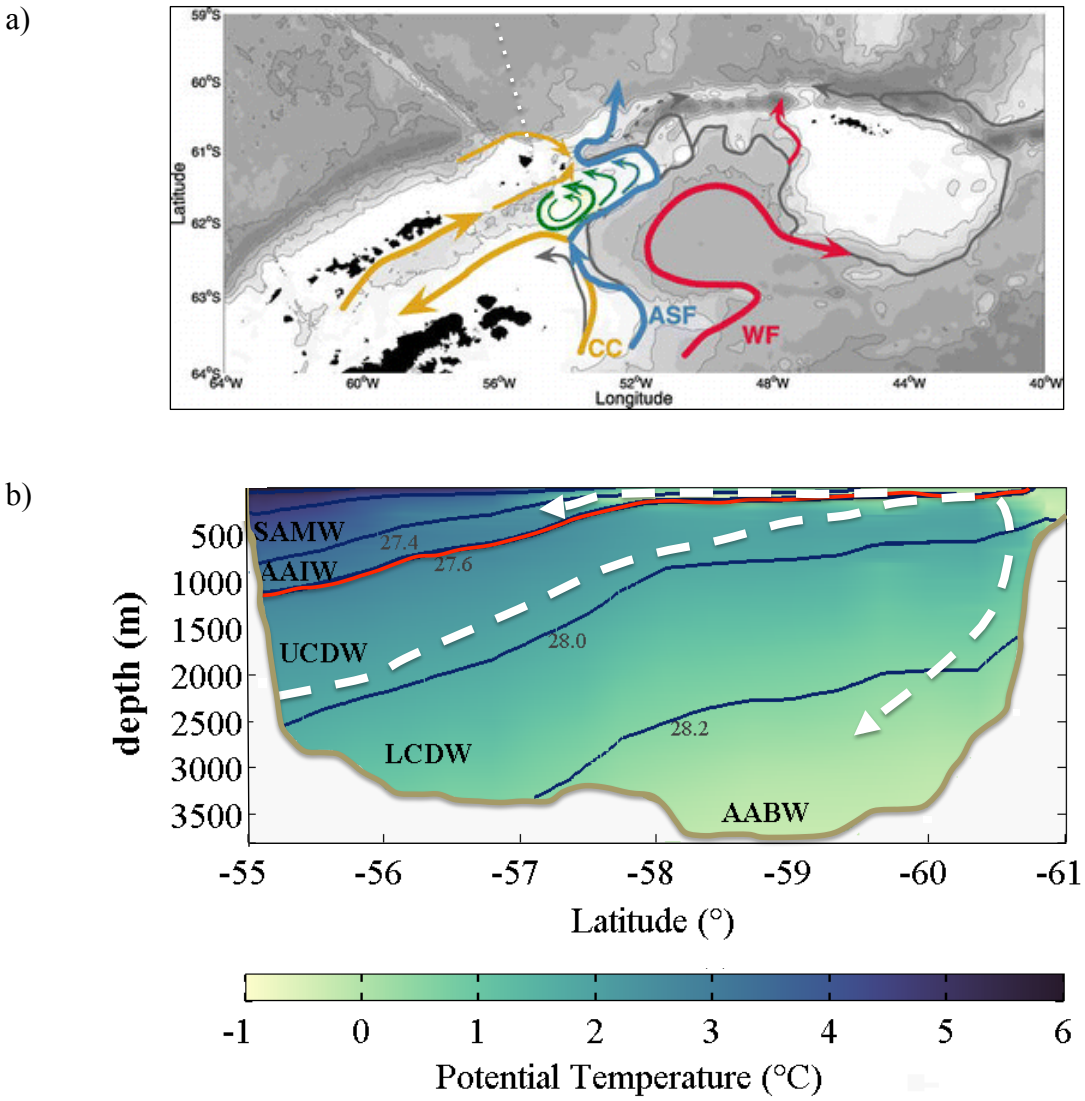

Figure 1.3: Two schematics to illustrate currents and circulation near the tip of the Antarctic Peninsula. a) is reproduced with permission from Andrew Thompson from Thompson *et al.* (2009) and shows surface currents from drifters labelled as the Coastal Current (CC), the Weddell Front (WF) and, in grey, Antarctic Slope Front currents from Heywood *et al.* (2004). Bathymetry shades change every 500 m and contours between 1000 m and 4000 m are drawn at 1000-m intervals. The southernmost component of SR1B transect track has been added to this figure in dashed-white to clarify b) in which the potential temperature over the decade to 2009 along the SR1B transect ending at Elephant Island is shown in colour-filled contours with potential density contours (kgm^{-3}) that commonly define the boundaries between watermasses overlain in smooth black lines and that which circumpolarly divides upper and lower overturning cells in red. Here, SAMW is Subantarctic Mode Water, AAIW is Antarctic Intermediate Water, UCDW is Upper Circumpolar Deep Water, LCDW is Lower Circumpolar Deep Water and AABW is Antarctic Bottom Water. The white dashed arrows roughly depict the lower and upper cells of the Southern Ocean as waters cool near the continent and sink to form AABW and are deflected northward by Ekman transports. Diverging surface waters are replenished by upwelling CDW.

1.2.3 Elephant Island Hydrography

Elephant Island forms the northernmost tip of the Antarctic Peninsula. The wider area is known as the Weddell Scotia Confluence and is characterised by the continental slope which extends eastwards from Elephant Island and the SSR which divides the Weddell Sea from the open ocean at South Drake Passage (for map, see Fig.2.1). Over the steep continental slope immediately north of Elephant Island, CDW and the isopycnal (27.6 kg m^{-3}) that circumpolarly divides the upper and lower Southern Ocean overturning cells outcrop into the surface mixed-layer (Figs.1.2b and 1.3b). South Drake Passage is one of the few regions where upwelling waters are thought to outcrop close to the continental slope (Tamsitt *et al.* , 2017). Here, Meredith *et al.* (2003) hypothesise that downslope convection feeds AABW and, to the east, WSDW is exported onto the continental slope via Phillip Passage and Orkney Passage (Heywood *et al.* , 2004), perhaps further west towards Elephant Island (Thompson *et al.* , 2009) (Fig.1.3a). The region is known for strong slope currents and is favourable for tidally-induced diapycnal mixing; much of the steep continental shelf-break is sufficiently sloped (Heywood *et al.* , 2007; Padman *et al.* , 2006). Thus, the ocean that surrounda the tip of the Antarctic Peninsula is remarkable in its representation of processes that dominate Southern Ocean physics as well as being accessible. As such, the Elephant Island region benefits from a number of long-standing observational campaigns, including an annually-repeated hydrographic transect across Drake Passage to Elephant Island (SR1B) and pressure gauges on the continental slope.

1.3 Aims and Objectives

The overarching aim of this thesis is to investigate processes influencing the watermass transformations that are critical to the MOC in the Southern Ocean. The study site is Elephant Island, where the watermass structure that makes up the Southern Ocean MOC is exemplified in meridional cross-section onto the continental slope. The objectives are to investigate:

1. intermittent diapycnal mixing at depth;

2. watermass transformations at depth;

3. sources of observed seasonal pulses of dense water at Elephant Island and

4. Weddell Sea water export pathways onto the continental slope.

1.4 Thesis Structure

The structure of this thesis follows a 'thesis by publication' format, in which Chapters 3-5 are presented as manuscripts *in lieu* of a results section, reproduced as-is, but with all references consolidated into a single bibliography with the framing thesis and supporting information included at the back of each relevant chapter. Chapter 2 provides an overview of data and methods; Chapter 3 investigates enhanced intermittent mixing across isopycnals that divide the Southern ocean overturning cells; Chapter 4 analyses the transformation of two watermasses as they exchange heat over the continental slope and Chapter 5 investigates the origin of seasonal dense water pulses on the slope at Elephant Island. Chapters 3-5 include their own introductions, methods, results, discussions and conclusions and are prefaced by a short paragraph tying them into the thesis as a whole and all references are all enclosed in the thesis' Bibliography section. Supporting information is included at the back of each chapter. Chapter 6 provides a summary and synthesis of the complete work and its contribution to current understanding of the topic.

1.5 Publications

Mead Silvester, J., Y.-D. Lenn, J. A. Polton, T. P. Rippeth and M. A. Morales Maqueda (2014), Observations of a diapycnal shortcut to adiabatic upwelling of Antarctic Circumpolar Deep Water, *Geophysical Research Letters*, 41, 79507956, doi:10.1002/2014GL061538.

Mead Silvester, J., Y.-D. Lenn, J. A. Polton, H. E. Phillips and M. A. Morales Maqueda (2017), Watermass Transformation at Mid-Depths over the Antarctic Continental Slope, manuscript submitted to the *Journal of Physical Oceanography* for publication.

Chapter 2

Instrumentation and methods

2.1 Overview of Cruises and Instruments

The following paragraphs provide an overview of the datasets used in Chapters 3-5. This does not duplicate the methods sections given in each of the paper chapters, but gives a coherent summary of the instrumentation and datasets used to produce this work as a whole and expands on some of the instrumentation. All primary data collection was carried out on three separate cruises aboard the *RRS* James Clark Ross in different years (2009, 2011 and 2015). Since there is overlap in the data used for Chapters 3-5, the data are summarised according to cruise, greater detail of EM-APEX float handling and some supplementary information that is not given in the abbreviated methods sections of data chapters is provided. All computational methodologies, including calibration, are confined to the paper chapters' respective methods sections. Table 2.1 summarises the instrumentation used and Fig.2.1 illustrates the locations of all instrumental deployments.

2.2 Research Cruise JR198 (2009)

The data used from this cruise comprise concurrent conductivity-depth-temperature (CTD) and VMP microstructure turbulence profiler casts as well as shipboard ADCP data over the

Instrumentation				
instrument	deployment	manufactured model	measured variables	units
CTD	tethered	Seabird Electronics	conductivity temperature pressure	S m^{-1} ^{o}C decibar
VMP-1000	free-falling	Rockland Scientific Instrument	dissipation	W kg^{-1}
ADCP	shipboard	75 kHz RDI Ocean Surveyor	horizontal velocities	cm s^{-1}
EM-APEX floats 4908a,b	autonomous remotely controlled	SeaBird Electronics pumped CTD	conductivity temperature pressure, horizontal velocities	S m^{-1} ^{o}C decibar cm s^{-1}
		electromagnetic subsystem		

Table 2.1: Summary of instruments used and their respective specifications and measured variables.

continental slope at Elephant Island. This was part of Cruise JR198, which ran along the annually-repeated SR1B track from Burdwood Bank, south of the Falkland Islands, and Elephant Island from 18-29 November 2009. These data were collected by principal investigators Miguel Angel Morales Maqueda and Yueng-Djern Lenn, and are used principally in Chapter 3.

2.3 Research Cruise R265 (2011)

As part of this cruise, an EM-APEX float (no. 4980a) was deployed by principal investigator Miguel Angel Morales Maqueda on 5 December 2011, again over the continental slope at Elephant Island. The EM-APEX float is a pseudo-Lagrangian, autonomously profiling instrument which can be set to profile according to a particular dive pattern between fixed depths and surface as requested to transmit data and receive new instructions via Iridium link. The float profiled continuously between 400 m and 900 m, surfacing every few days until near recovery (as batteries depleted) 12 days later on 17 December 2011. The float contains an inflatable bladder which is used to change the buoyancy of the float to match specified depths. During this time, the float profiled along the continental slope before entering Hesperides Trough and continuing eastward along its northern flank. Data were post-processed onshore by John Dunlap at Webb Research Corporations (USA). These data are used in Chapters 4 and 5.

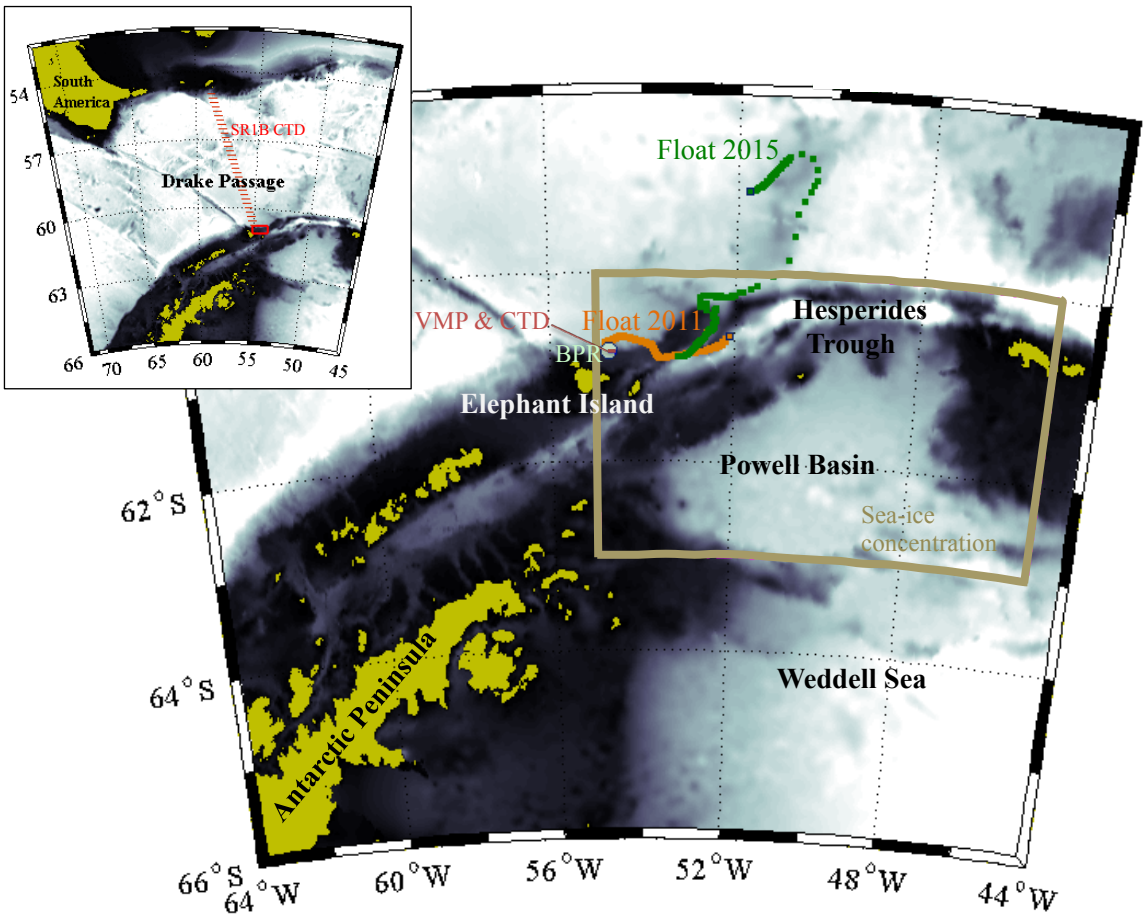

Figure 2.1: Maps showing the location of all instrument deployments and datasets used in this thesis. Inset: Drake Passage, with the SR1B track, which runs from south of the Faulkland Islands to Elephant Island, off the tip of the Antarctic Peninsula, labelled in red; the red boxed region near Elephant Island shows the location of the VMP and CTD timeseries, also marked on the main map. On the larger map, the 2011 and 1015 EM-APEX float deployments are marked in orange and green respectively; the BPR location is the mint-green dot and the region over which sea-ice concentration is averaged is within the brown boxed area.

2.4 Research Cruise JR305 (2015)

The above EM-Apex float was redeployed in 2015 (as float no. 4980b). The same float should have been redeployed by myself under principal investigator Miguel Angel Morales Maqueda on cruise JR292 from *RRS* James Clark Ross in 2014. However, despite the combined efforts of Jeffrey Pugh, Miguel Angel Morales Maqueda, myself and the many resourceful mechanics and engineers at Rothera Research Station who went to the lengths of making a specialist tool to open the instrument, we were unable to revive the float: the batteries were depleted due to a fault with the 'sleep' command hardware and available replacement batteries were of a different

weight and volume, rendering them impossible to fit and balance. The float was returned to the Webb Research Corporation (USA) for refurbishment and kindly redeployed by Yvonne Firing and Geoff Hargreaves the following season on 11 January 2015. This time, the float was deployed in westernmost Hesperides Trough with the aim of seeing whether it would capture Weddell Sea waters as observed in the 2011 deployment. The float profiled within Hesperides Trough before exiting north onto the continental slope where it profiled for a number of days before moving northwards into the open ocean and losing power on 2 February 2015. During this time, I worked closely with John Dunlap to respond to data and re-programme the float's depth boundaries and dive pattern to maximise useful output; it is possible to partially steer the float by making an assessment of horizontal velocities and isobaths. Data presented in this thesis are from continuously-profiling sections and are used only in Chapter 5.

2.5 EM-APEX Float Characteristics and Quality-Control

The EM-APEX measures horizontal velocities via an electromagnetic subsystem that comprises five electrodes, an accelerometer and a magnetic compass. The EM subsystem records relative velocities (± 0.015 m s $^{-1}$) in 2.2 m bins by measuring the motion-induced electric fields as the ocean moves through the vertical component of the Earth's magnetic field. These may be translated into absolute velocities using paired surfacing profiles' GPS locations. Velocities are used in Chapter 4 alone and are used only for computing shear, strain and potential vorticity, which do not require absolute velocities. The EM-APEX float was equipped with a pumped SeaBird Electronics CTD (so that no thermal lag correction was necessary) and measure temperature ($\pm$ 2 x 10^{-3} °C), conductivity ($\pm$ 2 x 10^{-3}) and pressure ($\pm$ 2 dbar). Data were quality controlled by:

1. checking for pressure drift (i.e all surface values are the same and applying an offset where not);

2. flagging bad pressure points (primarily near the top (upward-looking profiles) and bottom of profiles (downward-looking profiles) where the float overshoots the target depth);

3. comparing individual density, temperature and salinity profiles and checking whether spurious density inversions were the result of suspect salinity or temperature spikes and flagging bad data;

4. visually checking T-S diagrams against density profiles and flagging outliers;

Data considered 'bad' according to one variable was removed across all variables and interpolated over. T-S diagrams showing flagged datapoints are included in the supporting information at the back of relevant chapters.

2.6 Supplementary Data

The following publicly-available datasets are used to support the primary data: hydrographic data from the SR1B transect across Drake Passage (Chapter 3); the Bottom Pressure Recorder from Antarctic Circumpolar Current Levels by Altimetry and Island Measurements (ACCLAIM) at Elephant Island (Chapters 3, 5) and sea-ice concentrations from Passive Microwave Data from the National Snow and Ice Data Center (NSIDC) (Chapter 5). Additionally, barotropic and baroclinic tidal estimates are made from TPXO7.2 (Egbert *et al.* , 1994) (Chapters 3 and 4) and Tidal Model Driver (TMD) (Padman *et al.* , 2002) respectively. TPXO7.2 is a global model of barotropic tides which best-fits (according to least-squares) the Laplace Tidal Equations and the track-averaged altimeter data from two satellites, TOPEX/Poseidon and Jason, with an RMS of 5 cm. TPXO7.2 can be downloaded from http://volkov.oce.orst.edu/tides/global.html. TMD is a Matlab package for accessing the harmonic constituents of high latitude barotropic tide models. Here, it is run with the 1/30° x 1/60° (2 km) Antarctic Peninsula model (Model_AntPen), a high resolution regional model of the Antarctic Peninsula area from the middle of the Weddell Sea to west of Pine Island Bay. Computations are based on linearised shallow-water equations forced at open boundaries by tidal height from the circumpolar forward model CATS02.01 and astronomical forcing, and the model is particularly valuable for exploring tidal flows in narrow passages around the Antarctic Peninsula and islands near its tip (as used in Chapter 5). TMD for the Antarctic Peninsula can be downloaded from
https://mail.esr.org/polar_tide_models/Model_AntPen0401.html.

Chapter 3

Observations of a Diapycnal Shortcut to Adiabatic Upwelling of Antarctic Circumpolar Deep Water

This chapter presents high, intermittent diapycnal mixing at mid-depths over the Antarctic continental slope north of Elephant Island and proposes that observed mixing is forced by the locally-generated internal tide. Findings are discussed in the context of short-circuiting adiabatic upwelling as mid-depth mixing allows watermasses to transform at depth; influence on Southern Ocean overturning strength and the need for measurements and models to resolve processes at a sufficient temporal resolution to capture intermittent mixing.

Abstract

In the Southern Ocean, small-scale turbulence causes diapycnal mixing which influences important water mass transformations, in turn impacting large-scale ocean transports such as the Meridional Overturning Circulation (MOC), a key controller of Earth's climate. We present direct observations of mixing over the Antarctic continental slope between water masses that are part of the Southern Ocean MOC. A 12-hour time-series of microstructure turbulence measurements, hydrography and velocity observations off Elephant Island, north of the Antarctic Peninsula, reveals two concurrent bursts of elevated dissipation of $O(10^{-6})\mathrm{Wkg}^{-1}$, resulting in heat fluxes $\sim$10 times higher than basin-integrated Drake Passage estimates. This occurs across the boundary between adjacent adiabatic upwelling and downwelling overturning cells. Ray tracing and topography show mixing between 300-400m consistent with the breaking of locally-generated internal tidal waves. Since similar conditions extend to much of the Antarctic continental slope where these water masses outcrop, their transformation may contribute significantly to upwelling.

3.1 Introduction

The global overturning circulation, a critical component of the Earth's climate system, transports heat gained in the tropics to high latitudes, where it is lost to the atmosphere (Wunsch, 2004; Marshall & Speer, 2012). This circulation is sustained by ∼2 TW of mechanical energy input, of which approximately half comes from atmospheric winds and half from tides (Munk, 1966). Tide and wind energy force internal waves which dissipate energy to small-scale turbulence in vertical mixing events. The vertical exchange of heat and mass in the abyssal ocean balances deep water formation at high latitudes, maintaining abyssal stratification (Wunsch, 2004). However, observed background dissipation of $O(10^{-10})$W kg^{-1} is insufficient to balance deep water formation, suggesting that intense vertical mixing is concentrated at a few locations (Naveira Garabato *et al.* , 2004). The Southern Ocean, the key place where waters subducted or convected elsewhere rise to the surface to close the MOC, has recently come into focus as one such region of concentrated vertical mixing. Approximately 80% of the planet's wind energy is bound in storm tracks over the Southern Ocean (Zhai *et al.* , 2012) and this, coupled with topographic roughness and the action of tides, makes the Southern Ocean a potential hotspot for diapycnal mixing (Egbert *et al.* , 2004; Watson *et al.* , 2013; Wu *et al.* , 2011).

This study focuses on Drake Passage, a topographically complex chokepoint for ocean currents where elevated levels of tidally-forced diapycnal mixing can be expected (Heywood *et al.* , 2007; Padman *et al.* , 2006). Our measurements are taken to the north of Elephant Island, at the northern tip of the Antarctic Peninsula (Fig. 3.1a). M_2 tidal amplitudes (Padman *et al.* , 2002) and topographic roughness (Wu *et al.* , 2011) in the vicinity of Elephant Island are typical of the Antarctic continental shelf break equatorward of the M_2 critical latitude (∼74.5°S), accounting for ∼60% of the continental slope. At these latitudes, important watermass transformations occur as deep waters are drawn to the surface along tilting isopycnals where they are either transported northward by Ekman transports to form Antarctic Intermediate Water (AAIW) or South Antarctic Mode Water (SAMW), or lose buoyancy through air-sea fluxes near the cold continent and sink to form Antarctic Bottom Water (AABW) (Sloyan & Rintoul, 2001) (Fig. 3.1b). Although these transformations do not occur over all longitudes in the Southern

Ocean, Drake Passage is close to the site of Atlantic AAIW/SAMW formation (Piola & Gordon, 1989) and, immediately to the north of Elephant Island, dense waters formed along the eastern side of the Antarctic Peninsula convect downslope (Meredith *et al.* , 2003). While the return of deep waters to the surface along outcropping, inclined isopycnals is thought to dominate Southern Ocean upwelling, it has been suggested that such adiabatic processes are unable to account entirely for upward volume transports in the Southern Ocean, implicating diapycnal mixing as a contributor (Naveira Garabato *et al.* , 2007). Watson *et al.* (2013) estimate from a tracer-dispersion experiment that diapycnal mixing drives 20 - 30% of total Southern Ocean upwelling. We present the first time series of direct dissipation measurements to resolve strong intermittent diapycnal mixing episodes within the southernmost extent of Upper Circumpolar Deep Waters (UCDW), north of Elephant Island.

3.2 Measurements and Methods

From 18 to 29 November 2009, RRS *James Clark Ross* carried out a microstructure turbulence time-series (JR198) and the annually-repeated SR1B hydrographic survey from Burdwood Bank (south of the Falkland Islands) to Elephant Island across Drake Passage. Thirty-one full-depth conductivity-temperature-depth (CTD) stations were completed during the survey, culminating in a 12-hr station during which a free falling Rockland Scientific Instruments vertical microstructure profiler VMP-1000 (VMP hereafter), measuring turbulent kinetic energy (TKE) dissipation rates, repeatedly profiled off the northern coast of Elephant Island on 25 November (Figs. 3.1a, 3.2a). The VMP was equipped with microstructure shear probes, temperature and conductivity sensors and profiled simultaneously with a SeaBird Electronics CTD for independent, calibrated temperature and conductivity measurements. Fourteen such casts were accomplished, each approximately 800 m deep and taking 50 minutes from deployment to recovery. A shipboard 75 kHz RDI Ocean Surveyor acoustic Doppler current profiler (ADCP) measured velocities in 16-m bins with the first centred at a depth of 46.24 m, with bottom tracking off during the microstructure measurements, and was calibrated using water track data during post-processing into along- (u) and across-slope (v) components.

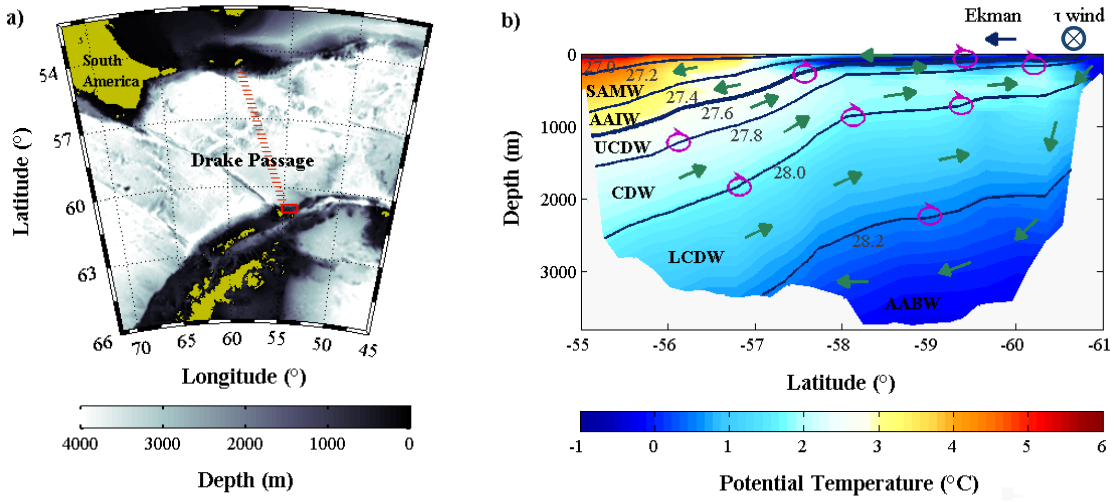

Figure 3.1: a) The location of the study site near Elephant Island is delimited by the red box. The red track marks the CTD transect across Drake Passage, the hydrography from which is used to construct schematic b) to illustrate meridional water mass transports across Drake Passage. Potential density (ρ - 1000 kg m^{-3}) is contoured, with the thicker line marking (isopycnal $\sigma = 27.6$ kg m^{-3}) the boundary between upwelling and downwelling cells of the Southern Ocean MOC. Green arrows show the mean overturning circulation: wind-driven northwards Ekman transport, northwards spread of waters cooled at the surface and sinking to form Antarctic Bottom Water (AABW) are all replenished by Circumpolar Deep Waters (CDW), Upper CDW (UCDW) and Lower CDW (LCDW) via adiabatic upwelling along isopycnals (e.g (Marshall & Speer, 2012; Sloyan & Rintoul, 2001)). Subantarctic Mode Water (SAMW) and Antarctic Intermediate Water (AAIW) are also formed within the Southern Ocean from subducting deep winter mixed layers. Pink recirculating arrows illustrate diapycnal mixing, a potential means for upwelling waters to short-circuit adiabatic pathways.

The barotropic tide is estimated from TPXO7.2 (Egbert & Erofeeva, 2002) (available from http://volkov.oce.orst.edu/tides/global.html) with the timing of high tide agreeing precisely with local bottom pressure recordings from Antarctic Circumpolar Current Levels by Altimetry and Island Measurements (ACCLAIM) data.

From ADCP velocities, square of shear was computed as the change in u and v velocity with depth, squared. Turbulent diffusivity is estimated after Osborn's relation (Osborn, 1980) as $K_\rho = \Gamma \frac{\varepsilon}{N^2}$, where ε is the dissipation rate from direct VMP measurements, buoyancy frequency N^2 is calculated from simultaneous CTD casts and Γ, the efficiency, is taken to be 0.2. The

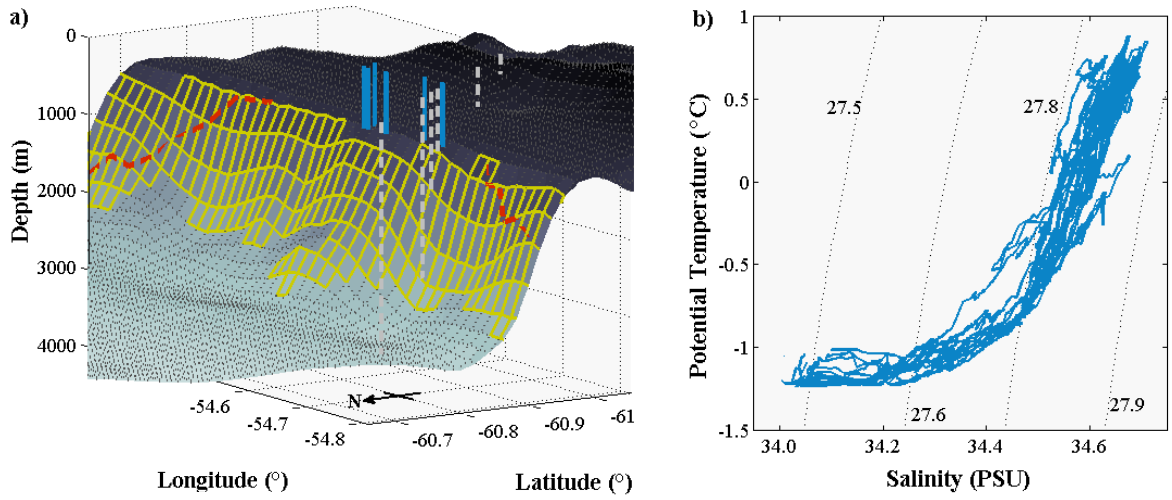

Figure 3.2: a) Nearby transect CTD stations (white dashed lines) and VMP-CTD casts (solid blue profiles) are superimposed upon topography (Amante & Eakins, 2009) using the same colour scheme as (Fig. 3.1a) as a reference to the bathymetry of the wider area. Casts drifted from west to east (right to left) along the shelf. Coordinate cells highlighted in yellow demarcate critical slopes according to the Baines parameter ($0.5<\gamma>2.0$) and thick, dashed red lines show the intersection of the M_2 ray path with critically-sloped topography. b) Temperature-salinity diagram.

Ozmidov length scale is computed as $(\frac{\varepsilon}{N^3})^{1/2}$ where N is the Brunt-Väisälä frequency. The M_2 ray slope ($\alpha = \sqrt{\frac{\omega^2 - f^2}{\langle N \rangle^2 - \omega^2}}$) is calculated from the internal wave dispersion relation where $\omega = 2\pi/12.42$ hrs^{-1} is the frequency of the M_2 tide; $f = -1.2737 \times 10^{-4}$ s^{-1} is the Coriolis parameter at this latitude; angle brackets denote time-averaged values; N^2 is derived from CTD casts corresponding to VMP casts for the upper 800 m of the water column and, below 800 m, from the final five ship's CTD transect stations (Fig. 3.2a). The Baines parameter is computed according to $\gamma = \frac{dH/dy}{\alpha}$ (Baines, 1982) where dH/dy represents the topographic slope in the ray propagation direction. Heat fluxes are computed from CTD temperatures as $F_h = \rho c K_\rho T_z$ where ρ is the potential density, $c = 4181$ J Kg^{-1} is the specific heat capacity of water and T_z is the vertical temperature gradient. Heat flux errors are computed from standard errors propagated through K_ρ and T_z as standard deviations and then normalised by $\sqrt{N}$ where N is the number of independent variables. Finally, the conversion of lee-wave energy flux to diapycnal

heat flux is calculated after Huang (1999) as $F = \frac{cbE/H}{g\alpha_w}$ where b is the fraction of mechanical energy used for mixing and is of the order 0.1; E is the mechanical energy flux; H is the depth of the water column; $g = 9.8$ m s^{-2} is the acceleration due to gravity and $\alpha_w = 0.167 \times 10^{-3}$ K^{-1} is the thermal expansion coefficient of water.

3.3 Results

Direct measurements of energy dissipation rates fall within the southernmost reaches of shoaling UCDW where it is drawn to the surface over the Antarctic continental slope. Here, northeastward-flowing currents dominate, following the shelf edge and the curve of the Antarctic Peninsula. At the VMP station, the shelf edge is approximately aligned in an east-west orientation (Figs. 3.1a, 3.2a), with a dominant eastward flow. The hydrographic CTD section is oriented in an across-slope sense with the VMP and simultaneous CTD casts aligned along-slope due to ship drift, and are confined within a 3 km^2 area (Fig. 3.2a). Analyses of temperature and salinity characteristics show a water mass of consistent properties at the margins of the UCDW class (Fig. 3.2b), with negligible variation along the slope relative to that across the slope. In zonal averages, isopcynal $\sigma = 27.6$ kg m^{-3} delineates the upper and lower Southern Ocean MOC cells (Lumpkin & Speer, 2007). In a 10-year-averaged SR1b hydrographic section (Fig. 3.1b), UCDW ranges from $\sigma = 27.6$ kg m^{-3} to $\sigma = 27.8$ kg m^{-3} with LCDW and the lower overturning cell found at higher densities.

3.3.1 Turbulent Kinetic Energy Dissipation, Mixing and Stratification

The VMP observations were collected over a 12-hr period with the intention of resolving the semi-diurnal tide (Fig. 3.3a). During this period, the surface tide cycled approximately from low through high to low water (Fig. 3.3b) with tidal current amplitudes of u <7 cm s^{-1} and v <2 cm s^{-1} and measurements taken between spring and neap phases of the tidal cycle.

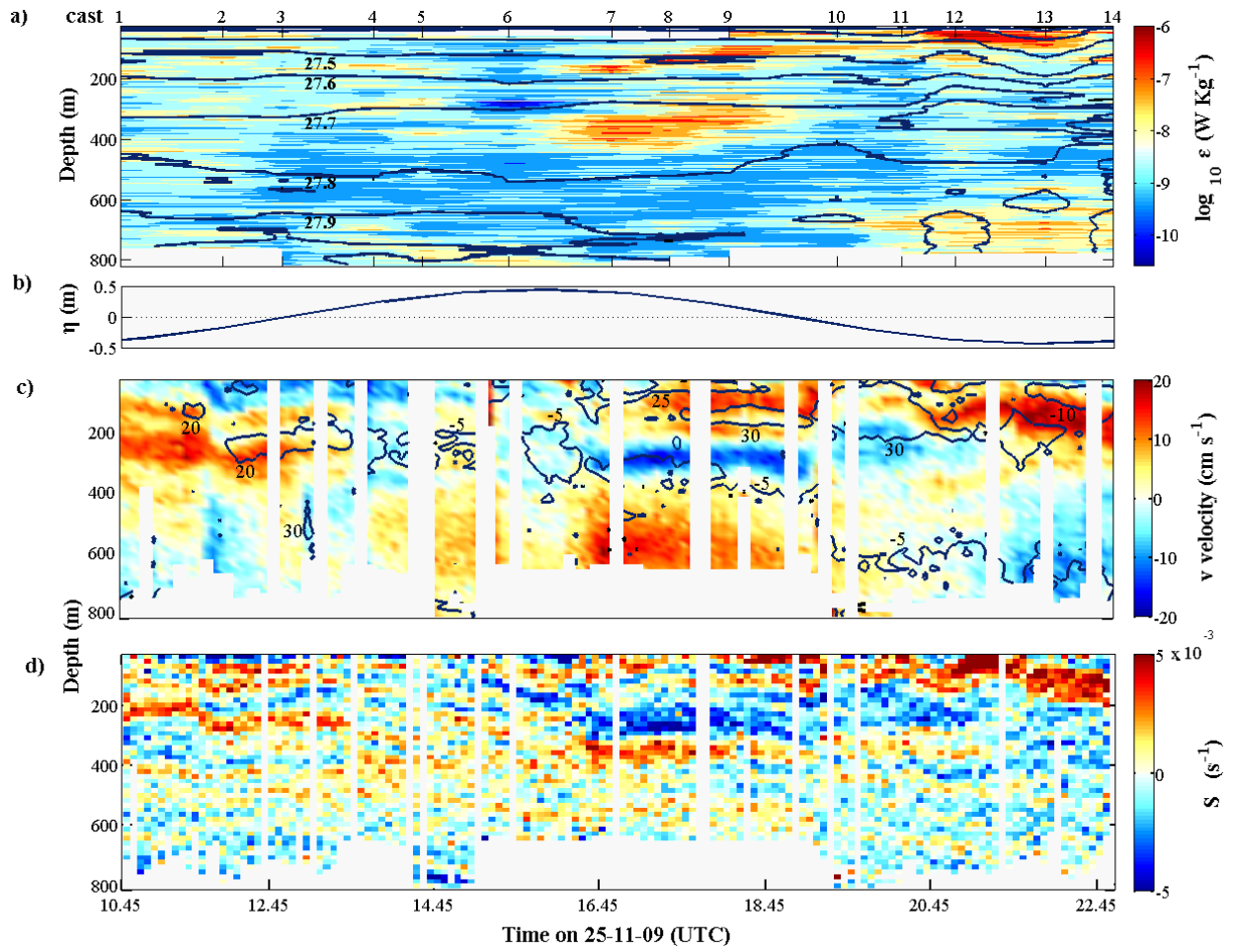

Figure 3.3: a) Time-series of the TKE dissipation rate, ε, from VMP casts with black contoured lines demarcating potential density (ρ - 1000 kg m^{-3}) measured by simultaneous CTD casts. b) Surface elevation due to semidiurnal M_2 tidal constituent from TPXO7.2. c) ADCP measurements of absolute v velocity in colour-filled contours with u velocity contours overlain in black, both with the depth-mean velocity subtracted. d) Bin-by-bin squared shear (S^2) computed from ADCP velocity data.

Relative to background dissipation levels of O (10^{-9}) W kg^{-1}, two separate bursts of elevated turbulent dissipation O (10^{-6}) W kg^{-1} were recorded between 16:30 and 19:00 UTC (casts 7 - 9), at depths of 120 - 200 m and 300 - 400 m. Relative to isopycnals, the upper patch of intense dissipation maintained a thickness of 25 - 30 m and shoaled progressively; the lower burst was confined between constant depths. Both persisted for approximately two hours, sampled by three consecutive VMP profiles. The isopycnal immediately below the lower dissipation event ($\sigma = 27.8$ kg m^{-3}) is displaced by 70 - 80 m, with the largest amplitude displacement coinciding with the maximum surface elevation of the semi-diurnal barotropic tide. Peak eddy diffusivities, K_ρ, of ~6 x 10^{-3} m^2 s^{-1} and ~1 x 10^{-3} m^2 s^{-1} compared with background diffusivities of <0.1

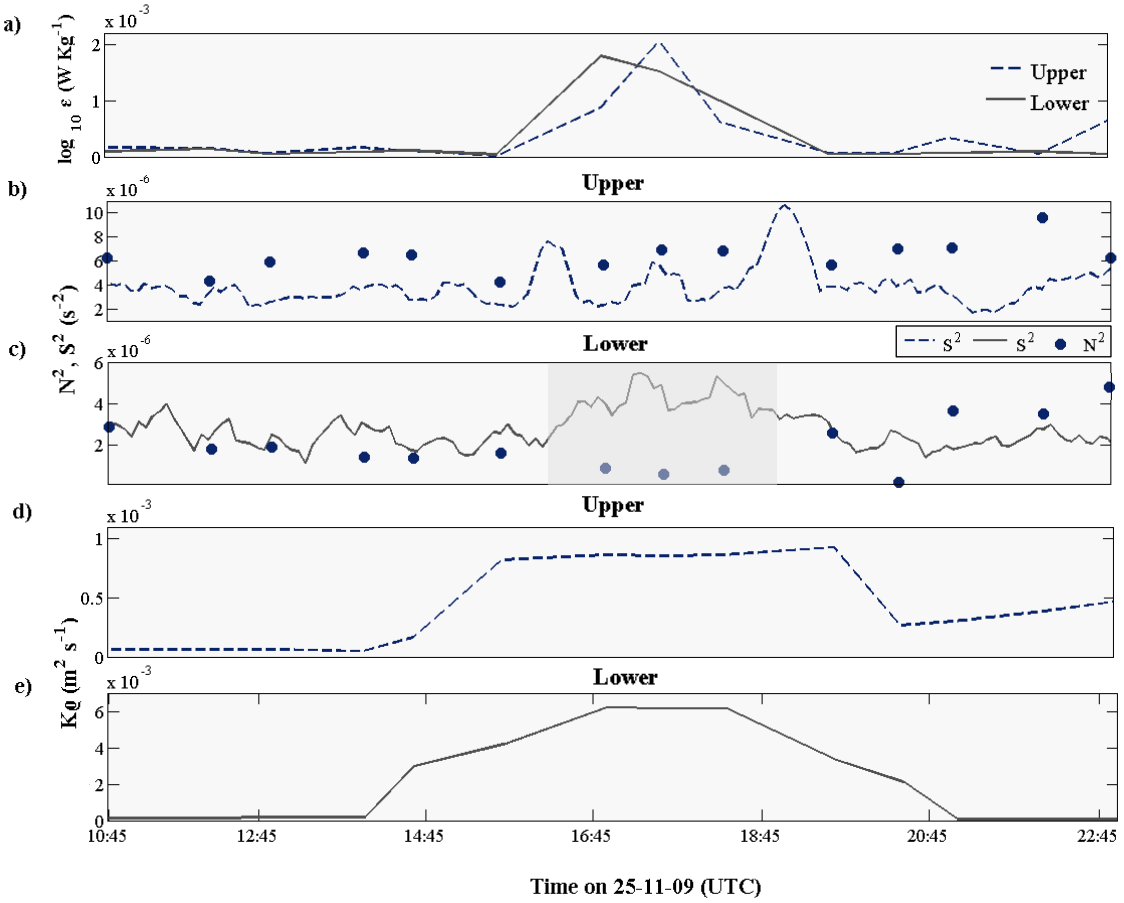

Figure 3.4: a) Total dissipation between 120 - 200 m (upper) and 300 - 400 m (lower). b-c) Buoyancy frequency, N^2 (dots), and squared shear, S^2 (lines), for upper (dashed lines) and lower (solid lines) bursts of dissipation, with the period where the Richardson number $N^2/S^2 < 0.25$ shaded in panel c). d-e) Estimated mean turbulent diffusivity between 120 - 200 m and 300 - 400 m, coincident with upper and lower bursts of dissipation respectively.

x 10^{-3} m^2 s^{-1} coincide with upper and lower bursts of dissipation respectively (Figs. 3.4a, b). Mixing events dominate the vertical heat flux at these depths averaging 25 $\pm$ 18 W m^{-2} during the upper burst and 58 $\pm$ 36 W m^{-2} during the lower event, significantly higher than average background levels of 3 $\pm$ 1 W m^{-2} and 4 $\pm$ 2 W m^{-2} respectively.

3.4 Current Velocities

The u and v velocity components, aligned in the along- and across-slope directions respectively, reveal a strong reversal in across-slope current direction at 250 - 300 m depth, coincident

with the timing of mid-depth dissipation events (Fig. 3.3c). This current reversal coincides temporally with isopycnic heave (Fig. 3.3a). The signature of the mid-depth v velocity reversal is clearly visible in the square of shear (Fig. 3.3d).

3.5 Discussion

This investigation focuses on the two distinctive bursts of dissipation $O(10^{-6})$ W kg^{-1}, which are $O(10^3)$ larger than background dissipation levels observed at mid-depths. Other instances of elevated dissipation were also captured, notably in the surface layer (casts 12-14) and the bottom boundary layer (casts 4-6; 11-14) with analyses (see supporting Fig. 3.6) revealing that near-surface mixing is consistent with shear-spiking from inertial energy input (Brannigan *et al.* , 2013) and that mixing lower in the water column may be attributed to bottom boundary layer processes, but their treatment is beyond the scope of this paper. Instead, the discussion is centred on elevated dissipation at mid-depths where upwelling occurs. Specifically, we speculate as to the origin of the energy available for driving turbulent dissipation and discuss the implications of these dissipation bursts on diapycnal mixing.

Of the upper and lower bursts of dissipation, the latter is associated with a greater diffusivity, K_ρ, of $\sim$6 x 10^{-3} m^2 s^{-1} above background levels compared to $\sim$1 x 10^{-3} m^2 s^{-1} in the upper case, where the rise in dissipation is accompanied by an increase in stratification (Figs. 3.4). This is reinforced by comparing the mean square of shear, S^2, and N^2 across the layers containing high dissipation, which reveals that the Richardson number falls to $<$0.25 during the lower dissipation burst only (Fig. 3.3c), so that only in this instance do the observations indicate that shear is sufficient to overcome stratification in turbulent mixing events. Shear instability may be driving the upper dissipation burst as well, but the Richardson number calculation is compromised by the low vertical resolution (16-m bins) of the 75 kHz ADCP which smooths higher *in situ* shear as the Ozmidov length scale during the upper burst is much smaller than bin-depth ($\sim$3 m), but sufficiently large during the lower burst ($\sim$15 m).

Three sources known to force the breaking of waves within the internal wave field are inves-

tigated: wind, tide and mesoscale eddies. Comparing the magnitude and alignment of bulk shear vectors across the strata containing high dissipation and the wind stress vector shows that directly wind-driven shear-spiking is unlikely to have provided the energy for mid-depth dissipation (see supporting Fig. 3.6). Temperature and salinity anomalies exhibit no significant correlation with velocity profiles within the velocity reversal periods suggesting that eddies are not responsible for the elevated levels of mixing. Moreover, mesoscale flows vary on timescales of days and longer, further reducing the likelihood of eddies as the cause of this feature. Several features indicative of a tidal signature cannot be conclusively resolved by observations that span only a single semi-diurnal period. Nevertheless, the isopycnic displacement occurs at close to the frequency of the M_2 tide (Figs. 3.3a, b) and there is a strong sinusoidal signal in the prominent v reversal close to the frequency of the semi-diurnal tide (Fig. 3.3b, c). Tidal models (Egbert *et al.* , 2004; Simmons *et al.* , 2004; Padman *et al.* , 2006) implicate the region as a globally significant dissipative site, while Heywood *et al.* (2007) show that internal tides are likely to be generated in Drake Passage from observations of tide-topography interactions, but emphasise their elusive detection there.

Internal tides are typically generated from the interaction of the tidal current with sufficiently sloped topography, propagating away from the generation site in a tidal ray refracted through the stratified ocean. Much of the sloped shelf edge north of Elephant Island is critical ($0.5 < \gamma < 2.0$) according to the Baines parameter categorisation of Robertson (2001) where $\gamma < 0.5$ is subcritical, $\gamma > 2.0$ is supercritical and a critical slope is the most likely to generate internal tides. Calculating the M_2 ray slope and tracing a radial path from the lower dissipative event to intersect with topography allows us to speculate as to whether locally generated internal tides could have been the driver of observed diffusivity. Assuming no reflection from the seabed, the sites where the M_2 ray path intersects critically sloped topography is shown in Fig. 3.2a. It is suggested that observed mid-depth turbulent diffusivity is consistent with the breaking of locally-generated internal waves forced by the tide.

Our background diffusivities near Elephant Island are directly comparable to basin-integrated estimates (based on tracer dispersion) of diapycnal diffusivity within Drake Passage UCDW by Watson *et al.* (2013) at 3.6 ± 0.6 x 10^{-4} m^2 s^{-1}, itself an order of magnitude higher than open

ocean background diffusivities. Our time-averaged diffusivities, including elevated dissipation events, are approximately five times larger than those associated with lee-wave generation in Drake Passage UCDW (Watson *et al.* , 2013), highlighting the importance of continental slope regions for diapycnal mixing.

Large heat fluxes of 25 ± 18 W m^{-2} and 58 ± 36 W m^{-2} resulting from upper and lower dissipation bursts respectively are at least an order of magnitude greater than time-series background fluxes of 3 ± 1 W m^{-2} and 4 ± 2 W m^{-2}. Consequently, dissipation bursts dominate the time-series averaged fluxes of 8 ± 4 W m^{-2} (upper) and 16 ± 8 W m^{-2} (lower). These heat fluxes, compared with fluxes of ∼0.4 W m^{-2} across isopycnal $\sigma = 27.4$ kg m^{-3} in the Atlantic sector of the Southern Ocean (computed using transports of 4 Sv and $\Delta T \approx 2.5$°C from Sloyan & Rintoul (2001)), are very large. Although this comparison is made across a different isopycnal than that which our fluxes straddle ($\sigma = 27.6$ kg m^{-3}), it is globally representative of the boundary between water masses we observe to have modified properties locally and is the most relevant of the scarce historical estimates for mixing in the Southern Ocean. From the basin-integrated lee-wave energy flux of 0.02 W m^{-2} given for Drake Passage UCDW in Watson *et al.* (2013), the equivalent heat flux is calculated after Huang (1999) to be ∼5 W m^{-2}, assuming a depth of 1000 m. This is comparable with our background fluxes, while our peak fluxes are ∼10 times larger.

The presence of high dissipation rates suggests that diapycnal mixing plays a role in the transformation of upwelling UCDW at Elephant Island. While the prevailing view that the primary mechanism for upwelling in the Southern Ocean, the wind-driven adiabatic transport of mass along inclined, outcropping and narrowing isopycnals requires no energy to be dissipated (Marshall & Speer, 2012), adiabatic pathways are unable to account entirely for upward volume transports here. It has been proposed that vertical mixing across isopycnals and indeed between adjacent upwelling and downwelling water masses is a means of short-circuiting adiabatic upwelling (Naveira Garabato *et al.* , 2007). Our observations provide evidence for the presence of strong intermittent diapycnal mixing, where adiabatic upwelling occurs, across isopycnals that generally divide the upper and lower Southern Ocean MOC cells (*circa* $\sigma = 27.6$ kg m^{-3}) in a circumpolar sense. Mixing within the water masses at the interface of the two South-

ern Ocean overturning cells may allow water mass transformation to occur at depth instead of at the surface following adiabatic upwelling. These isopycnals typically outcrop between ∼60°S and ∼70°S, approaching the Antarctic continental slope along the Antarctic Peninsula and between ∼45°E and ∼145°E, south of Australia (Marshall & Speer, 2012). Given that similar topographic roughness and M_2 tidal amplitudes extend to ∼60% of the Antarctic continental slope and coincide with where the outcropping of UCDW and LCDW approaches the slope, intermittent, tidally-driven mixing across the UCDW-LCDW interface may also occur elsewhere.

Although limited to narrow shelf break regions and intermittent, such elevated diapycnal mixing may drive the missing mid-depth water mass transformation of Watson *et al.* (2013), influencing our understanding of Southern Ocean overturning strength. The broad implications of diapycnal mixing at this location for Southern Ocean water mass transformations and upwelling rates drawn from this short time-series deserve further investigation and it is significant that we have identified a place where this can be studied.

3.6 Conclusions

A 12-hour time-series of TKE dissipation rates in which we observe elevated intermittent mixing across the boundary between adjacent adiabatically upwelling and downwelling branches of the Southern Ocean MOC is investigated. Two concurrent bursts of elevated dissipation of $O(10^{-6})$ W kg^{-1} between 120 - 200 m and 300 - 400 m are associated with high diffusivity and significant vertical heat fluxes that dominate time-series average fluxes of 8 ± 4 W m^{-2} and 16 ± 8 W m^{-2} and are significantly higher than regional estimates. The lower event appears consistent with the breaking of locally-generated internal tidal waves through shear instability. Our observations provide evidence that intermittent diapycnal mixing has led to large heat fluxes in upwelling regions. While the contribution of diapycnal mixing to upwelling *per se* at this location has not been quantified, the mixing of tracers has implications for water mass transformations. Yet if intermittent diapycnal mixing at such key locations has the potential to influence upwelling

rates, and moreover if it occurs elsewhere along the Antarctic continental slope, this may have far-reaching consequences for the strength of the MOC. This short time-series demonstrates the importance of continental slope regions for diapycnal mixing and identifies a place where the contributions of adiabatic and diapycnal mixing processes to upwelling should be studied. Finally, the large range in heat fluxes over the time-series highlights the need for further studies resolving variation on sub-inertial and sub-tidal timescales to elicit underlying processes.

3.7 Acknowledgments

We thank the officers and crew of the RRS *James Clark Ross* and the British Antarctic Survey IT and ETS personnel for their support during the science cruises JR195 and JR198. This work was carried out under the auspices of NERCs National Capability project, ACCLAIM. Additionally, JMS was supported by NERC studentship (NE/K500938/1); YDL by NERC Fellowship (NE/H016007/1); JP by NOC Modelling National Capability, FASTNEt (NE/I030259/1) and Irish Sea Observatory National Capability; MAMM by OSCAR (NE/I022868/1); TPR by TEA-COSI (NE/1029226/1) and OSMOSIS (NE/1019794/1). Data can be requested from the British Oceanographic Data Centre, BODC. Finally, we thank two anonymous reviewers for constructive comments that led to a substantially improved manuscript.

3.8 Supporting Information

This section contains supporting information for Chapter 3, including supplementary plots for the reader's interest and expansions on analyses 'not shown' in the original published manuscript. The contents are as follows:

1. the temperature and salinity along-slope sections from shipboard CTD profiles cast simultaneously with VMP profiles and
2. an explanation of and the plots used for the mentioned wind-driven shear-spiking analysis.

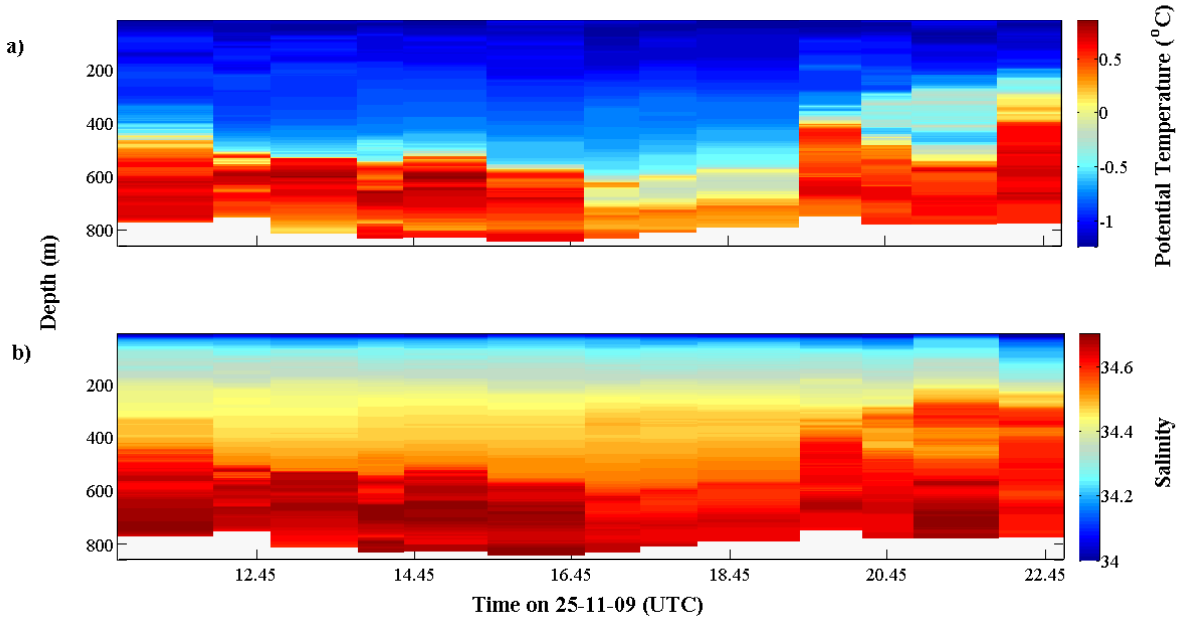

Figure 3.5: a) Potential temperature and b) salinity as measured by CTD casts carried out at the same time as VMP casts along the slope at Elephant Island. Both are presented as time-series but so that the measurements taken by each of the 14 casts are clearly attributed to each respective cast.

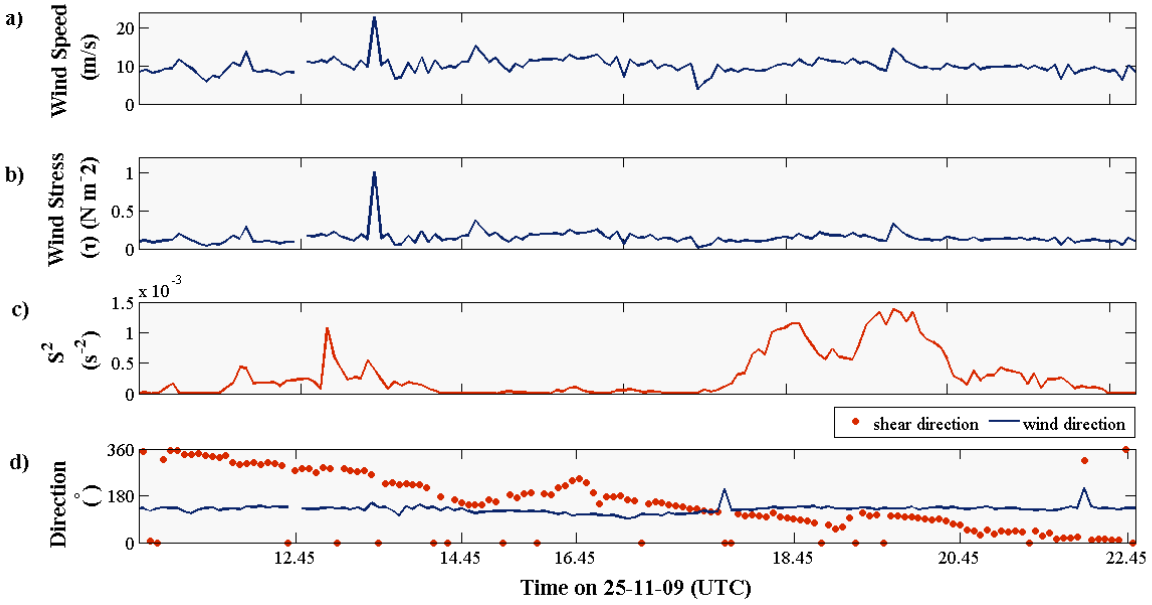

Figure 3.6: a) wind speed and b) associated wind stress (after Large & Pond (1981)) are compared to c) the square of shear across the mixed-layer depth according to Kara & Hurlburt (2000)'s diagnosis and d) the direction of the wind stress and shear vectors.When wind stress and shear vectors align at the base of the surface mixed-layer and wind stress is elevated, shear-spiking can occur. The described upper and lower dissipation events occur between approximately 16.30 and 19.00 hours on 25-11-09, which is not consistent with shear-spiking. Note that these dissipation events are recorded approximately an hour before the wind stress and shear directions align and the magnitude of shear begins to build, whereas the dissipation does not intensify at this point. However, near the surface, dissipation begins to rise after approximately 18.30 hours on 25-11-09, coinciding with the alignment of wind stress and shear vectors and the building of shear magnitude.

Chapter 4

Watermass Transformation at Mid-depths over the Antarctic Continental Slope

In this chapter, observations of watermasses transforming over the continental slope near Elephant Island at mid-depths are presented as an UCDW lens (likely an eddy) loses heat, mass and buoyancy to LCDW beneath, via shear-driven turbulent mixing across its lower boundary. It is suggested that symmetric instabilities arise around the lower boundary due to vortex-stretching by the baroclinic tide. This is discussed in terms of diabatic contributions to Southern Ocean upwelling and its relevance as a mechanism for warm-core UCDW eddies, which are prevalent along the Western Antarctic Peninsula, to supply heat to mid-depth waters over the shelf-break where the West Antarctic marine glacier melt is sensitive to ocean heat content. It is noted that general circulation and coupled ice-ocean models do not always capture these submesoscale features.

Abstract

The Meridional Overturning Circulation (MOC) controls the global oceans' latitudinal heat distribution, helping to regulate the Earth's climate. The Southern Ocean is the primary place where cool, deep waters return to the surface to complete this global circulation. While water mass transformations intrinsic to this process predominantly take place at the surface following upwelling, recent studies implicate vertical mixing in allowing transformation at depth over the Antarctic continental slope. EM-APEX float observations near Elephant Island, north of the Antarctic Peninsula's tip capture direct heat exchange between a lens of Upper Circumpolar Deep Water (UCDW) and surrounding Lower Circumpolar Deep Waters (LCDW) at mid-depths over the course of several days as it propagates along the slope. Peaks in diffusivity estimated from a shear-strain finestructure parameterisation and heat fluxes are associated with shear instability. Two-dimensional Ertel potential vorticity is elevated inside the UCDW lens and across its bottom boundary, with a strong contribution from the shear term in these regions. The alternating sign of the potential vorticity along the bottom boundary implicates symmetric forcing and we posit that the UCDW lens is deformed by tidally-induced vortex stretching, enhancing submesoscale instabilities around its bottom boundary. Hence waters mix across this boundary so that heat, mass and buoyancy are lost from UCDW to the LCDW beneath, providing direct evidence of water mass transformation at mid-depths over the Antarctic continental slope. This has implications for our understanding of rates of upwelling and ocean-atmosphere exchanges of heat and carbon at this critical location. Further, our observations demonstrate a mechanism by which UCDW-core eddies along the Western Antarctic Peninsula may contribute to on-slope heat dispersion at mid-depths in regions where the melting of marine glaciers is linked to ocean heat content.

4.1 Introduction

The meridional overturning circulation (MOC) is responsible for the way heat, freshwater and carbon are stored and transported around the globe, controlling the Earth's climate. The Southern Ocean limb of the MOC plays a key role in returning waters subducted elsewhere to the surface, completing the global overturning circulation. Water masses critical to this circulation outcrop over the Antarctic continental slope and are transformed either by surface fluxes following upwelling or by vertical mixing at mid-depths. At the surface, upwelled waters are transformed as they lose heat to the atmosphere near the cold continent, sinking to form Antarctic Bottom Water (AABW), or are deflected northward by wind-driven Ekman transports. Surface waters are replenished by deeper waters along upward-tilting isopycnals, a largely wind-driven process known as adiabatic upwelling (see schematic Fig.4.1b, (Marshall & Speer, 2012)) and is a combination of wind-driven Ekman pumping and isopycnic eddy mass flux; the remainder (20 - 30%) is attributed to diapycnal mixing (Watson *et al.* , 2013).

The exchange of properties between water masses across their dividing isopycnals and even between upwelling and downwelling overturning cells can short-circuit the adiabatic pathway (Naveira Garabato *et al.* , 2007; Mead Silvester *et al.* , 2014). These mid-water watermass transformations influence the total buoyancy budget of the circulation (Polton & Marshall, 2007) and subtly influence the rate of upwelling and so the rate at which both heat and the Southern Ocean's deep, carbon-rich waters communicate with the atmosphere.

Warm, salty UCDW is found along the steep continental slope near Elephant Island, at the northern tip of the Antarctic Peninsula (Fig.4.1a). Here, the isopycnals that circumpolarly divide upper and lower overturning cells outcrop (Lumpkin & Speer, 2007; Marshall & Speer, 2012) (Fig.4.1b) and, below, dense waters convect downslope (Meredith *et al.* , 2003). Previous observations along this slope resolve intense, intermittent mixing across the interface between overturning cells consistent with forcing from internal tides (Mead Silvester *et al.* , 2014).

Along the Western Antarctic Peninsula (WAP), UCDW extends onto the slope either as UCDW tongues or as eddies shed from the Antarctic Circumpolar Current (ACC) further north. The

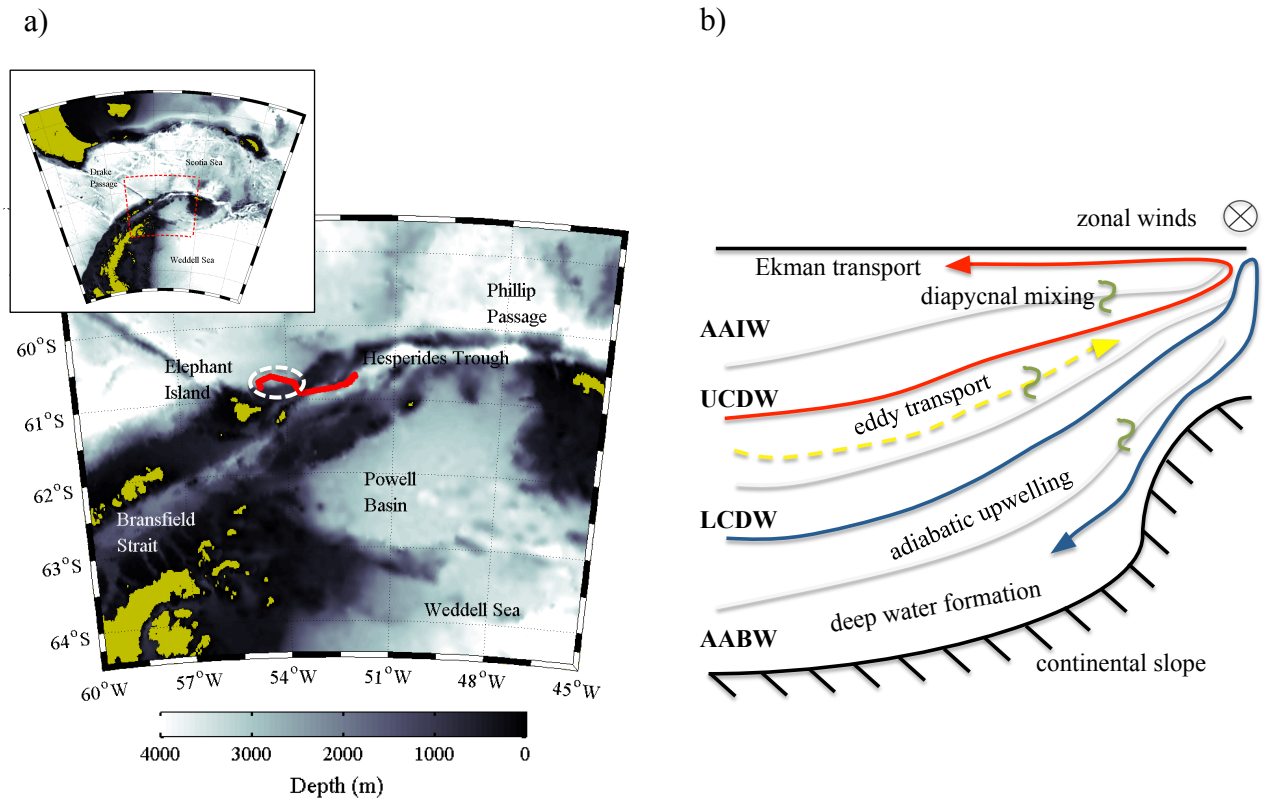

Figure 4.1: a) The EM-APEX float trajectory (red) from deployment near Elephant Island, in South Drake Passage (inset). The float drifted eastward along the steep continental slope before entering Hesperides trough. The white, dashed circle highlights the along-slope section under discussion. b) The mean overturning is depicted by red and blue arrows, the upper and lower overturning cells respectively. Waters upwell adiabatically, driven by the wind-driven overturning Deacon cell, which tilts isopycnals poleward, and an eddy cell which overturns in the equal yet opposite sense and acts to flatten them out, resulting in inclined, narrowing isopycnals that outcrop over the continental slope. UCDW and LCDW upwell along these layers towards the surface where they are either deflected north by Ekman transports to form Antarctic Intermediate Waters (AAIW) as deep winter mixed layers are subducted, or they lose buoyancy (heat) to the atmosphere through air-sea fluxes near the cold continent and sink to form Antarctic Bottom Water (AABW). Green squiggles show diapycnal mixing across isopycnals and between water masses, a means of short-circuiting the adiabatic upwelling pathway and subsequent transformations.

vertical exchange of heat along the base of these warmer water masses must be an important mechanism in dispersing their heat onto the shelf, which has been linked to the observed increase in mid-depth ocean heat content along the WAP (Martinson & McKee, 2012). The increase in mid-depth ocean heat content plays a critical role in the recent marine glacier retreat along the WAP (Cook *et al.* , 2016). It is thought that warmed LCDW is transported, via deep canyons in the shelf, into direct contact with the base of ice shelves at the coast (Moffat *et al.* , 2009) and that the principal pathway of warm water onto the slope is via UCDW-core eddies (Martinson & McKee, 2012).

We present new observations that show the time-evolution of a lens of UCDW, likely an eddy, at mid-depths over the Antarctic continental slope. Given that the Rossby Radius is 5.3-6.4 km (i.e a mesoscale eddy would be of a minimum diameter of 10.6-6.4 km) and the lens is 2.4-4 km diameter, we suppose that the lens is a submesoscale feature, though it should be remembered that lateral gradients are poorly resolved here. We investigate how the baroclinic tide interacts with the UCDW lens to enhance submesoscale instabilities and vertical mixing to effect the transformation of the UCDW lens and the LCDW below.

4.2 Methods

4.2.1 Instruments and Data

An autonomously profiling EM-APEX float (no. 4980a) was deployed from RRS *James Clark Ross* on cruise R264 on 5 December 2011 immediately north of Elephant Island (Fig.4.1a). The float profiled vertically and continuously between 400 m and 900 m, with each up-down cycle lasting approximately 1 hr 45 mins, and surfaced every other day until recovery on 17 December, 12 days later. Data are sent, and instructions received, via iridium link at the surface. The section under discussion runs from 6 -11 December, when the float followed the continental slope eastward, before crossing a bathymetric ridge and entering Hesperides Trough. As the EM-APEX float profiled, *in situ* measurements of temperature ($\pm$ 2 x 10^{-3} °C), conductivity ($\pm$ 2

x 10^{-3}) and pressure ($\pm$ 2 dbar) were recorded by a pumped SeaBird Electronics CTD in 2.2 m vertical bins. Horizontal velocities were derived from the onboard electromagnetic subsystem and processed onshore into zonal and meridional velocities in 3 m vertical bins. Profiles were visually checked for surface pressure consistency and any bad pressure points, which tend to occur near the top and bottom of profiles, were removed. Outlying values of temperature and salinity were flagged using T-S diagrams and visually evaluated against density profiles; in rare instances of bad data, points were removed and interpolated over. Supproting Fig.4.10 shows the flagged data and the subsurface float trajectory.

4.2.2 Velocities

The continental slope here is oriented such that the along-slope direction is notationally eastwards and the off-slope direction is notationally northwards (Fig.4.1a). The along-slope, U, and across-slope, V, velocity anomalies are calculated relative to the time-mean profile at each depth. Depth-mean along- and across- slope velocities within the UCDW lens are also presented.

4.2.3 Heat Content and Heat fluxes

The temperature anomaly relative to the time-mean profile within the UCDW lens is compared to that of the LCDW that lies between the the bottom boundary of the UCDW lens and isopycnal 27.78 kg m^{-3} (Fig.4.2a); where the 27.78 kg m^{-3} lower bounding isopycnal for LCDW is not captured, the deepest limit of the float profile is used as the lower boundary. The depth-integrated heat content is computed as $Q = \int \rho C_p T dz$ where ρ is the potential density (relative to the surface density), C_p is the specific heat capacity of seawater, T is the potential temperature and z is depth. The rate of change in heat content equivalent to the heat flux between UCDW and LCDW is computed as $F = \frac{\partial}{\partial t}(\rho C_p \int T_{(z)} dz)$ where t is time and vertical fluxes are down a gradient across the top and bottom boundaries of the UCDW lens from the temperature maximum inside to the temperature minimum outside. For each profile, the

temperature maximum is used to represent the core of the UCDW lens and, for consistency, the temperature minimum within LCDW is used as the deep integral limit; this contour closely follows isopycnal 27.78 kg m^{-3}. Heat and freshwater (salt) fluxes follow a similar temporal pattern (see supporting Fig. 4.7b - c) and heat fluxes across the top and bottom boundaries are of a similar magnitude and peak at similar times (see supporting Fig. 4.7 b - c). However since the top of the lens is only just captured by the float, fluxes across the top boundary are not adequately resolved, they are not discussed hereafter.

4.2.4 Dissipation, Diffusivity and the Gradient Richardson Number

Diffusivity is estimated from heat fluxes across the bottom boundary, again from the maximum temperature inside the UCDW lens to the minimum temperature beneath, according to $k_{flux} = \frac{F}{-\rho C_p dT/dz}$. For comparison, diffusivity is also estimated from dissipation according to shear-strain parameterisation after Meyer *et al.* (2014, 2015) and used to estimate diffusivity according to Osborn's relation (Osborn, 1980), $k_{shear-strain} = \Gamma \frac{\varepsilon}{N^2}$, where ε is the dissipation rate and $\Gamma = 0.2$ is the mixing efficiency. The gradient Richardson number is $Ri = \frac{N^2}{S^2}$, where N^2 is the buoyancy frequency and the $S^2 = (dU/dz)^2 + (dV/dz)^2$ is the shear-squared.

4.2.5 Ertel's Potential Vorticity and Gravitational Instability

Ertel's potential vorticity (EPV) is used to identify regions of instability. Since the emphasis of analysis here is on the relative spatial distribution of EPV and density is available only in the along-slope direction, the two-dimensional potential vorticity is approximated from an adaption of Thompson *et al.* (2014)'s formula as $EPV_{2D} = fb_z - V_z b_x + V_x b_z$ where $f = -1.27 \times 10^{-4}$ s^{-1} is the Coriolis parameter at this latitude; V is the across-slope velocity; and $b = -g\rho/\rho_o$ is the buoyancy in which $g = 9.8$ m s^{-2} is the acceleration due to gravity; ρ is the potential density and ρ_o is the reference density averaged from recorded surface values (not shown in Fig.4.2a); and subscripts denote partial derivatives with z increasing upwards and x increasing eastward in the on-slope direction. Positive EPV denotes regions of instability. The relative contribution

of the planetary term (fb_z) and the shear term ($-V_z b_x + V_x b_z$) to EPV_{2D} are evaluated, and the balanced Richardson number is computed to diagnose instabilities after Thomas *et al.* (2013) as $Ri_B = \frac{f^2 N^2}{M^2}$ where N^2 is the buoyancy frequency and M is the smoothed lateral buoyancy gradient, $\mid \bigtriangledown_h b \mid$. The rotational sense of shear within the UCDW lens is predominantly, yet weakly, anticyclonic and is presumed so when analysing instabilities from the balanced Richardson number.

4.3 Results

The continental slope lies approximately in an east-west orientation so that zonal and meridional velocities translate into the along-slope, U, and across-slope, V, directions respectively, with the dominant eastward flow determining the EM-APEX float's trajectory (Fig.4.3a,b). Analyses of temperature, salinity and potential vorticity characteristics show two markedly different water masses: UCDW and LCDW (Fig.4.2a). Initially, the float profiles within warm, salty UCDW, until an abrupt change in the direction of the EM-APEX float on 12/06 precipitates a transition into cooler, fresher LCDW with a distinct, 200 m thick lens of UCDW propagating along the slope within it. Supporting Fig. 4.8b shows that the waters of this lens are distinct from surrounding waters.

A semi-diurnal signal dominates the barotropic tide (Fig.4.3c, TPXO7.2), but is close to the inertial frequency at this latitude, and the lower boundary of the UCDW lens appears to be modified in the vertical plane at a semi-diurnal frequency, which dominates the thickness of the lens (Fig.4.2b). At these latitudes, it requires a longer timeseries than ours to separate the inertial and M_2 frequencies, but supporting Fig.4.8b shows that there is a broad hump around the semi-diurnal frequency in the temperature signal across the depths of the bottom boundary of the lens. Despite a sense of anticyclonic rotation, analysis of the EM-APEX float velocities do not bear a clear signature of an eddy (Fig.4.3d,e). This is likely because the spatial sampling of the lens is pseudo-Lagrangian and would not resolve the eddy cross-section well. However, onshore-propagating eddies originating from offshore CDW masses and with similar

characteristics have been observed over the continental slope nearby to the west (Martinson & McKee, 2012) and to the east (Thompson *et al.* , 2014) and the UCDW lens in this study is characterised by similar temperature and salinity properties to an UCDW mass sampled offshore and further west (Fig.4.2a).

Across-slope velocities throughout the water column vary with the diurnal tide (Fig.4.3b,c), so that the entire water column is pushed laterally onto the slope during high tide, and retreats at low tide: this relationship is clearer in the velocity signal within the UCDW lens (Fig.4.3c, e). This is also supported by the diurnal signal in the tidal elevation (Fig. 4.3c) and the diurnal tidal ellipses, the dominant axes of which are aligned perpendicularly to the continental slope at our study site (see supporting Figs. 4.9b,d). We suggest that the diurnal tide advects the entire water column (lens included) onto and off the continental slope in the horizontal plane, while the semi-diurnal tide modifies the bottom boundary of the lens in the vertical plane.

4.3.1 Heat Content and Heat fluxes

As the UCDW lens propagates eastward along the slope, it loses heat; total depth-integrated heat content over the last day is 46% lower than over the first day. Figs.4.2c and 4.2g shows a clear heat exchange between UCDW within the lens and the LCDW below, in phase with the deepening and shoaling of the lower boundary of the UCDW lens. At its deepest extent, the UCDW temperature anomaly peaks (see dashed lines, Fig. 4.2c), followed by an immediate rise in the temperature anomaly of the LCDW below and a synchronous drop in UCDW temperature anomaly. These events are associated with peaking heat fluxes (see supporting Fig. 4.7c) and bursts of warming occurring at the UCDW-LCDW interface signified by warmer datapoints migrating into waters of higher density (Fig. 4.2g).

4.3.2 Dissipation, Diffusivity and Shear Instability

For rigour, depth-mean diffusivities across the bottom boundary of the UCDW lens from shear-strain finescale parameterisation and heat flux estimates are compared (Fig.4.2d). While the

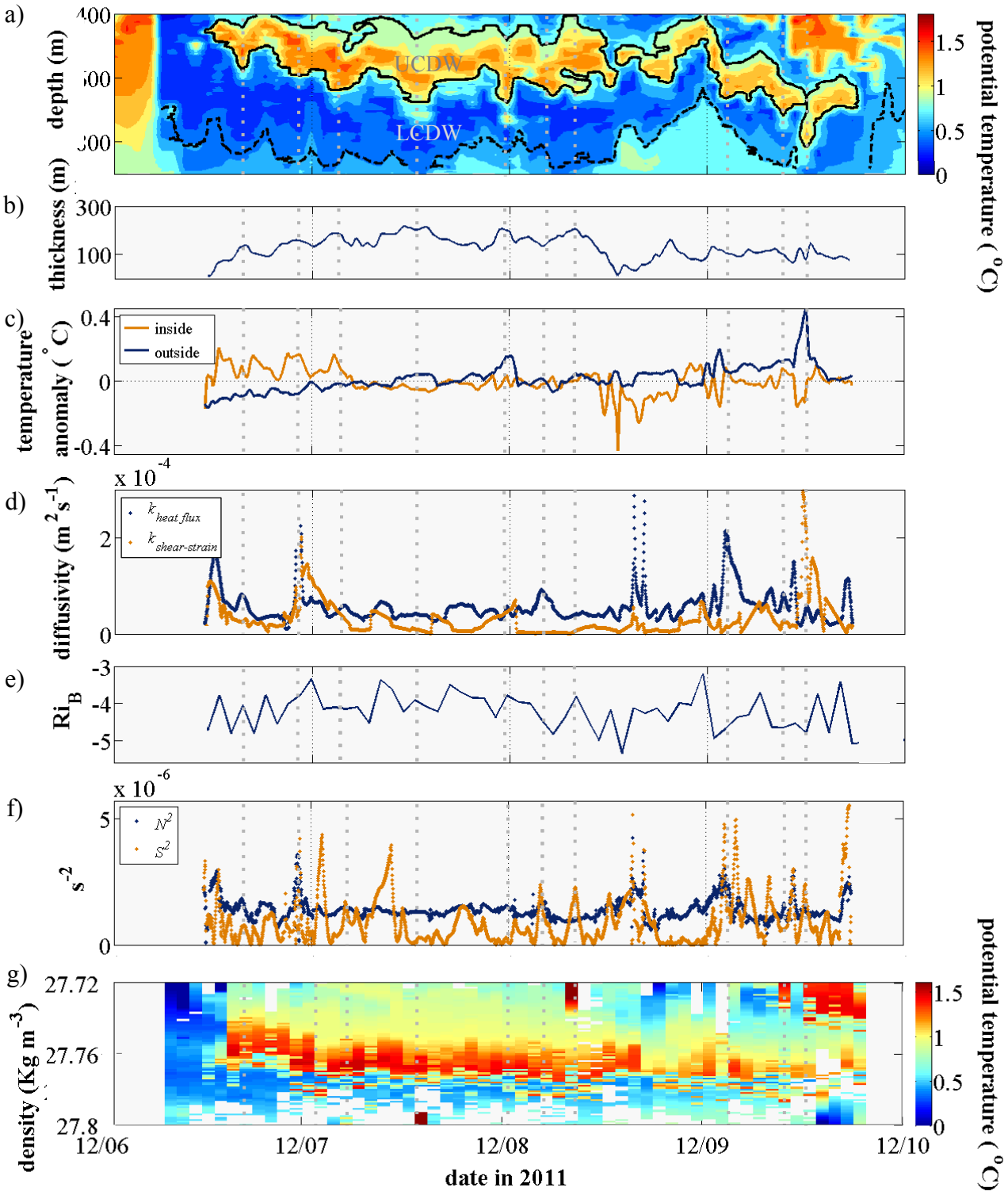

Figure 4.2: a) potential temperature of the along-slope section. Initially the float samples UCDW throughout the profiles, then a lens of UCDW, defined by its bounding isopycnal 27.77 kg m^{-3} (thick black line), propagating through LCDW; b) thickness of the UCDW lens; c) temperature anomaly relative to the time-mean profile within the UCDW lens and within the LCDW beneath between the bottom boundary and isopycnal 27.8 kg m^{-3} (thick dashed line in b); d) diffusivity estimated from shear-strain and heat flux calculations across the bottom boundary of the UCDW lens; e) the depth-averaged balanced Richardson number, Ri_B; f) comparing vertical shear-squared (S^2) and the buoyancy frequency (N^2). Where $S^2 \geq N^2$, the Richardson number $Ri \leq 1$. g) scatter of temperature profiles in density-space. Dashed grey lines facilitate comparison between the isopycnic heave of the lower boundary (b), heat exchange (c), estimated diffusivity (d) and $S^2 : N^2$

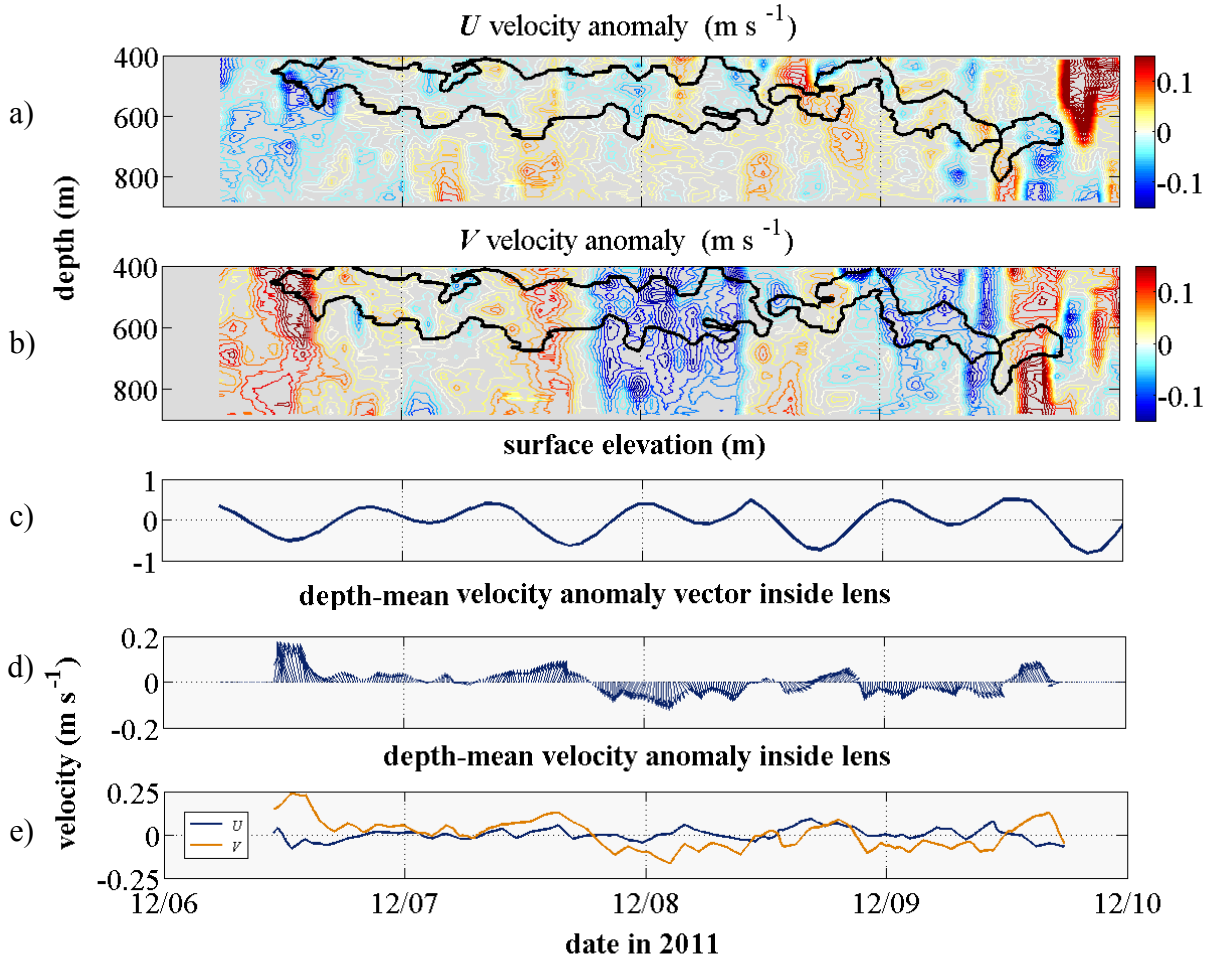

Figure 4.3: a) Along-slope, U, velocity anomaly; b) across-slope, V, velocity anomaly; c) the surface elevation of the barotropic tide; d) depth-mean velocity relative to the time-averaged velocity (i.e velocity anomaly) vector within the UCDW lens and e) the depth-mean velocity anomalies within the UCDW lens.

two estimates pick up similar peaks (Fig.4.2d), the heat-flux method tends to be more closely associated with the deepening of the UCDW lens's bottom isopycnal (Fig. 4.2a,d) with shear-strain methods estimating lower diffusivities in general, but illustrating the high dissipation associated with the UCDW lens compared to surrounding waters (see supporting Fig. 4.7d). These values are compared across the bottom boundary only, due to loss of data points across the top boundary in the shear-strain calculation. Shear instability can be expected for $Ri \leq 1$, where $S^2 \geq N^2$ in Fig.4.2f, and is the usually the case where diffusivities peak, although there are instances where $Ri \leq 1$ and diffusivities are not elevated (Fig.4.2d). Events where $Ri \leq 1$ but diffusivity is not enhanced appear to coincide with velocity reversals across the bottom boundary (Fig.4.3a,b), but this is beyond the scope of this paper.

4.3.3 Ertel's Potential Vorticity and Gravitational Instability

The EPV_{2D} is $O(1)$ higher inside than outside the UCDW lens and is visibly higher inside the lens than immediately beneath it, forming a gradient across the lower boundary, around which EPV_{2D} peaks (Fig. 4.4b) and alternates between positive and negative over time (Fig.4.4a). The EPV_{2D} is also higher within the second evolution of the lens (12/08 - 12/09) than in the first (12/06 - 12/08). Figs 4.4b-d show the relative contributions of the planetary and shear terms to EPV_{2D}, in which the shear term appears to contribute much to the cross-boundary intensification of potential vorticity. Instabilities are expected to arise from pure gravitational forcing where $Ri_B \leq -1$, as across the top boundary of the UCDW lens, progressively tending towards forced symmetric instability for $0 \leq Ri_B \leq 1$ and anticyclonic vorticity (Thomas *et al.* , 2013). Fig 4.4e shows that instabilities increasingly tend toward the symmetric across and immediately below the lower boundary, and this is supported by the changing sign in potential vorticity across the lower boundary, which is indicative of symmetric instability. The time-averaged balanced Richardson number (not shown) is dominated by higher values across the depths of the bottom boundary of the lens and the depth-averaged balanced Richardson number appears to increase with diffusivity across the bottom boundary of the lens (Fig. 4.2d,e). This is further supported by the episodic warming of the LCDW density class waters as the balanced Richardson number increases (Fig. 4.2c).

4.4 Discussion

The EM-APEX float samples a distinct lens of UCDW propagating along the Antarctic continental slope within LCDW at mid-depths, that is consistent with a submesoscale feature. This UCDW feature shares hydrographic characteristics with the offshore UCDW mass initially sampled, implicating it as a potential source, consistent with observations along the continental shelf further south along the WAP (Martinson & McKee, 2012) and the nearby western flanks of Powell Basin (Thompson *et al.* , 2014). While we cannot conclude that the UCDW lens is an eddy since the spatial sampling of the lens eliminates such a diagnosis, it is likely an

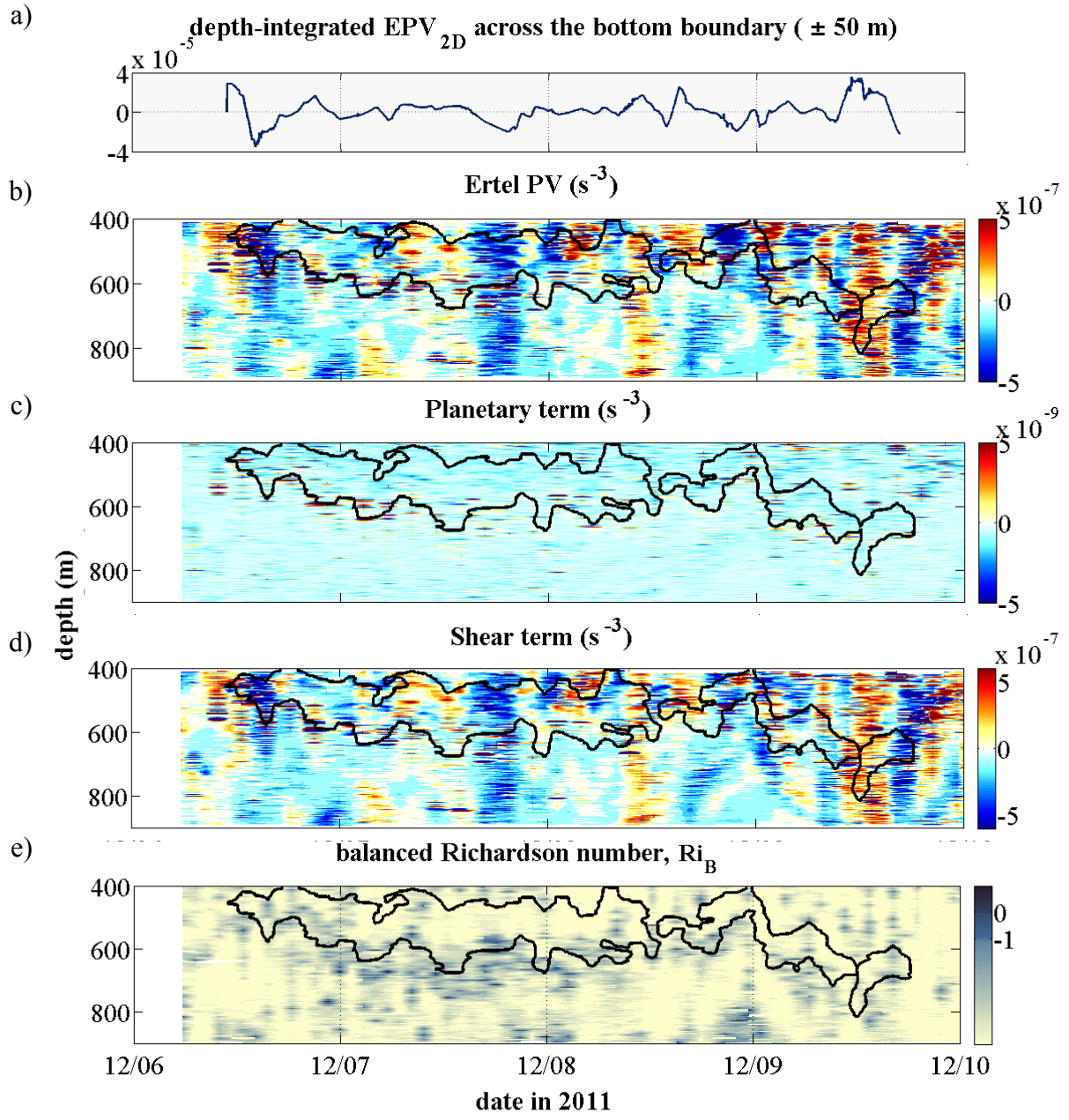

Figure 4.4: a) The two-dimensional case for Ertel's potential vorticity (EPV_{2D}), depth-integrated across the bottom boundary of the UCDW lens (50 m above and below); b) EPV_{2D} and the relative contributions of c) the planetary term and d) the shear term to (EPV_{2D}) and e) the balanced Richardson number in which gravitational instabilities arise where ($Ri_B \leq -1$,); gravitational/symmetric instabilities arise where ($-1 \leq Ri_B \leq 0$) symmetric instabilities arise where $0 \leq Ri_B \leq 1$ (darker blue). UCDW boundaries overlain in black.

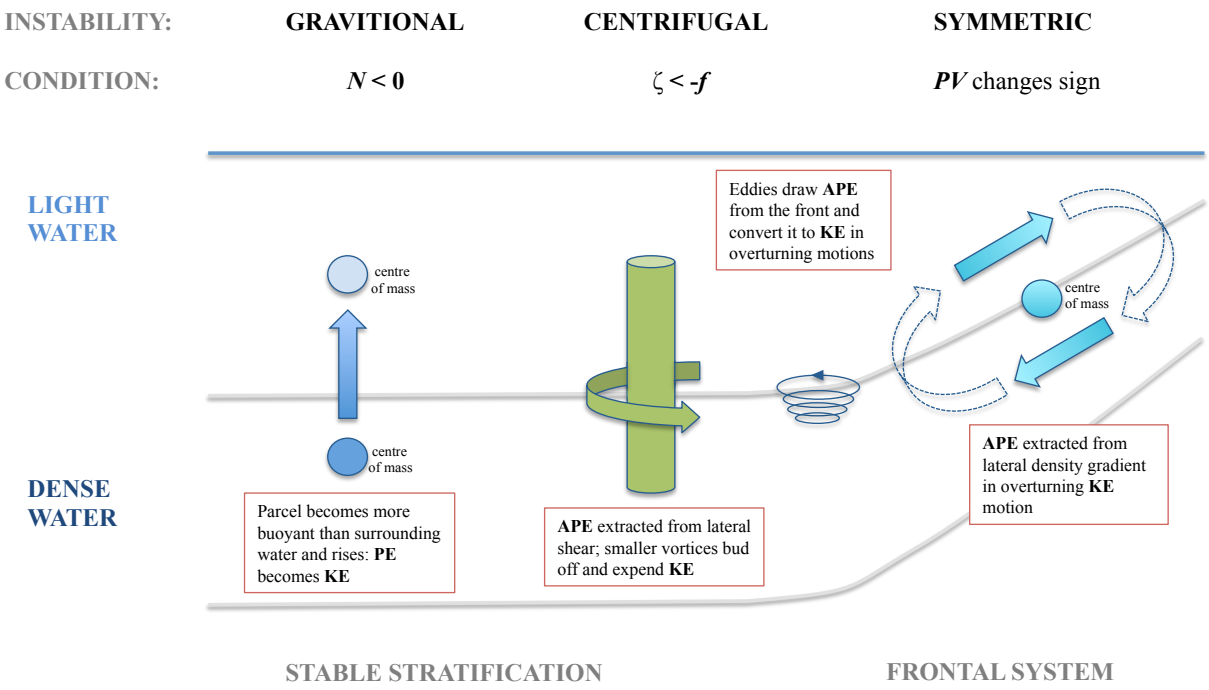

Figure 4.5: a) Schematic to illustrate how baroclinic instabilities can extract available potential energy and convert it to kinetic energy under different conditions, thus driving a forward cascade of energy so that it may dissipate at turbulence length-scales.

eddy and Martinson & McKee (2012) note that UCDW-core eddies are the dominant means of transporting heat onto the continental slope along the WAP. As the float travels along the slope, the entire water column is advected horizontally onto and off the slope by the diurnal tide. Meanwhile, the UCDW lens undergoes vertical vortex-stretching at approximately a semi-diurnal frequency, controlling the overall thickness of the lens. Much of the steep continental slope is favourable for the generation of internal tides (Heywood *et al.* , 2007; Padman *et al.* , 2006) and there is evidence of mixing consistent with the dissipation of M_2 internal tides (Mead Silvester *et al.* , 2014). It is therefore likely that this vortex-stretching arises from the propagation of an internal tide. However, the M_2 tidal frequency and the inertial frequency, f, are very close at this latitude (12.42 hrs and ∼14 hrs respectively). Additionally, given the diurnal and semi-diurnal signals in the surface elevation, there may be some interplay between the vertical semi-diurnal vortex-stretching and any 'squashing' that might arise from the water

column being pushed onto the slope at a by the diurnal tide at a diurnal frequency; exploring a mode 4 signal is, however, beyond the scope of this paper.

Heat is clearly exchanged between UCDW and LCDW (Fig. 4.2c), and the UCDW lens loses 46% of its heat content to the surrounding LCDW between the first and last day it was measured. Thus, as the UCDW lens transforms, it loses both buoyancy and thickness (mass) to the LCDW beneath (Fig. 4.2a,b), so that its centre has sunk by approximately 150 m from its first to its last sample point. Estimated heat fluxes and diffusivity from heat fluxes generally peak in phase with heat gain by LCDW and a deepening of the UCDW lens's bottom boundary, suggesting that the energy for this exchange is bound in a semi-diurnal frequency.

Dissipation, $\varepsilon_{shear-strain}$, is highest within the UCDW lens and diffusivity across the bottom boundary estimated from heat fluxes and shear-strain methods are comparable when peaking (Fig. 4.2d), but diffusivity estimates from heat flux tend to be higher. This difference cannot be entirely attributed to lateral heat fluxes, computed as $\rho C_p < VT >$, where V and T are anomalies relative to the time-mean, since they are at least $O(1)$ smaller than vertical heat fluxes. We note that dissipation estimates from shear-strain methods are less reliable near topography (Kunze *et al.* , 2006), as in this case.

Diffusivity peaks where $S^2 \geq N^2$ (Fig. 4.2d,f), so that where these coincide with heat exchange, shear instability and turbulent mixing are implicated as a mechanism for heat exchange across the bottom boundary. This is further supported by the relatively strong contribution of the shear term to EPV_{2D} and the potential vorticity fluxes near the UCDW lens's lower boundary (Fig. 4.4a). The potential vorticity is higher above the boundary than below it (Fig. 4.4b), creating a gradient across the lower boundary, consistent with a downward mass flux. Positive EPV_{2D} indicates regions where instabilities can develop (Thomas *et al.* , 2013). Since the depth-integrated EPV_{2D} changes sign across the bottom boundary as potential vorticity is driven repeatedly to zero (Fig. 4.4a), we diagnose that the instabilities are associated with symmetric forcing along the bottom boundary. The type of instability can also be inferred from the balanced Richardson number, Ri_B (Fig. 4.5), and we use it to support the evidence from the changing potential vorticity sign only, with the caveat here that the float is pseudo-Lagrangian

and therefore not accurately resolving lateral instabilities. The balanced Richardson number is less than unity everywhere in our data, indicating that instabilities arise from gravitational and/or symmetric forcing (Fig. 4.5). Symmetric instabilities arise where $0 \leq Ri_B \leq 1$; gravitational instabilities where $Ri_B \leq -1$ with a transition where $-1 \leq Ri_B \leq 0$ (Fig. 4.5). Across the upper boundary of the UCDW lens, instabilities are mainly gravitational, consistent with convective heat (buoyancy) loss across the top of the lens (Fig. 4.5). Our results show that instabilities tend towards the symmetric across and immediately below the lower boundary (Fig. 4.4e). Symmetric instability typically mixes waters of oppositely signed potential vorticity - as directly along the lower boundary - to reduce the potential vorticity to zero (Thomas *et al.* , 2013), and is most active in the region beneath the UCDW lens (Fig. 4.4b) where EPV_{2D} is repeatedly driven towards zero (Fig. 4.4a). This occurs as the bottom boundary is deepened at the frequency of the semi-diurnal baroclinic tide, which increases the lateral density gradient along the bottom boundary of the UCDW lens so that the available potential energy may be extracted from the lateral density gradient as kinetic energy in overturning motions (Fig. 4.6). Thus, shear instabilities are driving turbulent mixing across the boundary between these two water masses, leading to the observed heat exchange and transformation at mid-depths over the Antarctic continental slope.

The interaction between the tide and the UCDW lens and the resultant dispersion of heat into LCDW beneath it and over the continental slope highlights the importance of understanding tide-eddy interactions along the Antarctic margins, where UCDW-core eddies are the dominant means of transporting warm UCDW onto the shelf (Martinson & McKee, 2012). The subsequent intrusion of warmed LCDW through depressions in the shelf and into coastal waters where they may reach the undersides of ice shelves is more relevant to observed marine glacier retreat further south along the WAP (Cook *et al.* , 2016). However, our observations show that the vertical deformation of eddies by the baroclinic tide to generate instabilities could be an important mechanism for dispersing heat over the continental slope and at mid-depths, where WAP glacier melt is most sensitive to ocean heat content (Cook *et al.* , 2016).

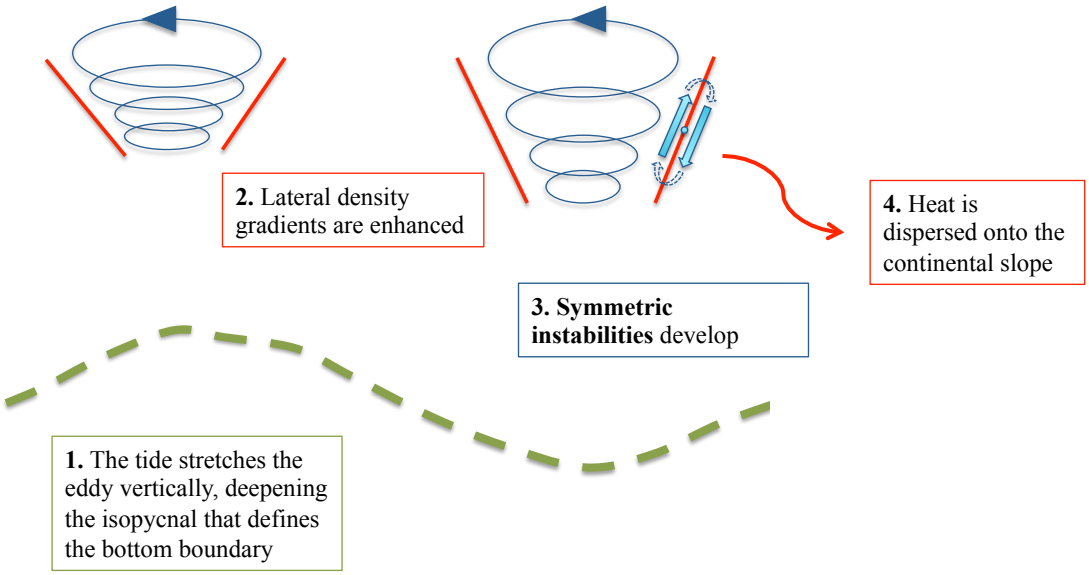

Figure 4.6: a) Schematic representation of instabilities across and around the bottom boundary of an eddy. 1. The tide (green dashed line represents elevation) stretches the eddy in the vertical plane, deepening the isopycnal that defines its bottom boundary; 2. the lateral density gradient along the bottom boundary of the eddy are enhanced; 3. symmetric instabilities develop; 4. overturning motions disperse heat onto the continental slope.

4.5 Summary and Conclusions

An EM-APEX float profiling eastward along the steep Antarctic continental slope from Elephant Island captures a lens of UCDW propagating within LCDW. Heat is exchanged directly between the two as the UCDW lens loses heat, salt, buoyancy and thickness (mass) to the LCDW beneath. Heat fluxes vary at a semi-diurnal frequency of either tidal or inertial origin and peaking diffusivities across the lower boundary of the UCDW lens are associated with shear instability according to the gradient Richardson number. The two-dimensional approximation of Ertel's potential vorticity is both higher within this lens and raised along its lower boundary, with the shear term's contribution explaining much of the elevation in EPV_{2D} along

the bottom boundary of the UCDW lens. The changing sign of the potential vorticity along the UCDW lens' lower boundary is commensurate with symmetric forcing driving potential vorticity towards zero as oppositely signed waters mix. Taken together, this provides evidence of mixing (down a flux gradient, from UCDW to LCDW) across the bottom boundary of the lens, explaining observed heat and mass loss from the UCDW lens. We posit that the baroclinic tide is deforming the lower boundary of the submesoscale lens at a semi-diurnal frequency to enhance lateral density gradients and hence symmetric instabilities; this creates the conditions for overturning and a forward cascade of energy to turbulent length-scales, where it may be dissipated.

The Southern Ocean is recognised for its important role in closing the global ocean heat budget. A vast theoretical and numerical modelling literature exists on the competing contributions to the buoyancy budget, yet only a limited number of observational studies have estimated the role of diapycnal mixing (e.g. Naveira Garabato *et al.* (2007); Mead Silvester *et al.* (2014)). This study further supports the hypothesis that diabatic processes contribute to mid-water watermass transformation. We have presented direct observations of transforming water masses at mid-depths over the Antarctic continental slope as shear instability drives turbulent mixing and heat exchange. In this region, water masses are predominantly transformed following adiabatic upwelling and our observations demonstrate that this also happens at mid-depths, short-circuiting the adiabatic pathway. Quantifying the contribution of such transformations is vital to our understanding of upwelling rates, a critical component in setting the strength of the MOC and the rate of communication of carbon and heat between the ocean and the atmosphere. We have also demonstrated a mechanism by which submesoscale instabilities resulting from the interaction of the baroclinic tide and UCDW-core eddies along the Antarctic margins may contribute to on-slope heat dispersion at mid-depths in regions where the melting of marine glaciers is linked to ocean heat content.

4.6 Acknowledgements

We thank the officers and crew of the RRS *James Clark Ross* and the British Antarctic Survey IT and ETS personnel for their support during the science cruises JR264. We are grateful to Kate Adams for her constructive comments at Challenger Conference 2016. This work was carried out under the auspices of NERCs National Capability project, ACCLAIM. Additionally, JMS was supported by NERC studentship (NE/K500938/1); YDL by NERC Fellowship (NE/H016007/1); JP by NERC grants ORCHESTRA NE/N018095/1 and PycnMix NE/L003325/1; HEP by the Australian Government's National Environmental Science Program and Australian Research Council Grants DP0877098 and CE110001028 and MAMM by OSCAR (NE/I022868/1). Data can be requested from the British Oceanographic Data Centre.

4.7 Supporting Information

This section contains supporting information for Chapter 4. This includes plots that support the analysis and information provided such as those 'not shown' in the original manuscript. The contents are as follows:

1. salinity section, heat and freshwater fluxes including a comparison of fluxes across the top and bottom boundaries as well as the dissipation section from shear-strain calculations;
2. spectrum of temperature at different depths across the lens and T-S diagram of waters inside and outside the lens;
3. tidal ellipse axes for the dominant regional tidal constituents and
4. flagged T-S datapoints from quality-control.

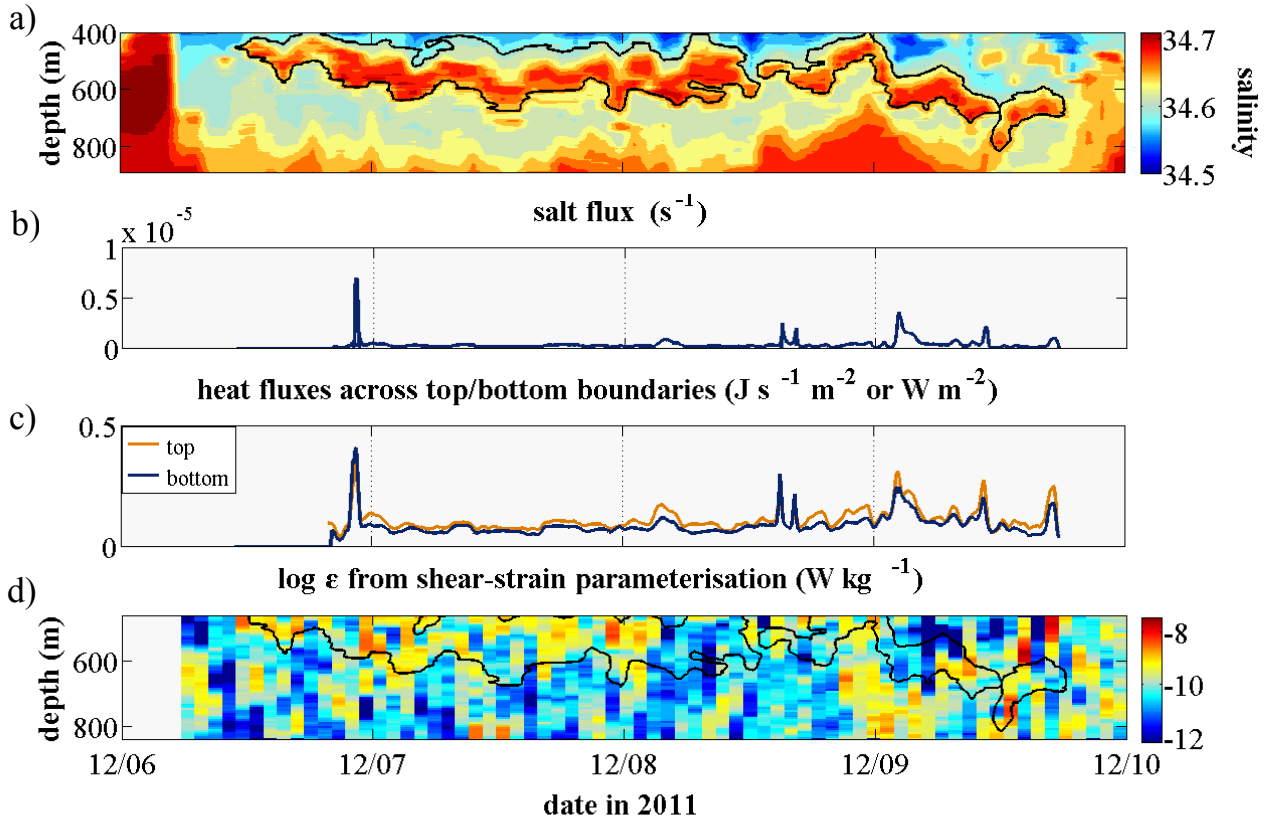

Figure 4.7: a) Salinity of the along-slope section corresponding to the potential temperature plot in Fig. 4.3a. Note that the lens exhibits similar salinity characteristics to the UCDW first sampled throughout the depth profiles and is similar in pattern to the potential temperature section; b - c) freshwater (salt) and heat fluxes across the bottom boundary and c) heat fluxes across the top and bottom boundaries are presented for comparison.Those across the top are neglected in the body of this chapter because the top boundary of the lens is not always captured, much less the surrounding waters. d) plot of the dissipation computed from shear-strain, highlighting elevated dissipation within the first evolution of the lens and the latter part of the second evolution of the lens. Note that because of the fast fourier transform implicit in shear-strain computations, datapoints are lost from the top and bottom of profiles and so dissipation across much of the top of the lens is not resolved.

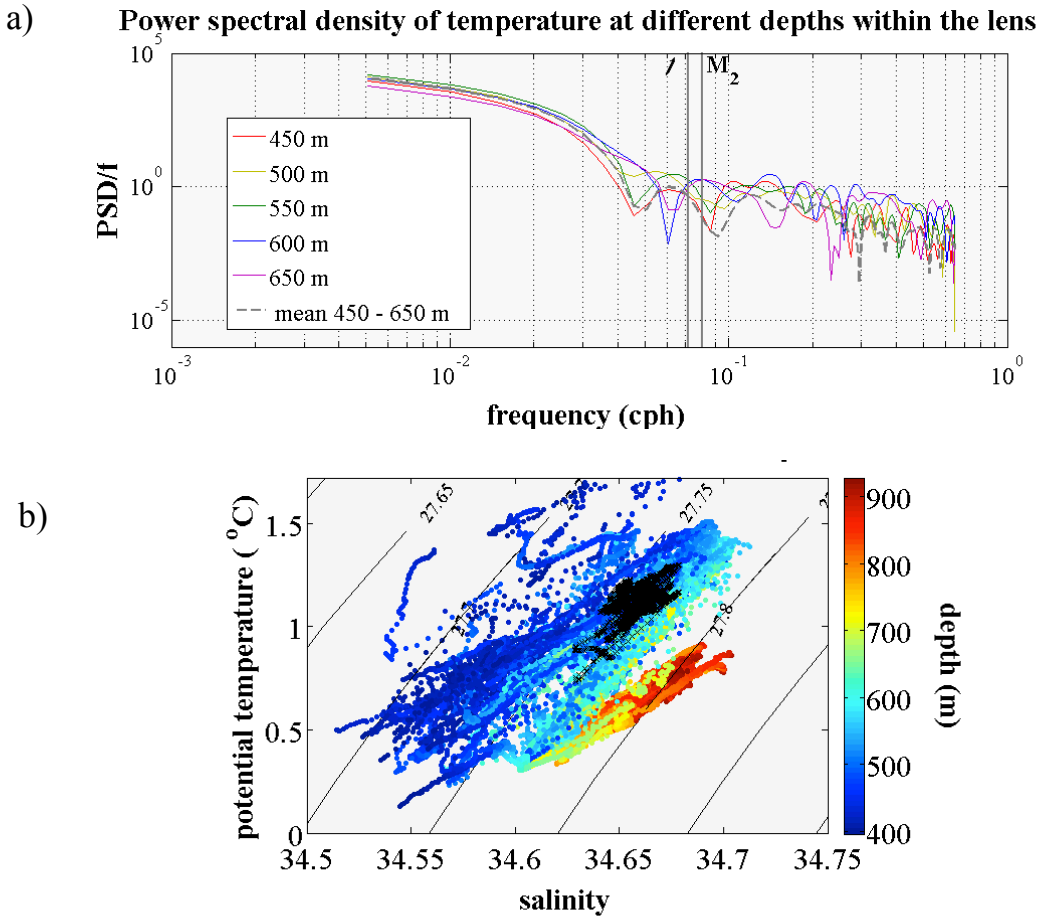

Figure 4.8: a) Power spectral density of the temperature across the depths of the lens (and within the lens). Note that at the depths of the lower boundary of the lens (600-650 m), there is a hump around the the inertial frequency (f) and the M_2 tidal frequency; they are, however close at this latitude and their separation to deduce whether tidal or inertial energy dominates would require a longer timeseries. b) T-S diagram highlighting the clear separation of watermasses within the lens (black crosses) and outside it (coloured by depth).

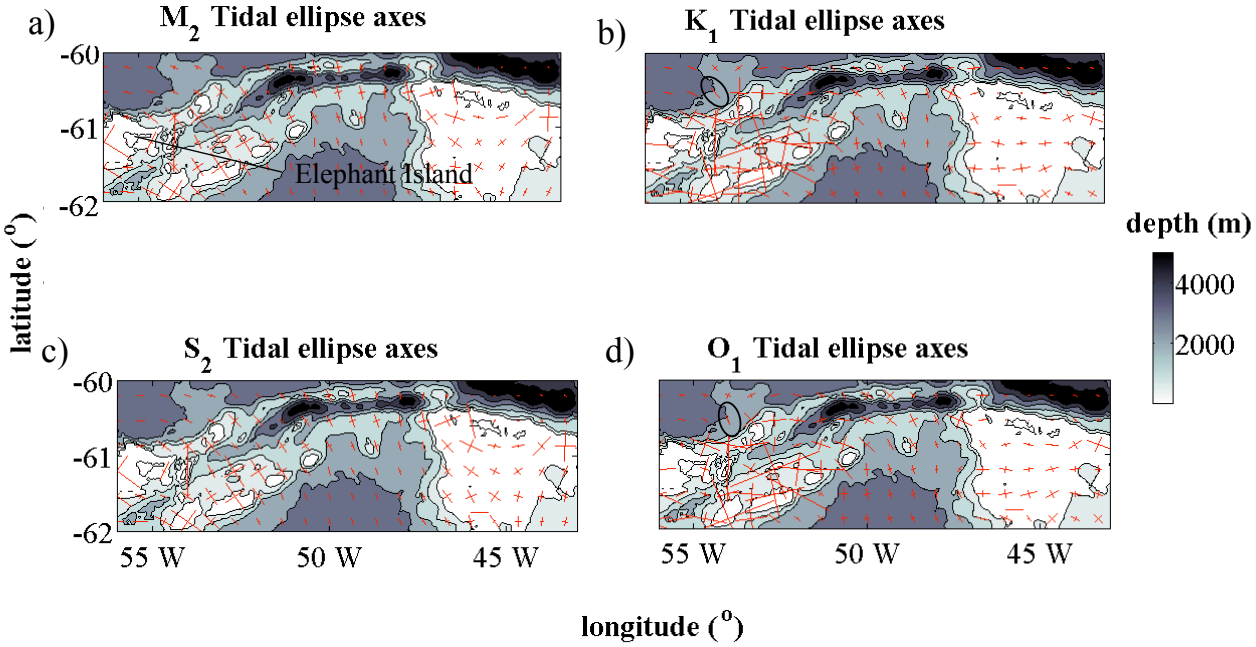

Figure 4.9: a-d) show the tidal ellipse axes for the dominant tidal constituents in the region over the bathymetry. Note that the ellipses for the diurnal tides (subplots b and d) are perpendicular to the continental shelf-break in the region of our EM-APEX float observations (circled in black).

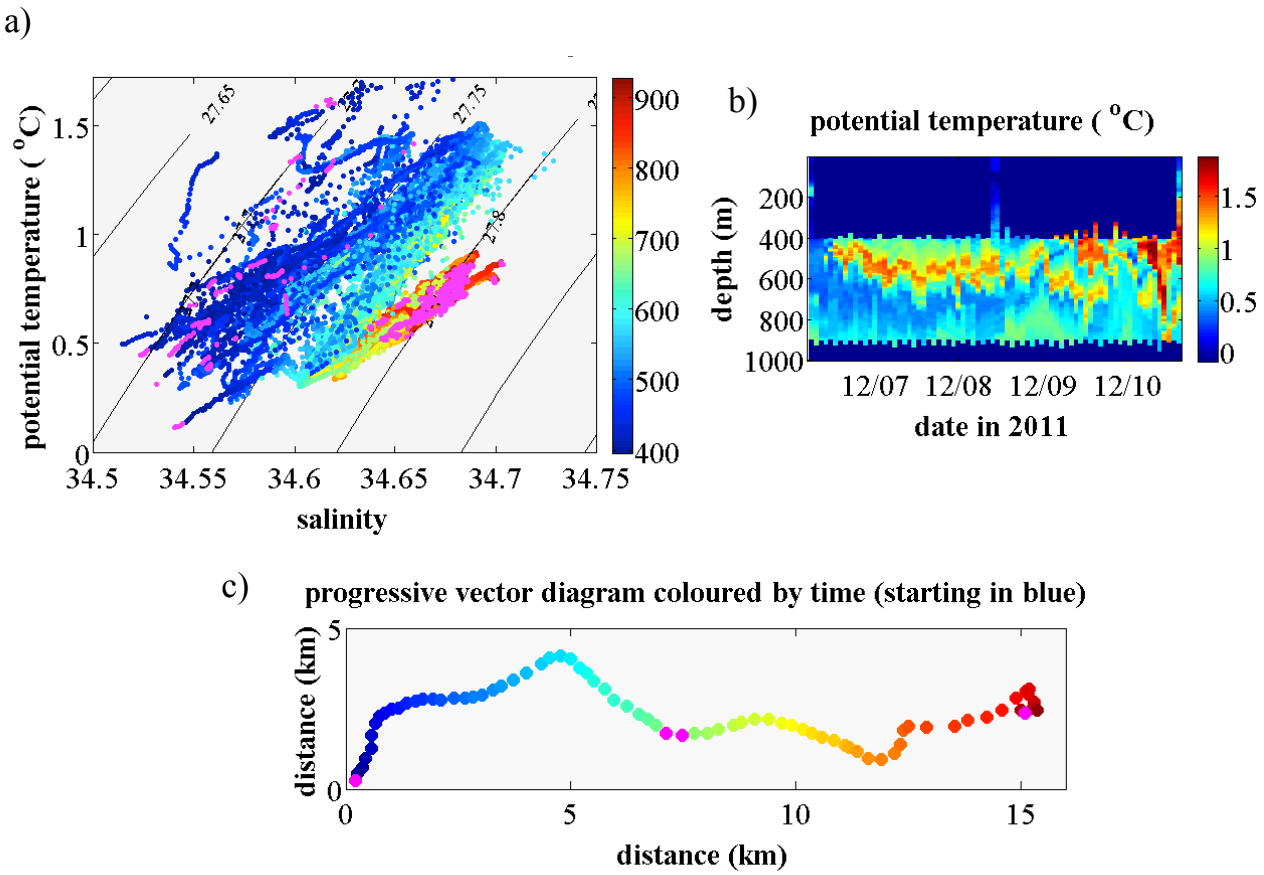

Figure 4.10: a) T-S diagram showing datapoints coloured by depth. Any datapoints removed during quality-control are shown in magenta and are primarily removed from the tops and bottoms of profiles where the EM-APEX float overshoots its target depth and bad pressure points are normally found within these ranges. Additional, any outliers are removed after visually checking individual profiles. b) demonstrates a temperature section from the raw data prior to quality-control, highlighting overshoots at the bottom on descending profiles and at the top on ascending profiles as well as showing individual profiles. c) is the subsurface float trajectory from relative velocities for the same section, with surfacing profiles highlighted in magenta.

Chapter 5

Observations of Dense Weddell Sea Water Export across the South Scotia Ridge

In this chapter, the origins of seasonal dense-water pulses observed at 1040 m on the continental slope north of Elephant Island, further east along the slope and within Hesperides Trough are investigated. Pathways for cold, dense Weddell Sea waters into Hesperides Trough and onto the continental slope here are explored. These processes are linked to dense water (AABW) formation and ventilation. Findings are discussed in the context of Southern Ocean overturning strength, AABW variability, climate feedbacks and a need for sufficient spatial resolution to capture the tidally-induced flows in circulation models.

Abstract

The major source of dense water in the Southern Hemishere is sea-ice production in the Weddell Sea. These waters are exported onto the Antarctic continental slope where they mix with warmer waters, transform and convect downslope to form Antarctic Bottom Water (AABW). AABW, which accounts for 30-40% of total ocean mass, is warming and freshening. Its formation drives the lower overturning cell and its ventilation controls the net CO_2 flux in the Southern Ocean. Weddell waters are separated from south Drake Passage's continental slope by the South Scotia Ridge (SSR) and reach the continental slope either by circumnavigating the SSR to the east or by crossing through topographical gaps. Two EM-APEX floats deployed in 2011 and 2015 near Elephant Island, capture cold, dense waters consistent with Weddell waters crossing the SSR via Hesperides Trough and reaching the continental slope near Elephant Island. These observations occur at similar phases of sea-ice melt to seasonal pulses of cold, dense water captured by a 20-year timeseries from a BPR lander at 1040 m on the continental slope at Elephant Island. The magnitude of these seasonal cold-water pulses on the continental slope and annual sea-ice concentration peaks over an area dominated by Powell Basin from 20-year records are significantly correlated with $r = -0.70, p < 0.05$ and a seasonal lag of 7.5-11 months. This time-lag is consistent with wind-forced transports and tidally-induced flows along the isobaths that connect the slope at Elephant Island and Powell Basin, via Hesperides Trough. Understanding dense water export pathways and their drivers is critical to monitoring AABW variability.

5.1 Introduction

High-latitude processes dominate global dense water formation and the subsequent sinking of watermasses that drives the Meriodional Overturning Circulation (MOC). Antarctic Bottom Water (AABW), the main water mass that occupies the lower cell of the MOC, is thought to account for 30-40% of all ocean mass (Johnson, 2008) and AABW formation is dominated by sea-ice production (Ohshima *et al.* , 2016).

AABW is formed at a few sites along the Antarctic Continental slope where warm, saline Circumpolar Deep Waters (CDW) and cold, Dense Shelf Waters (DSW) interact to form dense convective plumes that can descend the steep continental slope and contribute to deep ocean ventilation (Meredith *et al.* , 2003; Naveira Garabato *et al.* , 2002). A major source is Weddell Sea Deep Water (WSDW), accounting for ∼40% of AABW formation (Meredith *et al.* , 2013). Near the tip of the Antarctic Peninsula, dense waters from the Western Weddell Sea are exported into the South Scotia Sea (Heywood *et al.* , 2004), where warm, salty CDW pushes onto the shelf. In the Weddell Sea, Weddell deep Water overlies WSDW, which in turn overlies Weddell Sea Bottom Water, with denser classes constrained south of the South Scotia Ridge (SSR). Weddell Sea water export pathways are poorly understood and while they can flow around the SSR via the deep Orkney Passage, there is a growing consensus that they are able to cross the SSR through gaps in topography (Heywood *et al.* , 2004; Thompson *et al.* , 2009; Palmer *et al.* , 2012; Naveira Garabato *et al.* , 2002). Naveira Garabato *et al.* (2002) estimate the outflow from the Weddell Sea across the SSR at 19±7 Sv, of which 6±1.5 Sv is bottom water and 10.5±5 Sv is in the LCDW/WDW range. Of the latter, Palmer *et al.* (2012) estimate 7±5 Sv is northward across the SSR, amounting to $1/7^{th}$ of total WSDW export.

The Antarctic Slope Current (ASC) and the Coastal Current (CC) are the main pathways for Weddell Sea waters crossing the SSR through gaps in topography: the former through western Hesperides Trough and the latter via Bransfield Strait (Fig.5.1) (Heywood *et al.* , 2004; Thompson *et al.* , 2009; Flexas *et al.* , 2015b). Additionally, the Weddell Front, a component of the Weddell Gyre, circulates around Powell Basin and a portion exits through Phillip Passage (Thompson *et al.* , 2009), at depths of almost 2000 m. Weddell Sea waters entering Hesperides

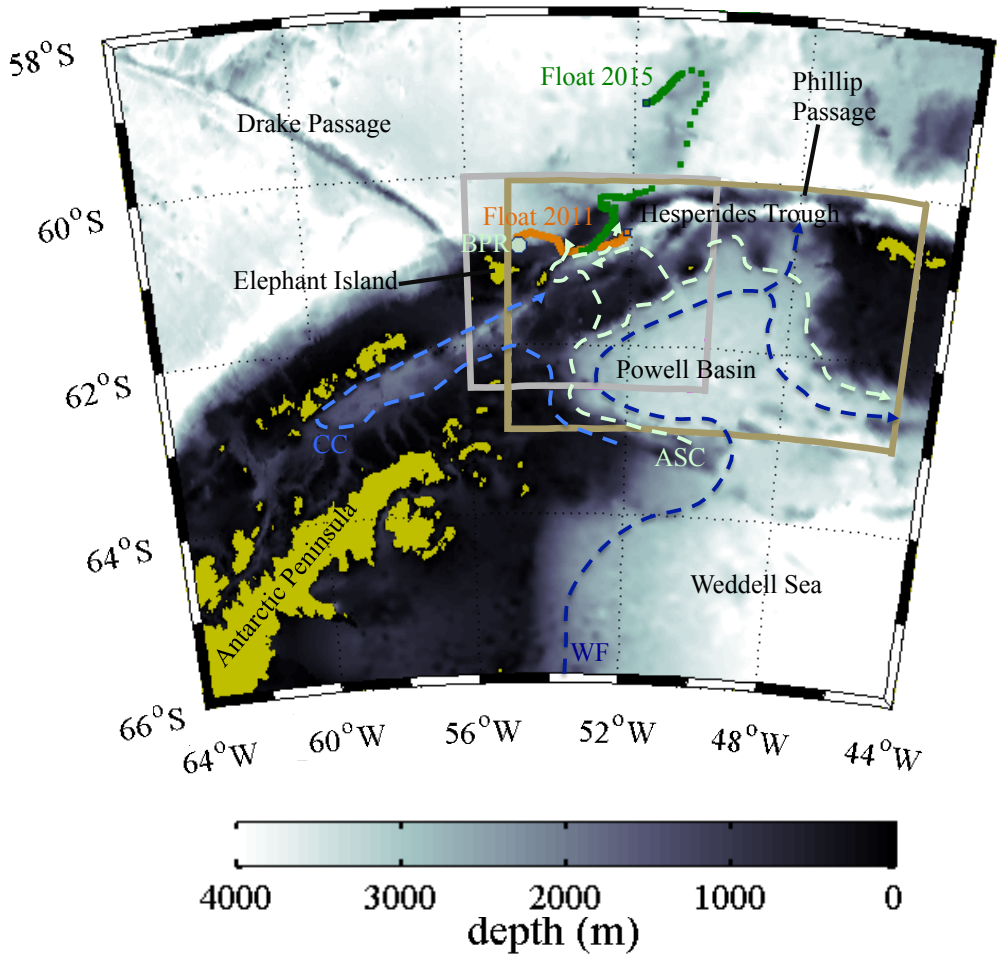

Figure 5.1: Location of EM-APEX float trajectories in 2011 (orange) and 2015 (green), with the end of their trajectories marked by squares. The mint-green dot is the site of BPR-temperature lander at 1040 m over the continental slope north of Elephant Island. The grey-boxed area corresponds to the area in Fig.5.6 and the taupe-boxed area outlines the area over which daily sea-ice concentration is averaged. The pathway commonly given for the Weddell Front (WF), a branch of the Weddell Gyre circulation, is outlined by the dark blue dashed line; the Coastal Current (CC) around Bransfield Strait is given by the light blue dashed line; the Antarctic Slope Front (ASF) is given by the white-dashed line after Heywood *et al.* (2004) with the westernmost exit branch onto the continental slope suggested by Thompson *et al.* (2009).

Trough circulate clockwise around its flanks before they too exit via Phillip Passage through the northern opening, so that although there is no direct connectivity between waters entering and leaving, those waters arriving onto the continental slope are significantly cooler and denser (Palmer *et al.* , 2012).

Along the northern slope of the SSR, important watermass transformations contribute to the upper and lower limbs of the Southern Ocean MOC. Here, waters upwell and undergo transformation at the surface near the cold continent, some of which lose buoyancy and sink to form AABW. Near Elephant Island, the continental slope drops steeply to ∼3000 m.

Meredith *et al.* (2003) linked seasonal dense water pulses on the continental slope at Elephant Island to local dense water production associated with seasonal changes in sea-ice. While Meredith *et al.* (2003) rejected the ingression of Weddell Sea waters around the SSR as an explanation for seasonal cold-water pulses, more recent studies have shown that the ASF, CC and Weddell Front likely form pathways onto the slope near these measurements at Elephant Island (Fig.5.1). These studies use a combination of ADCP current velocity observations (Naveira Garabato *et al.* , 2002), surface drifter pathways (Thompson *et al.* , 2009), current-meter moorings and hydrographic sections (von Gyldenfeldt *et al.* , 2002; Heywood *et al.* , 2004) and general circulation models (Schodlok *et al.* , 2002). Flexas *et al.* (2015b) note that tides contribute to the maintaince and steering of the ASC. More recent studies by Meijers *et al.* (2016) and Youngs *et al.* (2015) link seasonal variability in the properties of the slope current at Elephant Island to wind stress curl over the Weddell Gyre, an intensification of the Weddell Front and hence the ASC so that Weddell Sea waters are forced through deep sills across the SSR.

AABW and exported Weddell Sea waters have been freshening and warming over recent decades (Jullion *et al.* , 2013; Schmidtko *et al.* , 2014), affecting AABW subduction (Purkey & Johnson, 2010), which has implications for overturning strength as well as the efficacy of CO_2 drawdown. However, at present, our understanding of export pathways, modification *en route* and sites of shelf-sourced AABW formation limits our ability to monitor the variability of AABW and exported Weddell Sea waters.

Identifying shorter export pathways (i.e across the SSR) is important because waters transform *en route* so that the dense, cold properties of Weddell Sea waters are diluted. This is a region where high turbulent kinetic energy dissipation and therefore modification is expected (e.g Padman *et al.* (2006)). Monitoring how waters that feed AABW are modified along their export pathways and their variability is essential to understanding changes in AABW, but is presently constrained by a poor understanding of export pathways and their drivers. The aim of this paper is to investigate the source of cold, dense waters captured by EM-APEX floats near Elephant Island and in western Hesperides Trough as well as seasonal dense-water pulses recorded over 20 years by a Bottom Pressure Recorder on the continental slope at

Elephant Island. As such, the objectives are (1) to explore the relationship between seasonal cold-water pulses at Elephant Island and regional sea-ice concentration; (2) to explore possible sources of our dense-water observations and BPR pulses (i.e locally-produced dense shelf waters or dense waters exported from elsewhere) and (3) to explore possible export pathways from time-lags between sea-ice production (i.e dense water formation), known ocean flows, and our observations.

Our observations consist of three sections taken from two autonomously profiling EM-APEX float timeseries that capture cold, dense waters in western Hesperides Trough and on the continental slope north of the SSR. The data and models used are described in Section 5.2 and results are presented in Section 5.3. Our findings are discussed in Section 5.4 and summarised and concluded in Section 5.5.

5.2 Measurements, methods and rationale

This study uses direct observations from two autonomously profiling EM-APEX floats, which capture cold, dense water in Hesperides Trough and on the continental slope in south Drake Passage. The timing of these events are compared to a 20-year record of absolute temperature from a Bottom Pressure Recorder (BPR) at a depth of 1040 m on the continental slope at Elephant Island, and this timeseries is compared to a corresponding 20-year record of Antarctic sea-ice concentration from composite satellite data over the region. Since there is a time-lag of 9-10 months between sea-ice production over the region and dense-water pulses and we have observations of cold, dense water crossing the SSR and steered along isobaths, we use modelled tidally rectified velocities from TMD (Padman & Erofeeva, 2014) to explore transports between Powell Basin in the Weddell Sea and the continental slope at Elephant Island. The datasets used are introduced in detail in the following paragraphs.

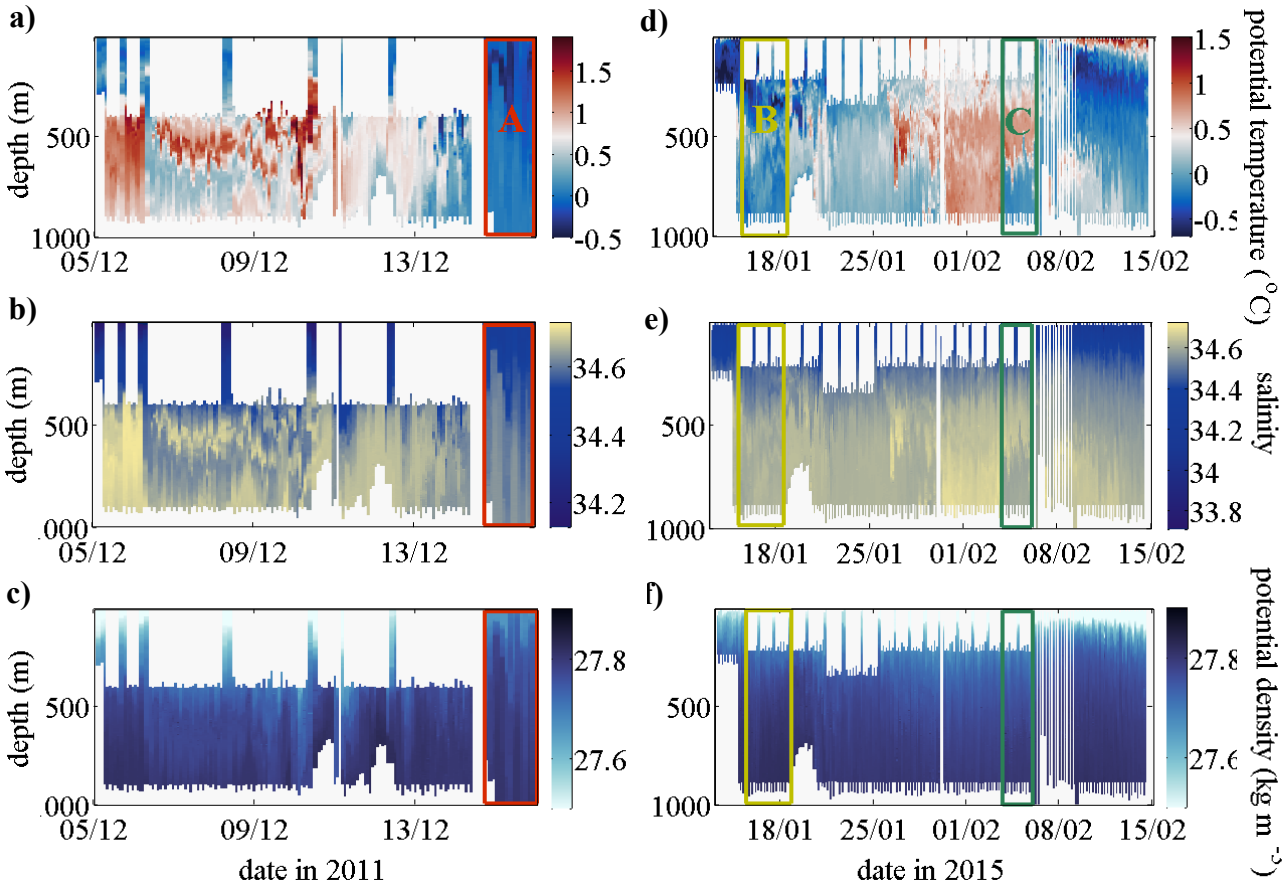

Figure 5.2: a) potential temperature, b) salinity and c) potential density of the 2011 deployment of the EM-APEX float; d) potential temperature, e) salinity and f) potential temperature of the 2015 EM-APEX float deployment. Regions A, B and C, which correspond to T-S diagrams A, B and C in (Fig.5.4) are highlighted; their colour signatures are consistent throughout the figures presented in this paper.

5.2.1 Dense water observations

An autonomously profiling EM-APEX float (no. 4980a) was deployed from *RRS* James Clark Ross on cruise R264 near Elephant Island on 5 December 2011 and recovered on 17 December 2011. The float profiled continuously between 400m and 900m along the continental slope near Elephant Island and within Hesperides Trough, a deep trench crossing the ridge that separates Drake Passage and the Weddell Sea (Fig.5.1). The float was redeployed (as no. 4980b) on 11th January in Hesperides Trough at the westernmost end, where it profiled to 900 m before crossing the northern ridge and drifting eastwards along the continental slope until its battery depleted on the 2nd February 2015 (Fig.5.1). The EM-APEX made *in situ* measurements of

conductivity (± 2 x 10^{-3}) (Fig.5.2b and d), temperature (± 2 x 10^{-3} °C) (Fig.5.2a and c) and pressure (± 2 dbar) which were recorded by a pumped SeaBird Electronics CTD in 2.2 m vertical bins. All data were visually checked for surface pressure consistency and bad pressure points (mainly near the top and bottom of profiles) were removed. Outlying temperature and salinity values were flagged using T-S diagrams and visually evaluated against density profiles; in rare instances of bad data, points were removed and interpolated over (see supporting Fig 5.9 for flagged data and further explanation). We present sections in which dense water was observed, two of which are in Hesperides Trough, captured in separate years, and one of which is on the continental slope in South Drake Passage (Fig.5.2, boxed areas A,B and C and Fig.5.4).

5.2.2 BPR temperature record and sea-ice concentrations

BPR temperature record

The high resolution (1992-2012) absolute temperature record comes from the Drake Passage South BPR, which sits on a lander at 1040 m on the continental slope immediately north of Elephant Island (Fig.5.1), and records temperature and pressure every 15 minutes. Data are retrieved and the landers are serviced annually or biennially as part of NOC Liverpool's Antarctic Circumpolar Levels by Altimetry and Island Measurements (ACCLAIM) programme. Meredith *et al.* (2003) calibrated temperature data from 1992-1999 and 2000-2001 deployments and found accuracy to be within 0.01^{o}C, sufficiently accurate to reliably capture seasonal cold water pulses.

Sea-ice concentrations

Daily averaged sea-ice concentrations 1992-2015 are from Nimbus-7 SMMR and DMSP SSM/I-SSMIS Passive Microwave Data from the National Snow and Ice Data Center. Regions are then divided into the taupe-boxed area in (Fig.5.1), a larger area, Hesperides Trough only, Powell Basin only and the shelf immediately north of Elephant Island. Daily sea-ice concentrations are

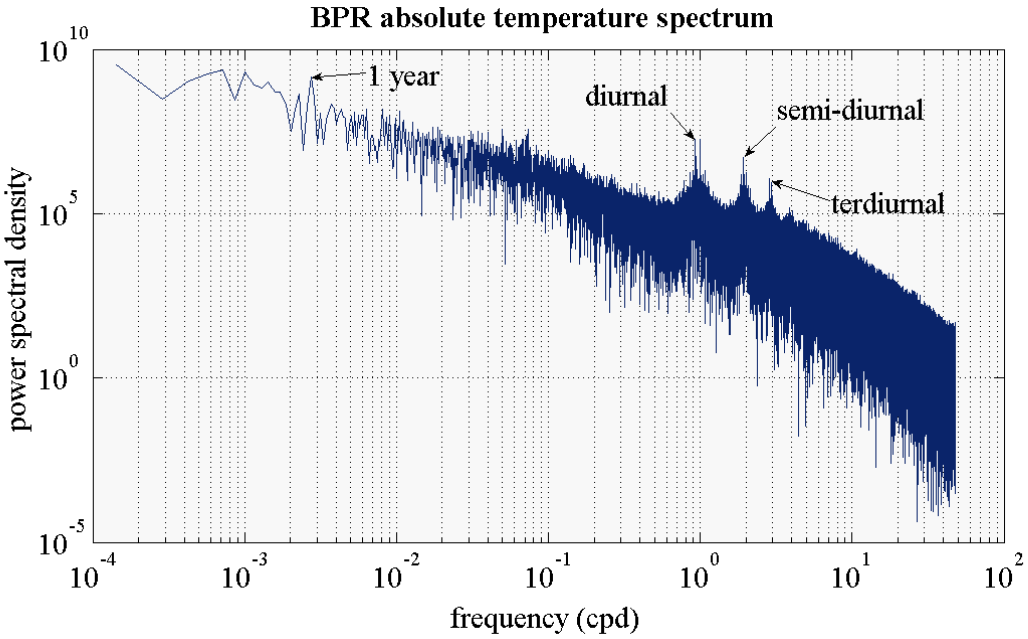

Figure 5.3: a) power density spectrum of the absolute temperature from the BPR recorder at Elephant island from 1992-2012. Note the annual peak in the spectrum, as well as diurnal, semi-duirnal and terdiurnal frequencies.

then averaged over the entire area for each region. The different areas are shown in supporting Fig.5.7a and d.

Correlations

We use a simple method for testing correlations between noisy, high-resolution datasets which correlates the higher-amplitude signals at the dominant frequency according to spectral periodicity. This is similar in concept to the first intrinsic mode function of a Hilbert-Huang transformation (Huang, 2014). Since the signals of both sea-ice concentration and BPR water temperature are dominated by annual spectral periodicity (see Meredith *et al.* (2003) and Fig.5.3), the peaks and troughs in sea-ice concentration and BPR temperature respectively (Fig.5.5 a and b) are identified according to the specification that (1) there should be 20 in the 20-year timeseries and (2) they should not be closer than 300 days apart. The magnitude of seasonal peaks in sea-ice concentration and the magnitude of seasonal troughs in BPR water

temperature for each year are then correlated, using a Pearson's correlation. This is repeated using a lag of one season so that the magnitude of the seasonal sea-ice concentration peak of, e.g 1995, is compared the magnitude of the seasonal trough in BPR temperature in 1996. The resulting correlation is only performed on overlapping years so that the BPR temperature for 1992 and the sea-ice concentration in 2011 are not taken into consideration. When performing an optimally-lagged correlation on the entire dataset, lags do not exceed one year. The pattern of seasonal sea-ice concentration is much the same for all regions investigated (supporting Fig.5.7c) and we present the results for the taupe-boxed area in Fig.5.1, which exhibits the strongest correlation. It is noted that there is a similarly strong correlation over the largest area and Powell Basin only (which dominates the taupe-boxed region), followed by Hesperides Trough only and, lastly, the Elephant Island shelf area (supporting Fig.5.7b). We use this correlation only to support observations in inferring likely source regions and export pathways from the time-lag between peaking sea-ice concentration (marking the end of production) and the BPR dense-water pulses; we do not suggest the likely location of dense-water production from the strength of correlation alone in any region.

5.2.3 Tidally-induced flow

The tidally induced flow is computed using Tidal Model Driver (TMD) (Padman *et al.* , 2002). This is a Matlab package for accessing the harmonic constituents of high latitude barotropic tide models and is run here with the1/30° x 1/60° (2 km) Antarctic Peninsula model (Model_AntPen) (76°S$-$58°S, and 240°$E-330°E$), from the middle of the Weddell Sea to west of Pine Island Bay. Computations are based on linearised shallow-water equations forced at open boundaries by tidal height from the circumpolar forward model CATS02.01 and astronomical forcing, and the model is particularly valuable for exploring tidal flows in narrow passages around the Antarctic Peninsula and islands near its tip, and is used for these purposes here. TMD for the Antarctic Peninsula can be downloaded from
https://mail.esr.org/polar_tide_models/Model_AntPen0401.html.

For our purposes, the depth- and time-averaged tidal residual velocities are extracted for each

of the M_2, S_2, O_1 and K_1 harmonic constituents, and linearly added together. The magnitude of the tidal excursion, for each harmonic constituent, is computed from the semi-major and semi-minor tidal ellipse model output (which are accurate to 0.05 cm s^{-1}) and, from this, the velocities are computed after Polton (2015) as:

$$U = \alpha L_T (f \frac{\Delta h}{h}) \tag{5.1}$$

where L_B is the length scale of the bathymetry, L_T is the point-wise tidal excursion length scale and α, the frictional coefficient, is 0.15 (Robinson, 1981) where $L_T \leq L_B$ and 0 where $L_T \geq L_B$ (the velocity of the induced current does not differ by more that $O(1)$ for a frictional coefficient between 0.15 and 0.75). Finally, $\frac{\Delta h}{h}$ is the maximum fractional change in water depth within a single tidal period. The latter can also be described, and is computed, as the ratio of the tidal excursion in the upslope direction to the bathymetric length scale, L_B, to give the maximum fractional change in water depth (Polton, 2015).

For a full description of how net currents are induced from oscillating flow over bathymetry from the vortex stretching of the Coriolis effect and friction, see Huthnance (1973); Polton (2015). The depth-averaged velocities of the tidally rectified flow presented here provide only a qualitative, instantaneous description of the persistent, baroclinic current speeds along isobaths. Nevertheless, this does give a first-order estimate for tidally induced currents that can be used to identify flow pathways across the SSR since flow is anticlockwise around bumps and clockwise around troughs in the southern hemisphere. We use the modelled magnitude of the tidally induced flow to approximate the flow along the 1000m -1500m and the 750m-900m isobath in a back-of the envelope fashion: taking the contour equidistant from the boundary contours (i.e 1250 m and 825 m respectively), we compute the point-wise velocity between points X and BPR and integrate along the isobath to find the time taken.

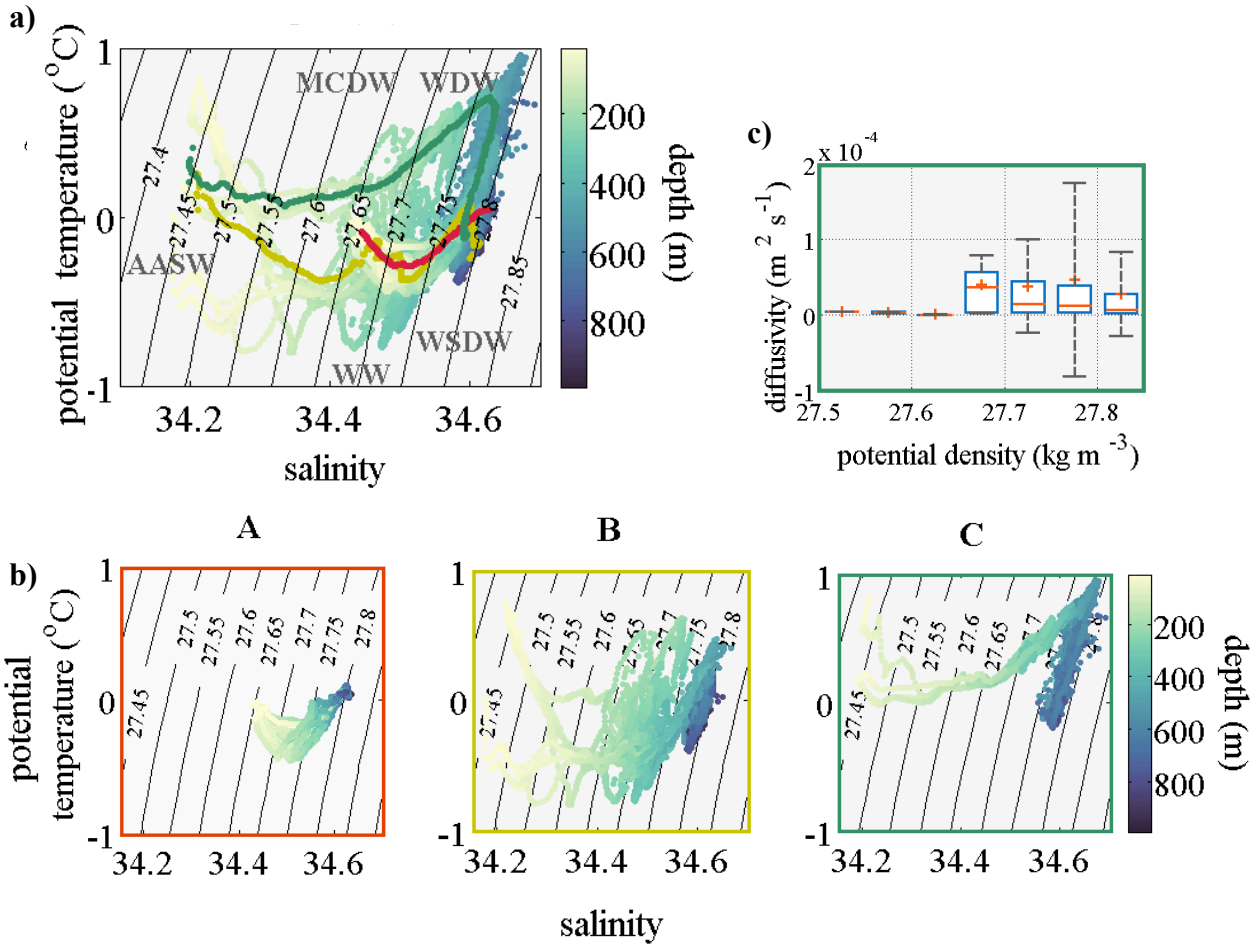

Figure 5.4: a) Potential temperature-salinity plot and relevant water masses for all sections A-C coloured by depth, with the depth-mean for each section overlain in the colour corresponding to the border of T-S diagrams A-C in panel b) and c) a box -and-whisker plot of the isopycnic diffusivity for section C, binned every 0.5 kg m^{-3}, with the box limits denoting interquartile range, the whiskers are the standard deviation, the orange line the median and the orange cross is the bin-average.

5.2.4 Diffusivity estimate

Dissipation is estimated by applying shear-strain parameterisation methods after Meyer *et al.* (2014, 2015) to the EM-APEX float parameters. The resulting diffusivity is used to compute the diffusivity via Osborn's relation (Osborn, 1980), $k_{shear-strain} = \Gamma \frac{\varepsilon}{N^2}$, where ε is the dissipation rate and Γ, the mixing efficiency, is fixed at 0.2. Plots of N^2 and ε are shown in supporting Figs.5.8b-c. Note that during the fast fourier transforms implicit in the shear-strain parameterisation calculation, a number of datapoints are lost from the top and bottom of profiles.

5.3 Results

The Temperature-Salinity (T-S) diagrams from sections A, B and C are given in (Fig.5.4 a) and conform to the T-S watermass map in the Southern Ocean, characterised by a hook-shaped formation associated with WDW (Heywood *et al.* , 2004; Thompson *et al.* , 2009) (Fig.5.4 a). Section A, from 2011, depicts cold, fresh waters at mid-depths and a clear increase in salinity with depth; section B from 2015 shows a similar region of cold (< 0.5), fresh waters between 400 m and 700 m, with a slightly warmer and more haline signal below 700 m, cooling sharply along the 27.8 kg m^{-3} isopycnal; section C shows CDW overlying WDW through WSDW, with a sharp transition associated with relatively elevated diffusivities (Fig.5.4 c), although errors are high. Generally, waters hold the characteristics of Antarctic surface waters above 200 m (limited profiles in B and C) and Weddell Sea waters below 700 m. Notably section B demonstrates some of the characteristics associated with the ASC at mid-depths (Heywood *et al.* , 2004).

Sea-ice concentration and BPR temperature both display annual, seasonal signals (Fig.5.5 a and b), with spectral energy density peaking annually (Fig.5.3. Cold, dense-water pulses here are also associated with freshening (Meijers *et al.* , 2016). Harmonic analysis also confirms the dominant annual signal in the sea-ice concentration and BPR-temperature timeseries (supporting Fig.5.8). While the phasing of cold-water pulses - and our EM-APEX float dense water observations - consistently occur as sea-ice concentration diminishes (melts) during the same season (Fig.5.6), the magnitude of the annual peak in sea-ice concentration over the taupe-boxed area in (Fig.5.1) and that of the seasonally-lagged trough in BPR water temperature are significantly and negatively correlated with $r = -0.70$ (insignificant for current season), both with $p < 0.05$. The average seasonal phase lag is 262.94 days with a standard deviation of 54.02 days (7.5-11 months). Initially, five different areas of sea-ice concentration were correlated with BPR temperature (the wider area of south Drake Passage and Powell Basin, the taupe-boxed region in Fig.5.1, Hesperides Trough only, Powell Basin only and the shelf immediately north of Elephant Island only, see also supporting Fig.5.7). The taupe-boxed region displays the highest correlation when optimally lagged, while the local on-slope region displays the weakest corre-

lation. However, the annual phasing of growth and decay in sea-ice concentration is similar for all areas.

The magnitude of the depth-averaged tidally-induced flow around bathymetry is shown in Fig.5.6, together with the flow direction along the isobath between the 1000 m and the 1500 m contours, which run continuously around the Antarctic Peninsula, connecting Powell Basin and south Drake Passage. In the southern hemisphere, the tidally induced current flows anti-clockwise around bumps and clockwise around troughs (the direction of flow around Hesperides Trough is known to be clockwise (Palmer *et al.* , 2012)). The magnitude of the current along the 1250 m contour gives a first-order approximation of the tidally-induced flow along the connecting isobath between the 1000 m and 1500 m, between points X and point BPR, where the BPR recorder lies on the isobath at 1040 m. The flow is considerable at several orders of magnitude greater than that around the rest of the peninsula, where it continues. The tidally-induced flow takes ∼262 days (9-10 months) to complete the journey in the direction of the yellow arrows. This is in good agreement with the seasonal lag between sea-ice concentration and cold-water pulse magnitudes. Where tidally-induced currents are persistent and high, they may be sufficient to act as biogechemical pathways (Polton, 2015); this is the case over much of the route along the 1000 m - 1500 m isobath and the 700 m - 900 m isobath.

5.4 Discussion and summary

Weddell Sea Deep Waters are the main supplier of AABW globally, and a portion ($\sim 1/7^{th}$) is exported across the SSR (Palmer *et al.* , 2012) onto the continental slope where it can form AABW. It is thought that Weddell Sea Waters crossing the SSR are predominantly transported from Powell Basin into Hesperides Trough via the CC and the ASC before exiting northwards via Phillip Passage. Heywood *et al.* (2004); Thompson *et al.* (2009) hypothesise that the ASC carries dense Weddell Sea waters across the SSR further west near Elephant Island, but the fate of the ASC beyond Hesperides Trough is unclear: Heywood *et al.* (2004) suggest the watermass loses cohesion through mixing while Meijers *et al.* (2016) identify a cool, fresh

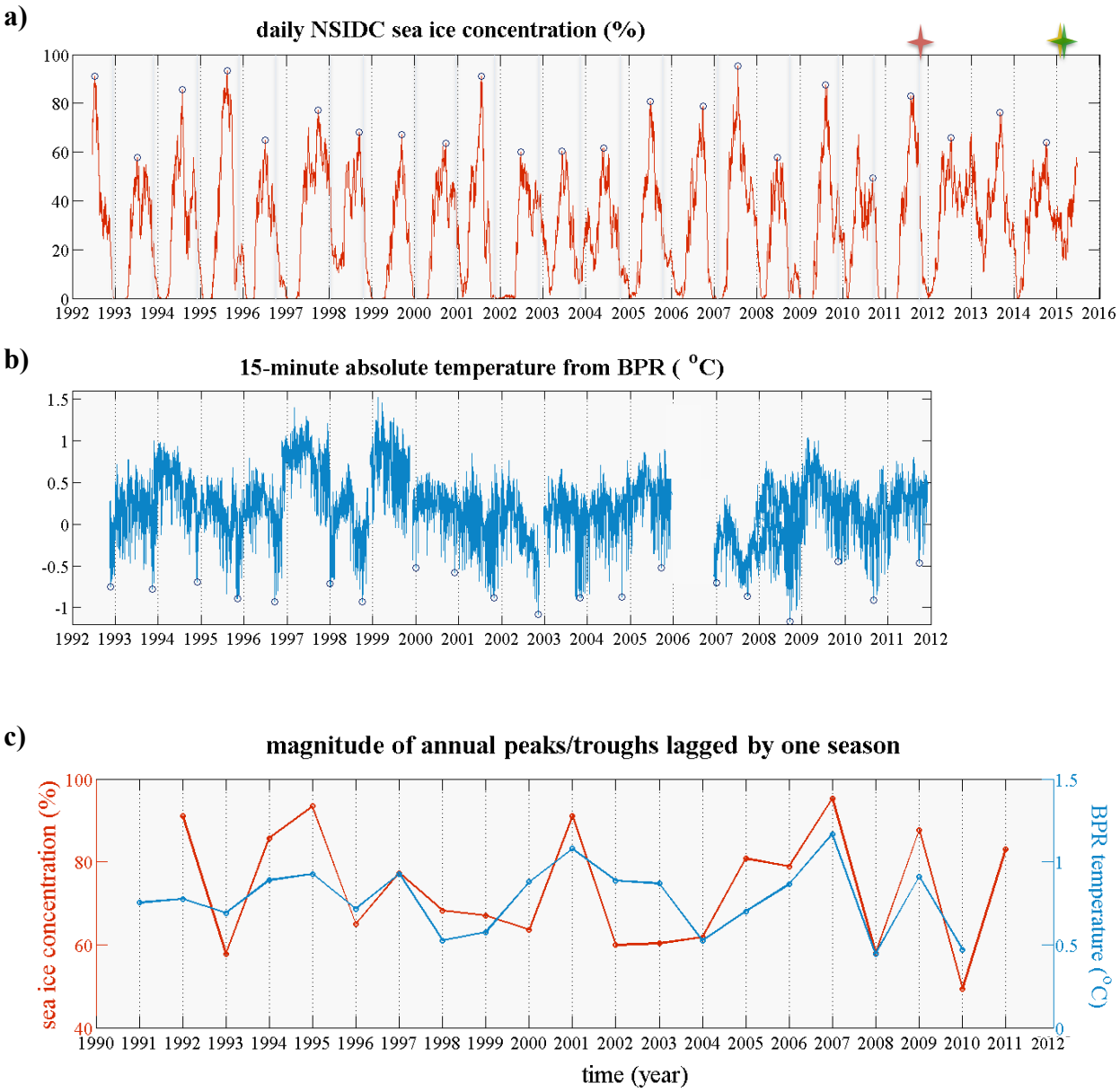

Figure 5.5: a) sea-ice concentration in the taupe-boxed region in Fig.5.1 and b) BPR-temperature. The circles mark the annual peaks and troughs respectively, with grey vertical lines in panel a) aligning with the cold-water pulse spikes in panel b). Stars show the timing of measurements A-C, chronologically and in consistent colours. c) is a plot of the magnitude of seasonal sea-ice concentration peaks and BPR-temperature troughs for each year, lagged by one season (significant correlation $r = 0.70$).

westward-flowing slope current along the continental slope at Elephant Island and hypothesise that it is an extension of the ASC in which Weddell Sea waters remain cohesive. von Gyldenfeldt *et al.* (2002) and Meijers *et al.* (2016) posit that gaps in topography at depths greater than 1000 m along the southern SSR west of Phillip Passage may form additional gateways for dense Weddell Sea Waters.

We observe T-S watermass properties consistent with dense Weddell Sea waters in western Hesperides Trough (Fig.5.4 b, sites A,B) and on the Antarctic continental slope (Fig.5.4 b, site C) at 52 -53^o W, close to Elephant Island and further west than Phillip Passage. We also confirm the continued trend in seasonal cold, dense water pulses in the temperature record at 1040 m on the continental slope at Elephant Island (Fig. 5.6, site BPR) identified by Meredith *et al.* (2003) by extending the 10-year timeseries by over a decade (Fig. 5.3). From this, we find a strong and significant, seasonally-lagged correlation of $r = -0.70, p < 0.05$ between the magnitude of cold water pulses and that of (previous season) sea-ice concentration. Not all our observations A-C are consistent with dense Weddell Sea Water export pathways proposed in the literature and dense waters observed at A,B and C occur at similar phase lags from peak sea-ice concentration to BPR cold water pulses. Since (1) there is a seasonal lag in the correlation between cold water pulses and previous-season sea-ice concentration peaks; (2) there is no significant correlation with current-season sea-ice concentration; (3) the best correlation comes from a relatively large area that includes Powell Basin, Hesperides Trough and the continental slope (Fig.5.1) and (4) there is no significant correlation with same-season local shelf sea-ice concentration, we propose that the dense water is exported from elsewhere onto the slope at Elephant Island. The shelf near Elephant Island forms part of an envelope at the tip of the Antarctic Peninsula identified by Ohshima *et al.* (2016) as a region of $\sim$ 2-3 m annual sea-ice production, creating the conditions for DSW formation, but we may discount this as a source because of the seasonal lag and the low capacity for storage over such a long period on the narrow shelf near Elephant Island. Our 7.5-11 month time-lag between sea-ice concentration peak (marking the end of production) and the cold-water pulses at Elephant Island is in agreement with the 6-13 month time-lag that Meijers *et al.* (2016) find between an intensification of wind-stress curl over the Weddell Gyre and slope current densities at Elephant

Island; they hypothesise that this is the result of the barotropic acceleration of the boundary current and the subsequent ingression of Weddell Sea waters across the SSR via the ASC (export around the SSR via Orkney Passage would take too long). From this explanation, our observations might represent a braided continuation of the ASC within and beyond Western Hesperides Trough.

Since our EM-APEX float observations of cold, dense water (Fig. 5.6) do not neatly align with the ASC but track isobaths that connect Powell Basin to the continental slope in south Drake Passage, we further investigate along-isobath flows by exploring the tidally-induced current along those isobaths. Our back-of-the-envelope calculation of the time taken from site X (Fig.5.6) to the BPR lander along the continuous isobath 1000 m - 1500 m ($\sim$262 days) agrees remarkably well with the observed seasonal lag between sea-ice concentration peaking and dense-water pulses ($\sim$282 days). If the tidally-induced currents transport Weddell Sea waters from Powell Basin along the isobath where the BPR lies at 1040 m, then the cool, fresh pulses observed here would not necessarily be associated with the downslope convection hypothesised by Meredith *et al.* (2003); this is supported by the fact that these seasonal pulses are not recorded by the lander below at 2000 m (Meijers *et al.* , 2016), which implies an along-isobath delivery of cold, dense waters at 1040 m.

However, higher isobaths (750 m - 900 m) also connect the two sites at depths consistent with our EM-APEX observations of cold, dense waters, connecting at the southernmost tip of Clarence Island or circulating around Bransfield Strait before crossing immediately north of Clarence Island and onto the shelf north of Elephant Island (Fig.5.6). From the tidally-induced current, we estimate that the shorter route that connects south of Clarence Island would take $\sim$190 days, while the slower tidally-induced flow around Bransfield Strait adds 5.8 years onto the journey. A number of 15-m surface drifters which are topographically steered replicate the route via the connection south of Clarence Island in Thompson *et al.* (2009)'s study, supporting this shorter pathway. While significantly shorter than the tidally-induced flow along deeper isobaths at around 6 months, waters reaching the shelf north of Elephant Island via this route may then form dense water upon interaction with salty CDW, spread and descend, a process which takes a few of months (Meredith *et al.* , 2003). This brings the journey time

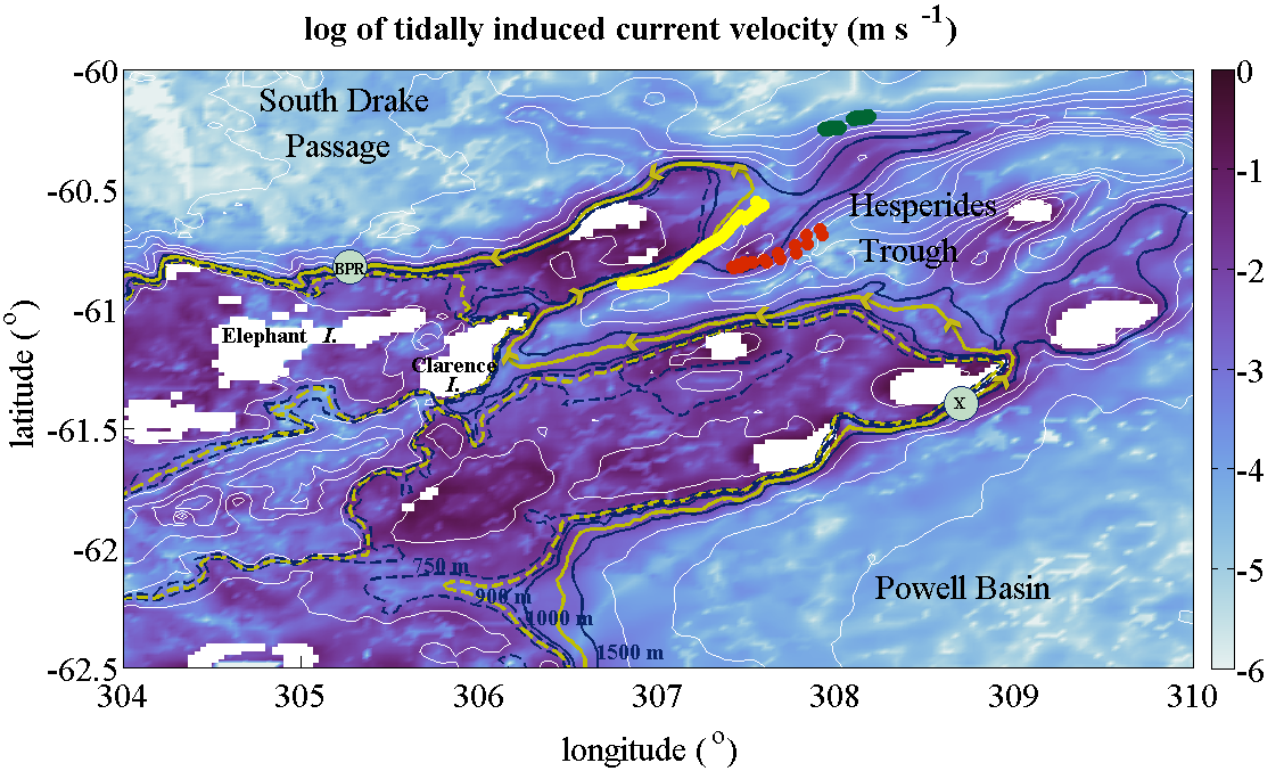

Figure 5.6: Zoomed-in area corresponding to the grey boxed area in Fig.5.1, coloured by the magnitude of the tidally-induced current, which flows anticlockwise around bumps and clockwise around troughs in the southern hemisphere. Excepting labelled islands, white regions are masked where the scale of the tidal excursion is greater than the bathymetric length scale ($L_T > L_B$ in 1.1), giving rise to unbounded values. The isobath between 700 m and 900 m is marked with thick dashed lines and the 825 m contour between is the yellow dashed line; the isobath between 1000 m and 1500 m contours is masked by the thick black line with the 1250 m contour line marked in yellow, with arrows denoting the direction of flow of the tidally induced current. Both isobaths connect Powell Basin and the continental slope in south Drake Passage. Point X and BPR are marked as the beginning and end of the route for which back-of-the-envelope timescales for the tidally-induced current are computed. EM-APEX sections A (red), B (yellow) and C (green) are shown, corresponding to regions where Weddell Sea waters are observed.

to the BPR site into line with that along deeper isobaths, so that, although less likely as it invokes multiple processes (and is not observed at the deeper lander), the export of Weddell waters along isobaths connecting Powell Basin and this location does not necessarily preclude downslope convection.

The pathways outlined here form a much more direct route from Powell Basin than previously suggested, allowing dense waters to exit Hesperides Trough without having to first circulate around it. Thus, Weddell Sea waters would have had less opportunity to mix and would therefore retain more cohesive characteristics onto the continental slope - as we see in the temperature-salinity characteristics captured by the EM-APEX float and the BPR temperature signal, both of which exhibit cold, fresh, dense water. This would allow for significant mixing as observed over the slope at Elephant Island (Mead Silvester *et al.* , 2014) once in contact with warmer, saline CDW over the continental slope, allowing for downslope convection and AABW formation. At site C, further east from Elephant Island, diffusivity is moderately enhanced at the boundary between warm, salty CDW and the dense water it overlies (Fig.5.4 c), suggesting that these processes may extend beyond Elephant Island, over the continental slope. This shortened pathway connecting the reservoirs of Powell Basin and south Drake Passage, where flows are significant (and timescales therefore short) and persistent may also act as a biogeochemical pathway, connecting the two basins; flows are especially fast along the short sections connecting Powell Basin and Hesperides Trough as well as Hesperides Trough and south Drake Passage (see Fig.5.6). The proposed pathways highlight sites for further study and the monitoring of topographically-steered Weddell Sea water export, both tidally- and wind-forced, onto the continental slope along the Western Antarctic Peninsula.

5.5 Conclusions

We demonstrate that the magnitude of seasonal cool, dense water pulses over the continental slope north of Elephant Island is linked to the magnitude of previous-season sea-ice concentration peaks. While these seasonal pulses of dense water were previously thought to be

descending local DSW feeding AABW (Meredith *et al.* , 2003), the pulses are not detected lower down the slope (Meijers *et al.* , 2016), suggesting transport along bathymetric contours. Our strong, seasonally-lagged correlation with the magnitude of sea-ice concentration in Powell Basin, a region associated with dense water production as sea-ice forms, favours the ingression of remotely-produced dense waters as an explanation for dense water pulses at Elephant Island. Further east, but nearby along the continental slope and in western Hesperides Trough, both deployments of EM-APEX floats capture cold, dense waters, consistent with exported Weddell Sea waters but not their known or proposed export pathways. These observations closely follow bathymetric contours, and we show that the tidally-induced flow along contours connecting Powell Basin and the site of dense water pulses at Elephant Island is consistent with the seasonal time-lag we observe, and is consistent with the topographically steered EM-APEX float observations and Thompson *et al.* (2009)'s drifter pathways. The timescale of our tidally-induced pathways may also be significant for biogeochemical connectivity between the two basins separated by the SSR, and this deserves further investigation. However, the time-lag is also consistent with Meijers *et al.* (2016)'s hypothesis that wind stress curl over the Weddell gyre intensifies boundary currents and allows waters to cross the SSR through topography and our EM-APEX float observations might represent a braided continuation of the ASC through the SSR. Both invoke isobathically steered flows on similar timescales. We therefore suggest that seasonal dense-water pulses are likely remotely produced and may be exported across the SSR from the Weddell Sea by the wind-forced ASC or tidally-induced current. This is shorter route than previously proposed, allowing more coherent dense water properties to come into contact with warmer CDW which can then transform to replenish and ventilate AABW. Mapping the pathways of dense water export and understanding their drivers and their variability is a critical step towards monitoring AABW variability on seasonal, interannual and longer timescales. This is particularly important given recent trends in the warming and freshening of Weddell Sea waters, exported waters and AABW and forecasting how these changes might influence overturning strength and the efficacy of CO_2 drawdown in the Southern Ocean.

5.6 Acknowledgments

We thank the officers and crew of the RRS *James Clark Ross* and the British Antarctic Survey IT and ETS personnel for their support during the science cruises JR195 and JR305. We are extremely grateful to Yvonne Firing, Geoff Hargreaves and Steve Mack for deploying EM-APEX float 4980b and to John Dunlap at for software support at Webb Research Corporations (USA). JMS was supported by NERC studentship (NE/K500938/1); YDL by NERC Fellowship (NE/H016007/1); JP by NERC grants ORCHESTRA NE/N018095/1 and PycnMix NE/L003325/1; HEP by the Australian Government's National Environmental Science Program and Australian Research Council Grants DP0877098 and CE110001028; TPR by TEA-COSI (NE/1029226/1) and OSMOSIS (NE/1019794/1)MAMM by OSCAR (NE/I022868/1).

5.7 Supporting Information

This section contains supporting information for Chapter 5. This includes plots that support the analysis and information provided such as those 'not shown' in the original manuscript and any background plots and statistics. The contents are as follows:

1. information on different areas used to average daily sea-ice concnetrations;
2. harmonic analysis of sea-ice concentration and BPR-temperature signals;
3. flagged datapoints removed during quality-control and
4. sections of parameters relevant to the shear-strain computation.

a)

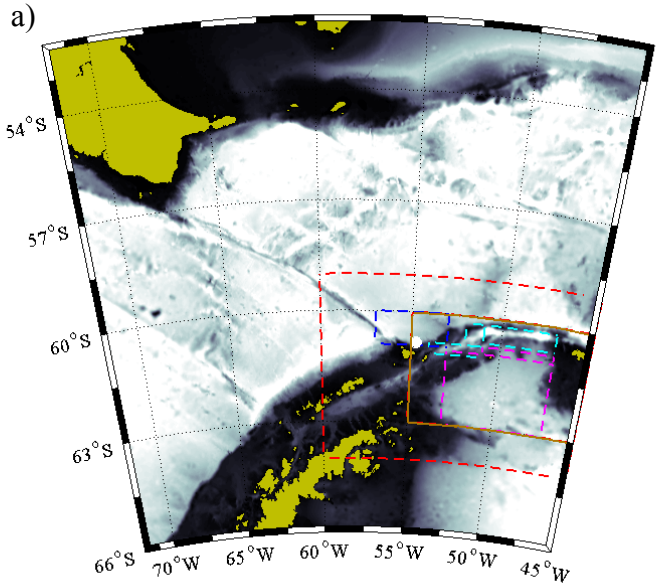

b)

Area	Lagged Correlation (*r*)	Significance (*p*)
Large general area	-0.6625	0.002
Small general area	**-0.6967**	**0.0009**
Powell Basin	-0.6628	0.002
Hesperides Trough	-0.6313	0.0016
Elephant Island shelf	-0.5877	0.0011

c)

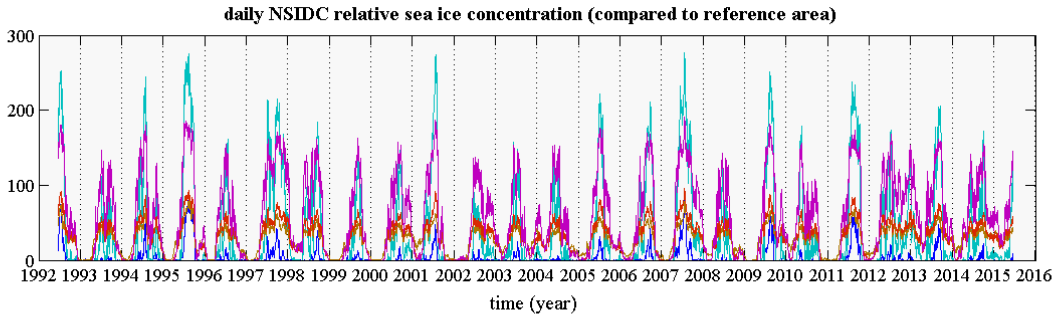

Figure 5.7: a) bathymetry is shaded as per Fig.5.1, the BPR location is the white dot and the areas over which daily sea-ice concentration is averaged are coloured to correspond the the areas in b) the tabulated, lagged, Pearson's correlations between the BPR-temperature troughs and sea-ice concentration peak magnitudes and c) the mean daily sea-ice concentration over each of the areas. There is no significant correlation with same-season sea-ice concentration and BPR-temperature troughs for any region.

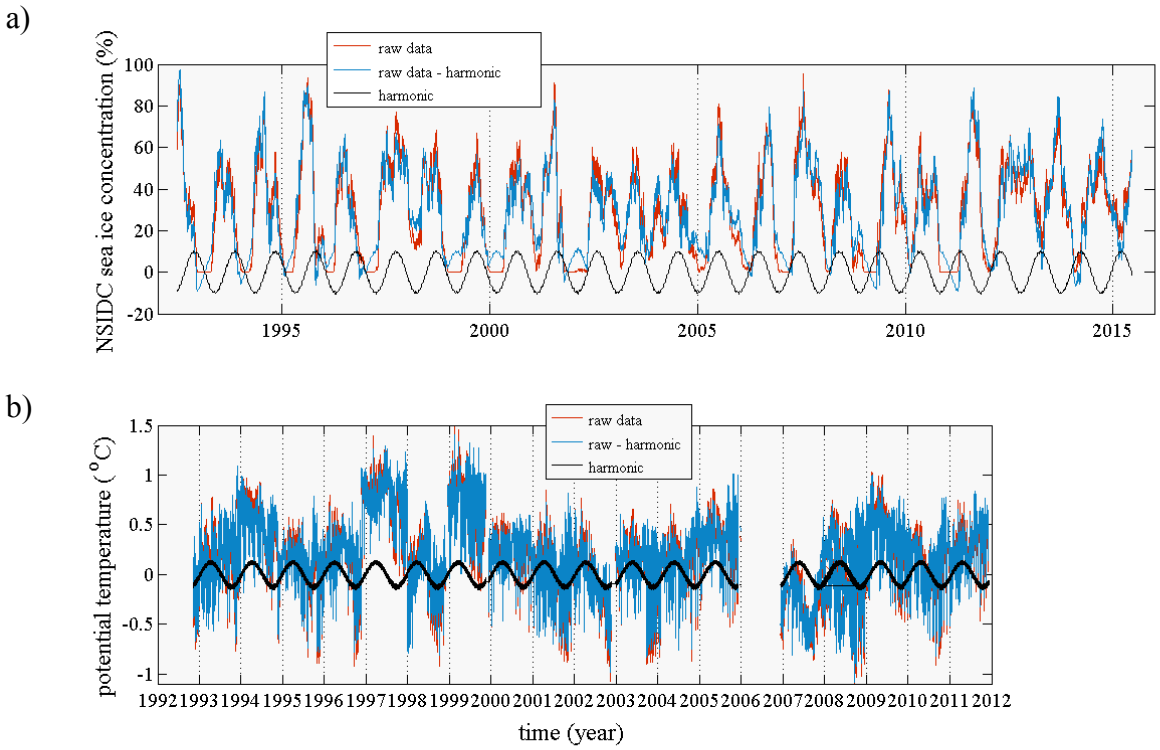

Figure 5.8: a) harmonic analysis for sea-ice concentration and b) BPR-temperature signals. Both display annual cycles, but it should be noted that harmonic analyses 'drift' towards the end of timeseries longer than 18.4 years as is the case for the sea-ice concentration signal here, so that the timing is not consistent for the latter portion of the timeseries.

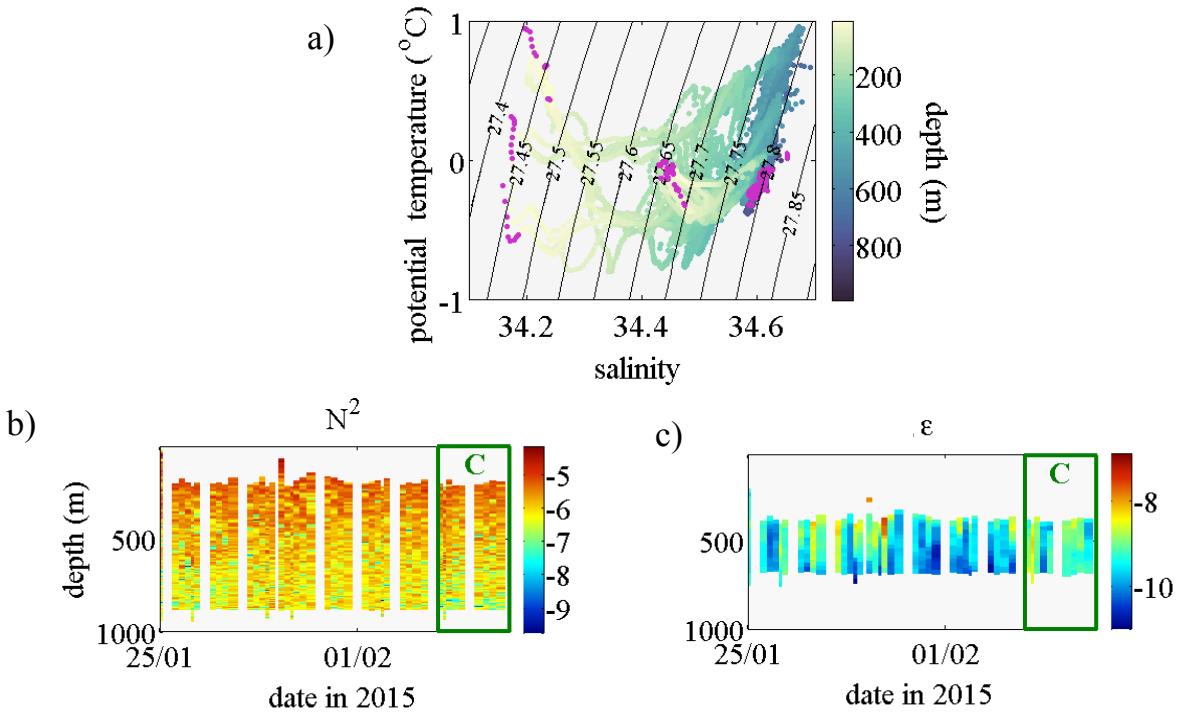

Figure 5.9: a) T-S diagram for all EM-APEX float datapoints used during this chapter with bad data flagged in magenta. These data are mainly from the tops and bottoms of ascending and descending profiles respectively as the float overshoots its target depth where bad pressure points are found as well as any outliers from individual T-S profiles. b) the buoyancy frequency and c) the dissipation (ϵ) that are used for computing the diffusivity in Fig. 5.4. Note the shortened profiles as datapoints are lost from the top and bottom of profiles during the shear-strain calculation.

Chapter 6

Synthesis

6.1 Summary

The aim of this thesis was to investigate processes that influence the watermass transformations acting to close the Southern Ocean MOC. The Southern Ocean, and in particular the area around the Antarctic Peninsula, has experienced rapid climate change over the past few decades, with a marked warming of the oceans (Gille, 2008). Observed variability in the atmosphere, ocean and cryosphere occurs on a multitude of timescales in this region, including seasonal, interannual and decadal, but there is growing evidence over the past few decades of trends linked to anthropogenic forcing (Meredith *et al.* , 2011). How these changes might feedback on climate is poorly understood, and the accuracy of climate models is constrained in no small part by poor parameterisations in the Southern Ocean: sub-grid scale processes such as tidal effects (Flexas *et al.* , 2015a), diapycnal mixing, and mesoscale to submesoscale eddies need to be parameterised, and these dictate the modelled exchange between watermasses and hence climate trends (Downes *et al.* , 2015). Our ability to accurately parameterise these processes is limited by understanding, partly due to a lack of observations in this harsh environment. A number of deficiencies in understanding were identified in Section 1.2.2, including quantifying intermittent diapycnal mixing and watermass transformations at depth where they can influence upwelling rates and identifying the sources and pathways of dense waters that feed AABW. As

such, the objectives of this thesis were to investigate:

1. intermittent diapycnal mixing at depth;
2. watermass transformations at depth;
3. sources of observed seasonal pulses of dense water at Elephant Island and
4. Weddell Sea water export pathways onto the continental slope.

The following paragraphs summarise how each of these objectives was met in turn and draws together the main findings in the context of current knowledge.

The short dissipation timeseries at Elephant Island (Chapter 3) addresses objectives (1) and (2) and explores enhanced diapycnal diffusivities of $O(10^{-3})$ associated with shear-driven turbulent mixing within upwelling CDW and across the interface of the two Southern Ocean overturning cells. These are the first direct measurements in support of Naveira Garabato *et al.* (2007)'s mid-depth mixing hypothesis and a driver for the missing mid-depth watermass transformations of Watson *et al.* (2013). These transformations effectively short-cut the adiabatic pathway in which transformations occur at the surface following adiabatic upwelling. Our enhanced mixing events are consistent with the breaking of locally-generated internal waves forced by the baroclinic tide. While this link remains a hypothesis, and a major weakness is therefore the inability to separate the inertial from the semidiurnal tide with such a short timeseries at this latitude, pinning this intermittent event to a mechanism is important because it enables a hypothetic up-scaling of the process that can inform future observational campaigns. For instance, we demonstrate that similar conditions (steep topography over which the same isopycnals outcrop and similar tidal amplitudes) extend to $\sim 60\%$ of the Antarctic continental slope so that the contribution to upwelling could be significant. It is therefore important for future observations over the shelf-break to resolve temporally-intermittent processes and we have highlighted regions where this can be studied.

In addition to the high diapycnal diffusivity and associated heat fluxes between UCDW and LCDW described in Chapter 3, EM-APEX float no.4980a captures direct heat exchange between

UCDW and LCDW at mid-depths over the shelf-break at Elephant Island two years later (Chapter 4) and address objective (2). This time, heat is exchanged across the bottom boundary of as an UCDW lens (likely an eddy) loses heat to the cooler LCDW below, an exchange driven by shear instability and turbulent mixing. Across the bottom boundary of the lens, we find that instabilities are consistent with symmetric forcing. We propose a mechanism in which the lens or eddy is stretched on a timescale consistent with the passing of baroclinic tides to enhance lateral density gradients, generating symmetric instabilities and creating the conditions for turbulent mixing. This hypothesised mechanism for heat dispersion is of particular relevance further west along the WAP where warm, UCDW-core eddies are the dominant mode of transporting heat onto the shelf (Martinson & McKee, 2012): here, the rising heat content of mid-depth LCDW is linked to the recent acceleration in basal melting of ice shelves (Cook *et al.* , 2016). The main limitations of the work in Chapter 4 are the poorly resolved lateral gradients which compromises the balanced Richardson number calculation (although this result is supported by potential vorticity analyses) and means we cannot determine whether the lens is an eddy, due to the sampling pattern of the EM-APEX float. It is also difficult to determine how Lagrangian the float is and therefore to what extent the lens is sampled in time and space. Nonetheless, this is a relatively high-resolution section in a poorly-sampled region and gives a rare insight into how warm water can penetrate at mid-depths over the continental slope of the WAP. Chapters 3 and 4 show that tides are likely to play a central role in mid-depth water mass transformations over the shelf-break through its interaction with steep topography and the submesoscale eddy field.

On the slope at Elephant Island, we have made separate observations of (1) enhanced diapycnal diffusivity and (2) direct heat exchange between water masses at mid-depths relevant to the lower (upper) boundary of the upper (lower) Southern Ocean overturning cells. Here too, seasonal pulses of dense, cold water are recorded over 20 years by a BPR lander at 1040 m, representing the lower boundary of the lower overturning cell on its descent path. Further east, but nearby along the continental slope and in western Hesperides Trough, both deployments of EM-APEX floats capture cold, dense waters, consistent with exported Weddell Sea waters but not their known or proposed export pathways. We investigate the origins of these waters

in Chapter 5, addressing objectives (3) and (4). We find a strong negative correlation between the magnitudes of seasonal dense water pulses and previous-season sea-ice concentration over a large area including Powell Basin in the Weddell Sea. While initially surprising, these time-lags are consistent with (1) Meijers *et al.* (2016) hypothesis that wind stress curl over the Weddell gyre intensifies boundary currents and allows waters to cross the SSR through topography and (2) tidally-induced flows along isobaths connecting the BPR on the slope at Elephant Island and Powell Basin. The latter is consistent with the topographically steered EM-APEX float observations as well as drifter pathways (Thompson *et al.* , 2009). We therefore suggest that seasonal dense-water pulses are remotely produced and exported across the SSR from the Weddell Sea via a considerably shorter route than previously proposed, allowing more coherent dense water properties to come into contact with warmer CDW which can then transform to replenish and ventilate AABW. This process is critical to CO_2 drawdown as well as overturning strength in the Southern Ocean. While Meredith *et al.* (2003) previously hypothesised that seasonal dense-water pulses are due to downslope convection feeding AABW as locally-produced DSW spreads and descends the steep slope (Meredith *et al.* , 2003), both Meijers *et al.* (2016) and our hypotheses invoke topographically-steered exports on similar timescales; however, the precise origins, driving mechanisms and supply pathways of observed dense-water pulses on the slope at Elephant Island remain elusive, and our dataset cannot explore these ideas further. Our inferences suggest that the isobaths connecting the BPR and Powell Basin are favourable sites for further studies aiming to capture Weddell Sea exports and monitor their variability. Mapping dense water export pathways and understanding their drivers is critical step towards monitoring AABW variability, especially given the recently observed freshening and warming of Weddell Sea watermasses, their exports and AABW itself. The contribution of the tidally-induced flow along this pathways and potentially others, deserves further investigation and is especially important given that general circulation models do not currently resolve - or often parameterise - these flows (Polton, 2015).

An emergent theme of this research is the contribution of tides to processes that influence the Southern Ocean MOC. Until recently, their contribution has been largely neglected by research campaigns in the SSC despite it being known as topographically favourable for the generation of

internal M_2 tides (Padman *et al.* , 2006). Only very recently have studies pointed towards their importance, including elucidating the role of the barotropic tide in setting up the ASF in western Powell Basin (Flexas *et al.* , 2015a) and mixing induced by interactions between the barotropic tide and the downwelling Ekman layer at Orkney Passage where WSDW is exported (Polzin *et al.* , 2014). The findings of this thesis implicate the tide in forcing mid-water diapycnal mixing as it interacts with topography and driving overturns as it modifies submesoscale features such as eddies. These processes, in driving transformation at depth, not only influence upwelling rates and the Southern Ocean MOC but also facilitate ocean warming at mid-depths where WAP glacier melt is sensitive to heat content. Additionally, we have proposed a mechanism whereby eddy-tide interactions could disperse heat over the continental slope and deliver heat onto the shelf to contribute to basal ice shelf melt along the WAP. This work also demonstrates that the tidally-induced flow could influence the export pathways of Weddell Sea water. The importance of tidal processes here, even if temporally intermittent and limited to shelf-breaks and connecting isobaths, should not be overlooked since it is periodic and predictable, unlike the wind stress force at these latitudes. This is particularly useful in pinpointing where locally-concentrated mixing can be observed and sites for monitoring Weddell Sea water exports (i.e along particular isobaths). However, the main deficiency of the work of Chapters 3 and 4 is the inability to truly separate the inertial and tidal frequencies that contribute to watermass transformation due to short time-series. At this latitude, the frequencies of the dominant M_2 tide and inertial oscillations are close to semi-diurnal, necessitating longer time-series for reliable spectral peak separation. While our observations are consistent with tidal forcing, it remains for future observations to explore this further through longer timeseries that can resolve (and repeat) intermittent tidal mixing and are of a sufficient resolution to partition inertial and tidal forcing.

The body of this thesis explored dynamical processes that take place on the scale of centimeters (i.e diapycnal mixing; heat exchange; tidal flows) which nevertheless, through their spatial prevalence, define the sensitive regional climate. This is demonstrated here through mid-water transformations in areas that can effect WAP ice melt and Southern Ocean upwelling rates as well as the modification of watermasses critical to overturning strength and the Southern

Ocean CO_2 flux. Climatological changes in the Southern Ocean, such as those exemplified near the tip of the Antarctic Peninsula, may be relatively quickly transmitted to the major ocean basins to be felt on a global scale. The Antarctic Peninsula and its surrounding waters have warmed over the past decades and while the timescales of transmission elsewhere and feedbacks are as yet largely unknown, this is an important region to monitor. Global circulation models and climate models are at present our most powerful climate forecasting tool; however they are limited in resolution, and our findings point to a number of processes from the temporally intermittent elevated tidal mixing to submesoscale heat dispersion and tidally-induced flows that these models must parameterise. The accuracy of these parameterisations currently limits the performance of climate models. The work of this thesis has made a small contribution towards identifying, quantifying and spatially characterising sub-grid processes in the Southern Ocean, and suggests locations in which these might have a disproportionate influence on the regional climate.

6.2 Conclusions

This thesis investigates three processes that influence water mass transformations in the Southern Ocean. Two mechanisms are proposed based on observations of mid-depth mixing that allow transformation at depth, impacting the total buoyancy budget of the circulation and so the rate of upwelling in the Southern Ocean. Upwelling here plays a central role in setting the strength of the global overturning circulation and, regionally, delivering warm waters into contact with the base of ice shelves as well as the rate of ventilation of deep, carbon-rich waters and its uptake from the atmosphere. The production rate and properties of AABW formation can in its own right also influence Southern Ocean overturning strength and the communication of sequestered CO_2 with the atmosphere. We have demonstrated the likely existence of a new, shorter pathway for coherent dense Weddell Sea waters to be exported onto the continental slope where it can mix with CDW to form AABW. The mechanisms for mid-water transformations, heat dispersion and export routes proposed here are relevant to understanding the causal pathways and the impact of recent warming and freshening of watermasses that are critical to

overturning in this region. Additionally, this work demonstrates that tides play a key role in driving watermass transformations near the tip of the Antarctic Peninsula and that sub-grid scale processes can, depending on location, have a disproportionate impact on regional climate.

6.3 Future Work

There is a vast body of work currently underway trying to improve the performance of climate models through better Southern Ocean parameterisations. This thesis hypothesises a number of mechanisms that are driven by sub-grid scale processes to explain observed transformations that, because of their locations, might have a disproportionate impact on the regional climate. Similar preconditions to these mechanisms extend to the wider region along the continental slope, so that their total effect could be significant. It is suggested then, that future studies should concentrate on regions in which sub-grid scale processes could have large effects due to scale or simple feedbacks, e.g eddy-tide interactions along the WAP and glacier melt; locally-generated internal tidal waves breaking along the Antarctic shelf-break; teleconnections between basins that might plausibly be linked through bathymetry; tidally-induced currents through topographical barriers. This could be achieved with observational campaigns along the WAP targeting areas where UCDW-core eddies are active e.g using gliders and moorings to capture heat exchange at the base of eddies, ensuring long enough timeseries for peak separation between semi-diurnal tides and inertial forcing. Ocean models such as Nucleus for European Modelling of the Ocean (NEMO) could be used to explore the evolution of UCDW lenses and regions favourable for the breaking of locally-generated internal tidal waves over the continental slope. The latter, complemented by observations (e.g from ARGO floats), could be used to compute the potential contribution of shelf-break mixing processes to coastal upwelling over the Antarctic shelf-break. Models such as NEMO and MITgcm could be used to explore export pathways from e.g the Weddell Sea by particle-tracking along isobaths that connect basins to complement carefully placed moorings along connecting isobaths.

Since the sub-grid processes outlined here are likely tidally-forced and the tide is predictable, it

may be possible to improve parameterisations under certain conditions (e.g eddy-tide interaction at specific locations). These could be explored through coupled ice-ocean, tide and general circulation models as well as observations: a number of locations have been identified in this thesis where future observations could test the hypotheses set out here.

Bibliography

Abernathey, R., Marshall, J., & Ferreira, D. 2011. The dependence of Southern Ocean meridional overturning on wind stress. *Journal of Physical Oceanography*, **41**(12), 2261–2278.

Alford, M.H. 2003. Redistribution of energy available for ocean mixing by long-range propagation of internal waves. *Nature*, **423**(6936), 159.

Amante, C., & Eakins, B.W. 2009. *ETOPO1 1 arc-minute global relief model: procedures, data sources and analysis*. US Department of Commerce, National Oceanic and Atmospheric Administration, National Environmental Satellite, Data, and Information Service, National Geophysical Data Center, Marine Geology and Geophysics Division.

Anderson, R.F., Ali, S., Bradtmiller, L.I., Nielsen, S.H.H., Fleisher, M.Q., Anderson, B.E., & Burckle, L.H. 2009. Wind-driven upwelling in the Southern Ocean and the deglacial rise in atmospheric CO2. *science*, **323**(5920), 1443–1448.

Baines, P.G. 1982. On internal tide generation models. *Deep Sea Research Part A. Oceanographic Research Papers*, **29**(3), 307 – 338.

Brannigan, L., Y-D., Lenn, Rippeth, T.P., McDonagh, E., Chereskin, T.K., & Sprintall, J. 2013. Shear at the Base of the Oceanic Mixed Layer Generated by Wind Shear Alignment. *Journal of Physical Oceanography*, July, 1798–1810.

Cook, A. J., Holland, P. R., Meredith, M. P., Murray, T., Luckman, A., & Vaughan, D. G. 2016. Ocean forcing of glacier retreat in the western Antarctic Peninsula. **353**(6296), 283–286.

Cullen, J.J., & Boyd, P.W. 2008. Predicting and verifying the intended and unintended consequences of large-scale ocean iron fertilization. *Marine Ecology Progress Series*, **364**, 295–302.

Downes, S.M., Farneti, R.and Uotila, P., Griffies, S.M., Marsland, S.J., Bailey, D., Behrens, E.and Bentsen, M., Bi, D., Biastoch, A., *et al.* . 2015. An assessment of Southern Ocean water masses and sea ice during 1988–2007 in a suite of interannual CORE-II simulations. *Ocean Modelling*, **94**, 67–94.

Ducklow, H.W., Steinberg, D.K., & Buesseler, K.O. 2001. Upper ocean carbon export and the biological pump. *Oceanography-Washington DC - Oceanography Society*, **14**(4), 50–58.

Egbert, G.D., & Erofeeva, S.Y. 2002. Efficient Inverse Modeling of Barotropic Ocean Tides. *Journal of Atmospheric and Oceanic Technology*, **19**(2), 183–204.

Egbert, G.D., Bennett, A.F, & Foreman, M.G.G. 1994. TOPEX/POSEIDON tides estimated using a global inverse model. *Journal of Geophysical Research: Oceans*, 24821–24852.

Egbert, G.D., Ray, R. D., & Bills, B.G. 2004. Numerical modeling of the global semidiurnal tide in the present day and in the last glacial maximum. *Journal of Geophysical Research: Oceans*, **109**(C3), n/a–n/a. C03003.

Farneti, R., Downes, S.M., Griffies, S.M., Marsland, S.J., Behrens, E., Bentsen, M., Bi, D., Biastoch, A., Böning, C., Bozec, A., *et al.* . 2015. An assessment of Antarctic Circumpolar Current and Southern Ocean meridional overturning circulation during 1958–2007 in a suite of interannual CORE-II simulations. *Ocean Modelling*, **93**, 84–120.

Flexas, M. d M., Schodlok, M.P., Padman, L., Menemenlis, D., & Orsi, A.H. 2015a. Role of tides on the formation of the Antarctic Slope Front at the Weddell-Scotia Confluence. *Journal of Geophysical Research: Oceans*, **120**(5), 3658–3680.

Flexas, M. M., Schodlok, M. P., Padman, L., Menemenlis, D., & Orsi, A. H. 2015b. Role of tides on the formation of the Antarctic Slope Front at the Weddell-Scotia Confluence. *Journal of Geophysical Research: Oceans*, **120**(5).

Fyfe, J.C., Saenko, O.A., Zickfeld, K., Eby, M., & Weaver, A.J. 2007. The role of poleward-intensifying winds on Southern Ocean warming. *Journal of Climate*, **20**(21), 5391–5400.

Gille, S.T. 2008. Decadal-scale temperature trends in the Southern Hemisphere ocean. *Journal of Climate*, **21**(18), 4749–4765.

Hallberg, R., & Gnanadesikan, A. 2006. The Role of Eddies in Determining the Structure and Response of the Wind-Driven Southern Hemisphere Overturning: Results from the Modeling

Eddies in the Southern Ocean (MESO) Project. *Journal of Physical Oceanography*, Dec., 2232–2252.

Heywood, K.J., Naveira Garabato, A.C., Stevens, D.P., & Muench, R.D. 2004. On the fate of the Antarctic Slope Front and the origin of the Weddell Front. *Journal of Geophysical Research: Oceans*, **109**(C6).

Heywood, K.J., Collins, J.L., Hughes, C.W., & Vassie, I. 2007. On the detectability of internal tides in Drake Passage. *Deep Sea Research Part I: Oceanographic Research Papers*, **54**(11), 1972 – 1984.

Huang, N.E. 2014. *Hilbert-Huang transform and its applications*. Vol. 16. World Scientific.

Huang, R.X. 1999. Mixing and Energetics of the Oceanic Thermohaline Circulation*. *Journal of Physical Oceanography*, Apr., 727–746.

Huthnance, J.M. 1973. Tidal current asymmetries over the Norfolk Sandbanks. *Estuarine and Coastal Marine Science*, **1**(1), 89 – 99.

Huybers, P., & Wunsch, C., year=2009 publisher=Annual Reviews. Paleophysical oceanography with an emphasis on transport rates.

Ito, T., Woloszyn, M., & Mazloff, M. 2010. Anthropogenic carbon dioxide transport in the Southern Ocean driven by Ekman flow. *Nature*, **463**(7277), 80.

Jacobs, S.S., & Giulivi, C.F. 2010. Large multidecadal salinity trends near the Pacific–Antarctic continental margin. *Journal of Climate*, **23**(17), 4508–4524.

Johnson, G.C. 2008. Quantifying Antarctic Bottom Water and North Atlantic Deep Water volumes. *Journal of Geophysical Research: Oceans*, **113**(C5).

Jullion, L., Naveira Garabato, A.C., Meredith, M.P., Holland, P.R., Courtois, P., & King, B.A. 2013. Decadal Freshening of the Antarctic Bottom Water Exported from the Weddell Sea. *Journal of Climate*, **26**(20), 8111–8125.

Kara, A. B.and Rochford, P.A., & Hurlburt, H.E. 2000. An optimal definition for ocean mixed layer depth. *Journal of Geophysical Research: Oceans*, **105**(C7), 16803–16821.

Kunze, E., Firing, E., Hummon, J.M., Chereskin, T.K., & Thurnherr, A.M. 2006. Global Abyssal Mixing Inferred from Lowered ADCP Shear and CTD Strain Profiles. *Journal of Physical Oceanography*, **36**(8), 1553–1576.

Large, W. G., & Pond, S. 1981. Open Ocean Momentum Flux Measurements in Moderate to Strong Winds. *Journal of Physical Oceanography*, **11**(3), 324–336.

Le Quéré, C., Orr, J.C., Monfray, P., Aumont, O., & Madec, G. 2000. Interannual variability of the oceanic sink of CO2 from 1979 through 1997. *Global Biogeochemical Cycles*, **14**(4), 1247–1265.

Le Quéré, C., Rödenbeck, C., Buitenhuis, E.T., Conway, T.J., Langenfelds, R., Gomez, A., Labuschagne, C., Ramonet, M.and Nakazawa, T., Metzl, N., *et al.* . 2008. Response to Comments on Saturation of the Southern ocean CO2 sink due to recent climate change. *science*, **319**(5863), 570c–570c.

Lumpkin, R., & Speer, K. 2007. Global Ocean Meridional Overturning. *Journal of Physical Oceanography*, Oct., 2550–2562.

Marshall, J., & Radko, T. 2003. Residual-mean solutions for the Antarctic Circumpolar Current and its associated overturning circulation. *Journal of Physical Oceanography*, **33**(11), 2341–2354.

Marshall, J., & Speer, K. 2012. Closure of the meridional overturning circulation through Southern Ocean upwelling. *Nature Geoscience*, Feb., 171–180.

Martinson, D. G., & McKee, D. C. 2012. Transport of warm Upper Circumpolar Deep Water onto the western Antarctic Peninsula continental shelf. *Ocean Science*, **8**(4), 433–442.

Mead Silvester, J., Lenn, Y-D., Polton, J.A .and Rippeth, T.P., & Morales Maqueda, M. 2014. Observations of a diapycnal shortcut to adiabatic upwelling of Antarctic Circumpolar Deep Water. *Geophysical Research Letters*, Oct., 2014GL061538.

Meehl, G.A., T.F. Stocker W.D. Collins P. Friedlingstein A.T. Gaye J.M. Gregory A. Kitoh R. Knutti J.M. Murphy A. Noda S.C.B. Raper I.G. Watterson A.J. Weaver, & Zhao, Z.-C. 2007. *IPCC*. Cambridge, United Kingdom and New York, NY, USA: Cambridge University Press. Chap. Index, pages 747–845.

Meijers, A. J. S., Meredith, M. P., Abrahamsen, E. P., Morales Maqueda, M. A., Jones, D. C., & Naveira Garabato, A. C. 2016. Wind-driven export of Weddell Sea slope water. *Journal of Geophysical Research: Oceans*, **121**(10).

Meredith, M.P., & King, J.C. 2005. Rapid climate change in the ocean west of the Antarctic Peninsula during the second half of the 20th century. *Geophysical Research Letters*, **32**(19).

Meredith, M.P., Hughes, C.W., & Foden, P.R. 2003. Downslope convection north of Elephant Island, Antarctica: Influence on deep waters and dependence on ENSO. *Geophysical Research Letters*, May, 1462.

Meredith, M.P., Woodworth, P.L., Chereskin, T.K., Marshall, D.P., Allison, L.C., Bigg, G.R., Donohue, K., Heywood, K.J., Hughes, C.W., Hibbert, A., *et al.* . 2011. Sustained monitoring of the Southern Ocean at Drake Passage: Past achievements and future priorities. *Reviews of Geophysics*, **49**(4).

Meredith, M.P., Brown, P.J., Naveira Garabato, A.C., Jullion, L.and Venables, H.J., & Messias, M-J. 2013. Dense bottom layers in the Scotia Sea, Southern Ocean: Creation, lifespan, and destruction. *Geophysical Research Letters*, **40**(5).

Meyer, A., Phillips, H.E, & Polzin, K.L. 2014. *Mixing (MX) Oceanographic Toolbox for EM-APEX* float data applying shear-strain finescale parameterisation.* Technical Report.

Meyer, M, Sloyan, B.M., Polzin, K.L., Phillips, H.E., & Bindoff, N.L. 2015. Mixing Variability in the Southern Ocean. *Journal of Physical Oceanography*, **45**(4), 966–987.

Moffat, C., Owens, B., & Beardsley, R. C. 2009. On the characteristics of Circumpolar Deep Water intrusions to the west Antarctic Peninsula Continental Shelf. *Journal of Geophysical Research: Oceans*, **114**(C5).

Munk, W., & Wunsch, C. 1998. Abyssal recipes II: energetics of tidal and wind mixing. *Deep Sea Research Part I: Oceanographic Research Papers*, **45**(12), 1977 – 2010.

Munk, W.H. 1966. Abyssal recipes. *Deep Sea Research and Oceanographic Abstracts*, Aug., 707–730.

Naveira Garabato, A.C., , E.L. McDonagh, Stevens, D.P., Heywood, K.J., & Sanders, R.J. 2002. On the export of Antarctic Bottom Water from the Weddell Sea. *Deep Sea Research Part II: Topical Studies in Oceanography*, **49**(21), 4715 – 4742.

Naveira Garabato, A.C., Polzin, K.L., King, B.A., Heywood, K.J., & Visbeck, M. 2004. Widespread Intense Turbulent Mixing in the Southern Ocean. *Science*, Jan., 210–213.

Naveira Garabato, A.C., Stevens, D.P, Watson, A.J., & Roether, W. 2007. Short-circuiting of the overturning circulation in the Antarctic Circumpolar Current. *Nature*, May, 194–197.

Nikurashin, M., Vallis, G.K., & Adcroft, A. 2013. Routes to energy dissipation for geostrophic flows in the Southern Ocean. *Nature Geoscience*, **6**(1), 48.

Ohshima, K. I., Nihashi, Sohey, & Iwamoto, Katsushi. 2016. Global view of sea-ice production in polynyas and its linkage to dense/bottom water formation. *Geoscience Letters*, **3**(1), 13.

Osborn, T. R. 1980. Dissipation Measurements of Oceanic Turbulence. *Pages 143–155 of:* J, Jacques C, & T, Nihoul B (eds), *Marine Turbulence Proceedings of The 11th International Liège Colloquium on Ocean Hydrodynamics*. Elsevier.

Padman, L., H. S., & Erofeeva, L. 2014. *AntPen04.01: Antarctic Peninsula High-Resolution Tidal Forward Model*. TMD Manual.

Padman, L., Fricker, H. A., Coleman, R., Howard, S., & Erofeeva, L. 2002. *A new tide model for the Antarctic ice shelves and seas*. Annals of Glaciology, vol. 34. Cambridge: Int Glaciological Soc. n/a. Pages 247–254.

Padman, L., Howard, S., & Muench, R. 2006. Internal tide generation along the South Scotia Ridge. *Deep Sea Research Part II: Oceanographic Research Papers*, **53**, 157–171.

Palmer, M., Gomis, D., Flexas, M.M., Jord, G., Jullion, L., Tsubouch, T.i, & Naveira Garabato, A.C. 2012. Water mass pathways and transports over the South Scotia Ridge west of 50W. *Deep Sea Research Part I: Oceanographic Research Papers*, **59**, 8 – 24.

Peixoto, J.P., & Oort, A.H. 1992. *The Physics of Climate*. Springer-Verlag GmbH.

Piola, A.R., & Gordon, A.L. 1989. Intermediate waters in the southwest South Atlantic. *Deep Sea Research Part A. Oceanographic Research Papers*, Jan., 1–16.

Polton, J. A., & Marshall, D. P. 2007. Overturning cells in the Southern Ocean and subtropical gyres. *Ocean Science*, **3**(1), 17–30.

Polton, J.A. 2015. Tidally induced mean flow over bathymetric features: a contemporary challenge for high-resolution wide-area models. *Geophysical & Astrophysical Fluid Dynamics*, **109**(3), 207–215.

Polzin, K.L, Naveria Garabato, A.C., Abrahamsen, E. Povl, Jullion, L., & Meredith, Michael P. 2014. Boundary mixing in Orkney Passage outflow. *Journal of Geophysical Research: Oceans*, **119**(12), 8627–8645.

Purkey, S.G., & Johnson, G.C. 2010. Warming of Global Abyssal and Deep Southern Ocean Waters between the 1990s and 2000s: Contributions to Global Heat and Sea Level Rise Budgets. *Journal of Climate*, **23**(23), 6336–6351.

Purkey, S.G., & Johnson, G.C. 2012. Global contraction of Antarctic Bottom Water between the 1980s and 2000s. *Journal of Climate*, **25**(17), 5830–5844.

Robertson, R. 2001. Internal tides and baroclinicity in the southern Weddell Sea 1 . Model description. 1–22.

Robinson, I.S. 1981. Tidal vorticity and residual circulation. *Deep Sea Research Part A. Oceanographic Research Papers*, **28**(3), 195 – 212.

Sabine, C.L., Feely, R.A., Gruber, N., Key, R.M., Lee, K., Bullister, J.L., Wanninkhof, R., Wong, C.S.l, Wallace, Douglas W.R., Tilbrook, B., *et al.* . 2004. The oceanic sink for anthropogenic CO2. *science*, **305**(5682), 367–371.

Saenko, O.A., Fyfe, J.C., & England, M.H. 2005. On the response of the oceanic wind-driven circulation to atmospheric CO2 increase. *Climate dynamics*, **25**(4), 415–426.

Schmidtko, S., Heywood, K.J., Thompson, A.F., & Aoki, S. 2014. Multidecadal warming of Antarctic waters. **346**(6214), 1227–1231.

Schodlok, M.P., Hellmer, H.H., & Beckmann, A. 2002. On the transport, variability and origin of dense water masses crossing the South Scotia Ridge. *Deep Sea Research Part II: Topical Studies in Oceanography*, **49**(21), 4807 – 4825.

Sigman, D.M., & Boyle, E.A. 2000. Glacial/interglacial variations in atmospheric carbon dioxide. *Nature*, **407**(6806), 859.

Simmons, H.L., Hallberg, R.W., & Arbic, B.K. 2004. Internal wave generation in a global baroclinic tide model. *Deep Sea Research Part II: Topical Studies in Oceanography*, **51**(25-26), 3043–3068.

Sloyan, B.M., & Rintoul, S.R. 2001. The Southern Ocean Limb of the Global Deep Overturning Circulation. *Journal of Physical Oceanography*, Jan., 143–173.

Snow, K., Hogg, A.M., Sloyan, B.M., & Downes, S.M. 2016. Sensitivity of Antarctic bottom water to changes in surface buoyancy fluxes. *Journal of Climate*, **29**(1), 313–330.

Tamsitt, V., Drake, H.F., Morrison, A. K., Talley, L.D., Dufour, C.O., Gray, A.R., Griffies, S.M., Mazloff, M.R., Sarmiento, J.L., Wang, J., & Weijer, W. 2017. Spiraling pathways of global deep waters to the surface of the Southern Ocean. *Nature Communications*, 172.

Thomas, L.N., Taylor, J.R., Ferrari, R., & Joyce, T.M. 2013. Symmetric instability in the Gulf Stream. *Deep Sea Research Part II: Topical Studies in Oceanography*, **91**, 96 – 110.

Thompson, A.F., Heywood, K.J., Thorpe, S.E., Renner, A.H.H., & Trasvia, T. 2009. Surface Circulation at the Tip of the Antarctic Peninsula from Drifters. *Journal of Physical Oceanography*, **39**(1), 3–26.

Thompson, A.F., Heywood, K.J., Schmidtko, S., & Stewart, A.L. 2014. Eddy transport as a key component of the Antarctic overturning circulation. *Nature Geoscience*, Dec., 879–884.

van Wijk, E.M., & Rintoul, S.R. 2014. Freshening drives contraction of Antarctic Bottom Water in the Australian Antarctic Basin. *Geophysical Research Letters*, **41**(5).

von Gyldenfeldt, A.-B., Fahrbach, Eberhard, Garcia, M. A., & Schröder, Michael. 2002. Flow Variability at the Tip of the Antarctic Peninsula. *Deep-sea research ii*, **49**, 4791–4806.

Watson, A.J., Ledwell, J.R., Messias, M-J., King, B.A, Mackay, N., Meredith, M.P, Mills, B., & Naveira Garabato, A.C. 2013. Rapid cross-density ocean mixing at mid-depths in the Drake Passage measured by tracer release. *Nature*, Sept., 408–411.

Whalen, C.B., Talley, L.D., & MacKinnon, J.A. 2012. Spatial and temporal variability of global ocean mixing inferred from Argo profiles. *Geophysical Research Letters*, **39**(18).

White, W.B., & Peterson, R.G. 1996. An Antarctic circumpolar wave in surface pressure, wind, temperature and sea-ice extent. *Nature*, **380**(6576), 699.

Wu, L., Jing, Z., Riser, S., & Visbeck, M. 2011. Seasonal and spatial variations of Southern Ocean diapycnal mixing from Argo profiling floats. *Nature Geosci*, June, 363–366.

Wunsch, C.and Ferrari, R. 2004. Vertical Mixing, Energy, And The General Circulation Of The Oceans. *Annual Review of Fluid Mechanics*, Jan., 281–314.

Youngs, M.K., Thompson, A.F., Flexas, M.M., & Heywood, K.J. 2015. Weddell Sea Export Pathways from Surface Drifters. *Journal of Physical Oceanography*, **45**(4), 1068–1085.

Zhai, X., Johnson, H.L, Marshall, D.P, & Wunsch, C. 2012. On the Wind Power Input to the Ocean General Circulation. *Journal of Physical Oceanography*, May, 1357–1365.